UNIVERSITY OF CALIFORNIA,
IRVINE

Reduced-Order Modeling of Unsteady Aerodynamics: Theoretical and Computational Approaches

DISSERTATION

submitted in partial satisfaction of the requirements
for the degree of

DOCTOR OF PHILOSOPHY

in Mechanical and Aerospace Engineering

by

Amir Saman Rezaei

Dissertation Committee:
Professor Haithem E. Taha, Chair
Professor William Sirignano
Professor Said Elghobashi

2019

DEDICATION

To my family and friends, whose love and unwavering support made this pursuit possible.

TABLE OF CONTENTS

LIST OF FIGURES

LIST OF TABLES

Page

Nomenclature

α	geometric angle of attack
α_u	angle of attack during upstroke motion
α_d	angle of attack during downstroke motion
α_{eff}	effective angle of attack ($\frac{\dot{\alpha}b}{U_\infty}$)
b	half chord ($\frac{c}{2}$)
U_∞	freestream velocity
U	local velocity
w	angular velocity of the prescribed motion
k	reduced frequency ($\frac{\omega b}{U_\infty}$)
A	amplitude of pitching
$\dot{\Gamma}$	rate of changing of the circulation
y_{upper}	y-coordinate of the boundary layer on the top surface
y_{lower}	y-coordinate of the boundary layer on the bottom surface
Δy	difference in the thickness of the top and bottom boundary layer
μ	dynamic viscosity
μ_t	eddy viscosity
ρ	density
Re	chord based Reynolds number
Re_θ	momentum-thickness Reynolds number
$\hat{Re}_{\theta t}$	local transition onset momentum-thickness Reynolds number
θ	momentum thickness
γ	intermittency
TI	turbulent intensity
TE	trailing-edge

ACKNOWLEDGMENTS

I would like to thank my Ph.D. advisor, Professor Haithem Taha, for his advice, patience and for supporting me in the past four years. He is one of the smartest, most humble and most courteous people I know. He was not only my PI, but my older brother. I could not wish for a better Ph.D. experience.

I also thank my family and friends for their endless support and providing unconditional love and care. Definitely, I could not be in my current stage without their help and encouragement.

I also thank my qualifying exam committee members, which also includes my PhD defense committee members, Professor William Sirignano, Said Elghobashi, Feng Liu and Tom Trogdon for their help and consideration. I should thank Professor Sirignano, Elghobashi, Liu and Papamoschou who taught me the fundamentals in math and fluid mechanics.

I would like to thank professor Khalid Rafique, Dr. James Lewis and Dr. Tim Kost er for helping me during my teaching assistantship for the wind tunnel course at UCI and for all the fruitful discussions we had. I appreciate the help of Carlos Renan Dos Santos during the last year of my PhD study.

I thank all of the previous and current fellow lab mates for their suggestions and help.

Lastly, I would like to acknowledge the support of the National Science Foundation grant CMMI-1635673.

CURRICULUM VITAE

Amir Saman Rezaei

EDUCATION

Ph.D. in Mechanical and Aerospace Engineering (Jan 2016-Dec 2019)
University of California Irvine, Irvine, CA. (3.9/4.0 GPA)

* Funding Organization: National Science Foundation **(NSF)**, Grant#: 1635673

- Recipient of " 2018 AIAA OC section **best student award**" for continued academic excellence and developing **CFD** models for transient flows.

Master of Science in Mechanical Engineering (2012-2015)
University of Tehran, Tehran, Iran. (4.0/4.0 GPA)

RESEARCH EXPERIENCE

Graduate Research Assistant **2016–2019**
University of California, Irvine *Irvine, California*

TEACHING EXPERIENCE

University of California, Irvine *Irvine, California*
Teaching Assistant for MAE 108 (Wind Tunnel) **2017–2019**
Teaching Assistant for MAE 60 (Electrical Circuits) **2017**
University of Tehran, Iran *Tehran, Iran*
Teaching Assistant for Fluid Dynamics **2015**
Teaching Assistant for CFD **2015**
Teaching Assistant for Advanced Mathematics **2014**

WORK EXPERIENCE

Internship: CFD Engineer at Alcon, Surgical Instrumentation, R&D unit, Lake forest, CA (Summer 2019)

PROFESSIONAL ACTIVITIES

Reviewer
-Journal of Fluid Mechanics

-Journal of Fluids and Structures
-The Aeronautical Journal
-Drones

ABSTRACT OF THE DISSERTATION

Reduced-Order Modeling of Unsteady Aerodynamics: Theoretical and Computational Approaches

By

Amir Saman Rezaei

Doctor of Philosophy in Mechanical and Aerospace Engineering

University of California, Irvine, 2019

Professor Haithem E. Taha, Chair

Unsteady aerodynamics emerges in several applications in mechanical and aerospace engineering such as the flutter problem, dynamic stall, bio-inspired flying robots, helicopters, and wind turbines. A leap in the design of these machines would only occur in the preliminary design phase upon investigating millions of design alternatives, which cannot and should not use high-fidelaity simulations. Therefore, the development of reduced-order models for unsteady aerodynamic loads will be of paramount importance for advancing these applications, which is the main focus of this dissertation.

The common (perhaps only) reduced-order models of unsteady aerodynamics in literature are based on potential flow theory, which is neither complete (invokes a closure condition) nor descriptive of viscous effects. While the Kutta condition is quite successful in small-angle of attack and large Reynolds number situations, it was originally devised for steady flows. Hence, its illegitimate use in unsteady environments may only be successful at low-frequencies. Therefore, there are numerous research reports that invoked another closure condition for potential flow in the unsteady case.

Three main contributions are achieved in this dissertation. First, realizing that the lift development and vorticity production are essentially viscous processes, a viscous extension

of the classical theory of unsteady aerodynamics is developed by matching the potential flow theory with a special boundary layer theory that pays close attention to the flow details in the vicinity of the trailing edge: the triple deck boundary layer theory. Based on this extension, a Reynolds-number-dependent lift frequency response is developed for the first time. The theory is validated against high-fidelity simulations of the Navier-Stokes equations showing a remarkable agreement. It is found that viscosity induces more phase lag at high reduced frequencies and low Reynolds numbers where the viscous effects are more pronounced.

Second, to extend the applicability of this viscous unsteady theory to account for arbitrary airfoil shapes, arbitrary kinematics, and wake deformation, a numerical method is developed. The developed numerical technique represents a viscous extension of the classical unsteady vortex lattice method (UVLM). In such an extension, Hilbert matrix algebra is exploited to show the relationship between the Kutta condition and the location of the control and collocation points on the panel. As such, the implicit Kutta condition in the UVLM is relaxed (corrected for) by updating the locations of these points within the panel at each time based on the viscous correction coming from the triple deck boundary layer theory, which is based on the instantaneous airfoil motion.

Finally, due to the fact that many aerial vehicles operate at moderate Reynolds number, which is prone to laminar-to-turbulent transition and theoretical approaches are not expected to perform efficiently in those conditions, the transition effects on the lift and circulation dynamics on a pitching airfoil are investigated numerically. It is found that transition induces significant nonlinearities in the lift and circulation dynamics even at very small pitching amplitudes down to half a degree. It is shown that this nonlinearity in the lift dynamics is attributed to the violation of the Kutta condition in this regime. Based on this connection, it is delineated how the potential flow theory can be extended with the aid of high-fidelity simulation data to capture the nonlinear transition effects.

Chapter 1

Introduction to the Thesis

1.1 Background and Motivation

The ability and strong legacy of potential flow theory have paved the path for aerodynamicists to labour it in a wide range of aeronautical engineering problems. Although its history goes back to D'Alambert and Euler (Dugas, 2012), the theory did not ripen until Prandtl (1904). In the the last century, most of the analytical developments of the wing (airfoil) aerodynamics in an incompressible flow, either steady or unsteady, were based on the Prandtl's potential flow theory. Based on his assumptions, for an infinitely thin airfoil, the viscous events are associated with a thin layer around the airfoil and a thin layer in the wake (unlike the steady flows, in unsteady flows, the wake should be considered) and the flow outside of these regions can be assumed irrotational. These concepts, in addition to assuming small disturbance to the mean flow (flat wake assumption), form the heart of the classical theory of (unsteady) aerodynamics (Birnbaum & Ackermann, 1923; Prandtl, 1918; Wagner, 1925; Theodorsen, 1935; Von Karman & Sears, 1938) and also provide the basis for the recent developments (Wang & Eldredge, 2013; Ford & Babinsky, 2013; Hemati *et al.*,

2014; Ramesh *et al.*, 2014; Darakananda & Eldredge, 2019; Epps *et al.*, 2019). However, this framework using potential flow is not complete and invokes a closure or auxiliary condition (e.g., the Kutta condition (Kutta, 1902)) since the strength and shape of the vortices that are shed form the sharp trailing-edge (TE) of the airfoil are not specified apriori. Applying the Kutta condition at the sharp edges completes the framework by providing strengths of the newly shed vortices. Consequently, one can use conservation of circulation to determine the value of the instantaneous circulation over the airfoil (bound circulation), which dictates the generated lift force through Kutta-Joukowsky theorem (Joukowsky, 1910). Moreover, it has been believed for decades that by allowing the sheets of vorticity on the airfoil and in its wake, the classical thin airfoil theory does not completely ignore viscous effects; that is, the boundary layer over the airfoil and the viscous shear layer in the wake are represented by the infinitely thin sheets of vorticity on the airfoil and wake, respectively (see a detailed discussion by Sears (1976*a*)). However, the application of the Kutta condition to unsteady flows has been controversial (see Crighton (1985) and the references therein). Although this framework is indeed for a linearized and high Reynolds number flow at small angles of attack, it has been extensively used at low Reynolds number flows (e.g., biological flyers) relying on the facts that (i) there is no sharp stall (a smooth lift variation over a broad range of angles of attack (Dickinson *et al.*, 1999), (ii) the shear force contribution to the aerodynamic loads is minimal, as observed in the experimental study of Dickinson *et al.* (1999) and the computational results of Wang (2000) and Ramamurti & Sandberg (2002).

As expected, all the analytical theories in steady or unsteady aerodynamics were developed for simple geometries such as a flat plate or a cylinder etc., under simplifying assumptions like flat wake and the types of motion that lend themselves to analytical solutions such as a step input, a simple harmonic motion or a constant speed motion. Due to the ability of the potential flow framework to capture essential physics of the flow, scholars attempted to adopt numerical approaches based on this framework. The most famous one is the vortex lattice method developed by Falkner (1943), which can accommodate any airfoil shape subjected

to any arbitrary input and allows for the wake deformation. In this method, the shape of the airfoil is represented by its camberline and is divided into finite number of panels with a vortex of unknown strength sitting on each of them and the airfoil motion is accommodated by the condition of flow tangency for impermeable surfaces (no-penetration boundary condition) that gives the strength of the vortices. Then, utilizing Bernoulli's equation, the pressure field on the airfoil is obtained and the aerodynamic loads can be calculated. The vortex lattice method is a simple and efficient tool that is employed in variety of aeronautical and aerospace engineering applications (Belotserkovskii, 1977; Katz & Maskew, 1988; Smith, 1996; Stanford & Beran, 2010).

The Unmanned Aerial Vehicles (UAV) and Micro Air Vehicles (MAV) are the two most important examples that renewed interest in the unsteady aerodynamics subject in the past two decades (Mueller & DeLaurier, 2003; Ansari *et al.*, 2006*a*). There are many reasons that why the classical aerodynamics models may not be sufficiently accurate for these new concepts and further research is required to extend and modify the classical models to be applicable in modern aerodynamics. For example, in many scenarios where the aerodynamics of a flapping bird or an insect is of interest, the body (airfoil) experiences high angles of attack and operates in the low-to-moderate Reynolds numbers where the underpinning assumptions of the potential flow are not valid. Therefore, scholars seek new methods to extend the classical approaches to be suitable for modern aerodynamics applications (Ramesh *et al.*, 2014; Nguyen *et al.*, 2016; Mesalles Ripoll *et al.*, 2019). Since the Kutta condition acts as the bridge between potential flow and viscous flow, further investigation on this complementary condition in the potential flow framework is needed that leads to viscous extension of potential flow approaches.

1.2 Application of Potential Flow in Unsteady Aerodynamics

In unsteady aerodynamics, the goal is to find the aerodynamic loads on a moving airfoil (wing). In this thesis, following the classical methodologies, it is assumed that the flow is incompressible with high Reynolds number and the airfoil deflections are small. Based on these assumptions, the continuity equation and the non-linear Navier-Stokes partial differential equations can be reduced to the linear Laplace equation for velocity potential and Bernoulli's equation for pressure field. It is known that the superposition principle can be applied on the linear differential equations to construct the solution. There are many functions that can satisfy the Laplace equations, such as a source, sink, doublet, vortex and free stream (e.g. a constant value), which are called elementary functions or singularities. Combining these singularities, it is possible to construct the flow field around different objects, which is a typical chapter in all the elementary fluid mechanics courses to study the steady flow. In the case of an unsteady flow, for example when the object is moving, setting up the problem is more involved and requires special techniques. There are several tools to be utilized in order to develop an unsteady aerodynamic model in the potential flow framework. Since the focus in this dissertation is on the unsteady aerodynamics modeling, assume a moving flat plate (which represents the airfoil or the lifting surface) in a fluid medium. The domain of the aforementioned setup is called plate domain. It is a common practice to conformally map the plate domain ($z - plane$) into the cylinder domain($\zeta - plane$) (see figure 1.1) through Kutta-Joukowsky transformation as

$$z = \xi + \frac{b^2}{4\xi}, \tag{1.1}$$

where $z = x + iy$ is the coordinate in the plate domain and $\xi = \zeta + i\eta$ is the coordinate in the cylinder domain.

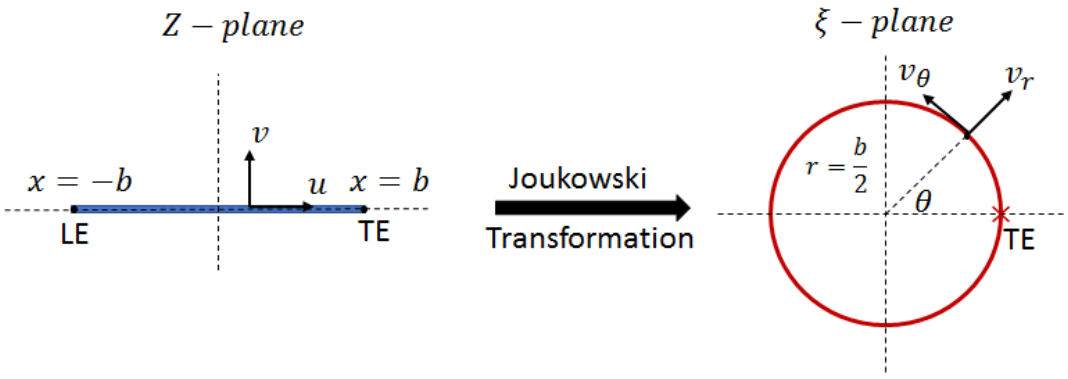

Figure 1.1: Conformal map between the flat plate of length $2b$ ($-b \leqslant x \leqslant b$) to a circle of radius $b/2$ ($0 \leqslant \theta \leqslant 2\pi$)

Utilizing equation (1.1), a cylinder of radius $b/2$ and its surrounding flow field can be confromally mapped to the flow field around a flat plate of length $2b$. Generally, formulation of the problem in the cylinder domain is more convenient as working with potential function of source/sinks and vortices are easier in the cylinder domain. The relation between the coordinate on the plate surface and the cylinder surface can be written as $x = b\cos\theta$. Furthermore, since $dW/dz = dW/d\xi.(dz/d\xi)^{-1} = u - iv$ (where W is the complex potential function) and $dW/d\xi = e^{-i\theta}(v_r - iv_\theta)$, by using equation (1.1) to find $dz/d\xi$ and substituting $\xi = \frac{b}{2}re^{i\theta}$, the velocities on the plate surface (u, v) are related to the velocities on the cylinder surface (v_r, v_θ) by $u = -v_\theta/2\sin\theta$ and $v = v_r/2\sin\theta$. It can be immediately seen that $\theta = 0$, which corresponds to the TE of the cylinder, is a singularity unless $v_\theta = 0$ (note that automatically $v_r = 0$ due to no-penetration or no flow through boundary condition). This mathematical trick, $v_\theta = 0$, to remove the singularity from TE is called Kutta condition. In the plate domain, the equivalent representation of the Kutta condition is no pressure loading or zero circulation or vanishing velocity difference on the top and bottom surfaces at the plate TE. This representation essentially means that the flow separates from the plate right at the TE station and there is no vorticity jump at that location. Having the velocity potential Φ in

the plate domain and using unsteady Bernoulli's equation given by

$$\rho\Phi_t + \frac{1}{2}\rho\left(\vec{\nabla}\Phi.\vec{\nabla}\Phi\right) + P + \rho g z = F(t), \tag{1.2}$$

the pressure distribution on the top and bottom surfaces can be obtained. In equation (1.2), Φ_t is the time derivative of the velocity potential, $\vec{\nabla}\Phi(=\vec{u})$ is the gradient of the velocity potential that gives the velocity vector $\vec{u}$, P is the fluid pressure and ρ is the fluid density. The constant of integration $F(t)$ is calculated by considering the freestream properties as $F(t) = P_\infty + \frac{1}{2}\rho V_\infty^2$ where P_∞ is the freestream pressure far from the plate and V_∞ is the freestream velocity. Note that in the derivation of $F(t)$, it is assumed that the Φ_t at ∞ is zero ($\Phi_t|_\infty = 0$), which corresponds to the constant freestream velocity. If the freestream velocity is time-varying, then $\Phi_t|_\infty$ possesses a non-zero value, which is not the case in this dissertation. If $\vec{u}$ is linearized around V_∞ meaning $\vec{u} = (V_\infty + \Delta u)\hat{i} + (\Delta u)\hat{j}$ and equation (1.2) is used to calculate the pressure on the top and bottom surfaces of the plate, then the lift force coming from the integration of the top and bottom surfaces pressure difference is written as

$$L(t) = 2\rho\left[\int_{-b}^{b}(\Phi_t(x)dx) + V_\infty\Phi_{TE}\right]. \tag{1.3}$$

Note that in equation (1.3) it is assumed that Φ_{LE} is zero. This assumption is justified based on the fact that it is expected the stagnation point to be in the vicinity of leading-edge (LE) and the resulting pressure possesses high values. As it can be seen in equation (1.3) the only unknown parameter is the velocity potential Φ. It can be shown that the velocity potential is correlated to the tangential velocity on the cylinder as

$$\Phi(\theta) = \frac{-b}{2}\int_\theta^\pi v_\theta(\tau)d\tau, \tag{1.4}$$

where τ is an arbitrary integration variable. As a result, the whole problem of finding the lift force on the moving flat plate boils down to finding the tangential velocity on the cylinder (when the plate is conformally mapped to the circle). In order to use the velocity potential on the cylinder given by equation (1.4) to find the lift force, the x coordinate in the integral in the right hand side of equation (1.3) is changed with θ by $x = b\cos\theta$ and is written as $b\int_{\pi}^{0} \Phi_t(\theta)\sin\theta d\theta$. One important difference between the steady and unsteady aerodynamics models is that the wake should be considered in the latter. In the presence of wake, Kelvin's law of zero total circulation ($\frac{d\Gamma_{total}}{dt} = 0$) should be satisfied. Since it is assumed that the fluid and plate are at rest at $t = 0$ and the total circulation Γ_{total} is zero, it remains zero for all the time resulting in

$$\Gamma_{bound} = -\Gamma_{wake}, \tag{1.5}$$

where Γ_{bound} is the total circulation on the plate and Γ_{wake} is the total wake circulation.

1.3 Summary of Theodorsen Model

Theodore Theodorsen (1935) developed an unsteady aerodynamics model for a pitching-plunging flat plate. This problem traces its roots back to the major issue of the first generation aircraft suffering from structural failure and stability loss which culminated in the theory of wing oscillations (Von Baumhauer & Koning, 1923). Since this problem was dealing with high Reynolds number flows and low angles of attack configurations, the potential flow theory was the best candidate for solving the aerodynamics side of the flutter problem. Exploiting the tools and concepts described in the previous section, Theodorsen managed to solve the unsteady aerodynamics problem of a harmonically pitching-plunging airfoil (see figure 1.2: the distance between the hinge and mid-chord point is ab) that is coupled with the structural dynamics equation to provide flutter boundaries.

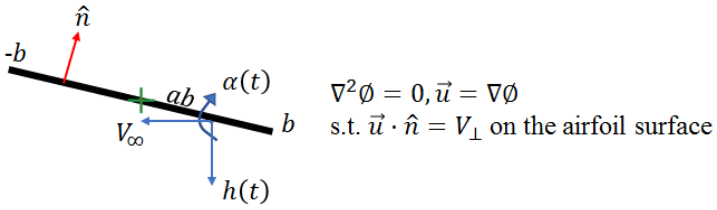

Figure 1.2: A generic setup for a pitching-plunging flat plate

He tackled the problem by formulating it in the cylinder domain and dividing the aerodynamic forces into two different categories: non-circulatory and circulatory. In the non-circulatory part, the motion of the cylinder, which corresponds to the motion of the flat plate through Kutta-Joukowsky transformation, is accommodated. To do so, a distribution of sources/sinks of unknown strength $Q(\theta)$ are placed on the cylinder. The no-penetration boundary condition on the cylinder surface ($v_r(\theta) = 0$) provides a means to obtain $Q(\theta)$. In fact, we are dealing with time-varying sources/sinks such that the velocity produced by them cancels the velocity induced by the pitching motion $\alpha(t)$, plunging motion $h(t)$ and the free stream velocity V_∞. The induced tangential velocity by this distribution of sources and sinks is

$$v_{\theta_{NC}}(\theta) = -2\left[(V_\infty \sin\alpha + \dot{h}\cos\alpha + \dot{\alpha}ab)\cos\theta + \frac{\dot{\alpha}b}{2}\cos 2\theta\right] \tag{1.6}$$

Note that, $\sin\alpha$, and $\cos\alpha$, are replaced by α and 1, respectively, as the deflections are assumed to be small. Then, by utilizing equation (1.4) the velocity potential on the plate will be

$$\Phi_{plate} = b\left[(V_\infty\alpha + \dot{h} + \dot{\alpha}ab)\sin\theta + \frac{\dot{\alpha}b}{4}\sin 2\theta\right], \tag{1.7}$$

which is plugged into equation (1.3) to provide the non-circulatory lift L_{NC} as

$$L_{NC} = \pi\rho b^2 a_{\perp\frac{1}{2}}, \tag{1.8}$$

where, $a_{\perp\frac{1}{2}} = V_\infty\dot{\alpha} + \ddot{h} - \ddot{\alpha}ab$ (after linearization), is the acceleration of the mid-chord point of the plate. The non-circulatory lift is commonly termed as "added mass" lift as it can be interpreted as the required force to move the surrounding fluid (in fact $\pi\rho b^2$ can be regarded as the mass per unit length). This force which appears in the right hand side of the flutter formulation (similar to all other aerodynamic forces) can be moved to the left hand side and be added to the inertial forces acting as an "added mass" term. The important feature of the L_{NC} is that it is an instantaneous force due to the airfoil motion as there is a direct algebraic relation between the L_{NC} and the acceleration term. Therefore, no dynamics is involved in the forces of this category. One significant outcome of this solution is the tangential velocity at the TE of the cylinder, which can be calculated by setting $\theta = 0$ in equation (1.6) as $v_{\theta_{NC}}(\theta = 0) = -2v_{3/4}(t)$. As a result, the normal velocity at the three-quarter-chord of the plate $v_{3/4}(t)$ is directly proportional to the tangential velocity of the cylinder at TE. Based on the previous section, in order to satisfy the Kutta condition, $v_{\theta_{TE}}$ must be zero. In consequence, it is expected that the circulatory portion of the lift force cancels the generated velocity by the non-circulatory portion to remove the singularity at the TE.

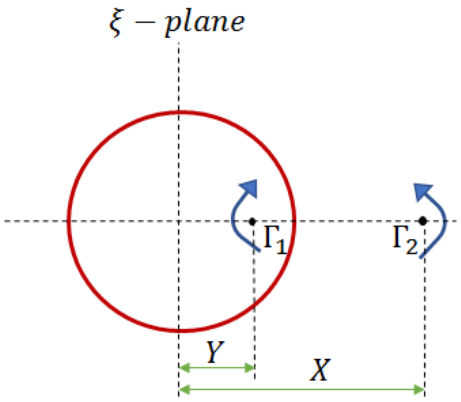

Figure 1.3: Setup of the Theodorsen problem in cylinder domain for the circulatory portion of the lift

As mentioned before, in the unsteady flows, the wake behind the plate (airfoil) must be modeled. For this purpose, Theodorsen added a vortex of strength Γ_2 outside of the cylinder with the distance X to the center as shown in figure 1.3. This vortex disturbs the no-penetration boundary condition on the circle, which was already satisfied in the non-circulatory part. In other words, the cylinder will not remain a streamline by just considering a single vortex (Γ_2) in the wake. Therefore, an image vortex Γ_1 is placed inside the cylinder with the distance Y to the center, which sits on the line connecting the center of the wake vortex Γ_2 and the center of the cylinder. Before trying to make the cylinder surface a streamline again, it is convenient to satisfy the Kelvin's circulation theorem based on equation (1.5), which gives $\Gamma_1 = -\Gamma_2$. So, we are dealing with a pair of counter-rotating vortices with equal strength. Now, it is desired to find Y in terms of X such that the superposition of the pair of vortices keeps the cylinder of radius $b/2$ a streamline, which results in $Y = b^2/4X$. Then, the tangential velocity induced by the pair of vortices on the cylinder is calculated as

$$v_{\theta_C} = \frac{-\Gamma_1}{\pi b} \frac{X^2 - b^2/2}{X^2 + b^2/4 - bX\cos\theta}. \tag{1.9}$$

Thus, the tangential velocity at the TE ($\theta = 0$) can is given by $v_{\theta_C}(\theta = 0) = \frac{-\Gamma_1}{\pi b} \frac{X+b/2}{X-b/2} = \frac{-\Gamma_1}{\pi b} \sqrt{\frac{Z+b}{Z-b}}$, where Z is the coordinate of the wake vortex in the plate domain corresponding to X in the cylinder domain (Z and X are related to each other through Joukowsky transformation). In the next step, the wake vortex Γ_2 is substituted with a distribution of vortices $\gamma_w(z,t)$. It is important to elucidate that this substitution does not disturb the Kelvin's condition as Γ_1 is assumed to adapt itself with the wake vortices distribution to keep the cylinder a streamline and the Kelvin's condition satisfied. In order to satisfy the Kutta condition, the tangential velocity of the non-circulatory and circulatory parts of the solution is considered ($v_{\theta_{NC}}(\theta = 0) + v_{\theta_C}(\theta = 0) = 0$), and the integral equation for circulation is

derived as

$$\frac{1}{\pi b}\int_{b}^{\infty}\gamma_w(z,t)\sqrt{\frac{z+b}{z-b}}dz = 2v_{3/4}(t). \tag{1.10}$$

Furthermore, substituting v_{θ_C} from equation (1.9) in equation (1.4) and using equation (1.3), $\Phi_{TE} = \frac{\Gamma_1}{2}$ and the circulatory lift is written as

$$L_c(t) = \rho V_\infty \int_{b}^{\infty}\gamma_w(z,t)\frac{z}{\sqrt{z^2-b^2}}dz. \tag{1.11}$$

So far, no particular assumption has been made on the motion type. If the airfoil undergoes harmonic motion with low deflections at zero mean angle of attack, it is fair to assume a harmonic and flat wake convecting with V_∞, which means $\gamma_w(z,t) = \gamma_w(z_0, t-\frac{z-z_0}{V_\infty})$ where z_0 is the location of the current wake vortex $\gamma_w(z,t)$ at $t = t_0$. Based on these simplifications, we obtain

$$\gamma_w(z,t) = \bar{\gamma_w} e^{iw(t-\frac{z}{V_\infty})} \tag{1.12}$$

It is worth pointing out that the extension of equation (1.12) for a non-zero mean angle of attack is an involved process and has not been presented in the literature according to the author's knowledge. Now, by combining equations (1.10) and (1.11) and utilizing equation (1.12), the circulatory lift L_c can be written as

$$L_c = L_{QS}\frac{\int_1^\infty e^{-ik\sigma}\frac{\sigma}{\sqrt{\sigma^2-1}}d\sigma}{\int_1^\infty e^{-ik\sigma}\sqrt{\frac{\sigma+1}{\sigma-1}}d\sigma}, \tag{1.13}$$

where $L_{QS} = -2\pi b\rho V_\infty v_{3/4}(t)$ is the quasi-steady lift, $\sigma = \frac{z}{b}$ is the normalized coordinate

and $k = \frac{wb}{V_\infty}$ is the motion reduced frequency. The ratio of the two integrals in the right hand side of equation (1.13) is called Theodorsen function $C(k)$. Astonishingly, there is an analytical solution for Theodorsen function as

$$C(k) = \frac{H_1^{(2)}(k)}{H_1^{(2)}(k) + iH_0^{(2)}(k)}, \tag{1.14}$$

where $H_n^{(m)}$ is the Hankel function of m^{th} kind of order n. Unlike the non-circulatory lift where an instantaneous force is generated due to the plate motion, the circulatory lift possesses dynamics and there is a transfer function $C(k)$ between the input (motion) and output (lift) in this case, which is a function of reduced frequency. Lastly, the total lift force experienced by the flat plate is given by the summation of the non-circulatory (equation (1.8)) and circulatory lifts (equation (1.13)). For further details on the differences and connections between circulatory and non-circulatory lifts, the reader is highly recommended to read Taha & Rezaei (2019*b*).

1.4 Outline of the Thesis

The main focus of this work is to replace the Kutta condition in the classical efficient unsteady aerodynamics models with a viscous condition that contains viscous effects near the trailing edge. This goal is achieved by relaxing the Kutta condition in the potential flow framework and obtaining the strength of the generated singularity through triple-deck boundary layer theory. In chapter 2, it is shown that relaxing the Kutta condition introduces a singularity in the pressure distribution as expected. This singularity is integrable meaning that the resulting force and moment associate with that pressure distribution is finite. It is shown how the triple-deck boundary layer theory can be employed to find the strength of the singularity. This theory treats the flow in the vicinity of the TE, where there is a strong interaction between the upstream Blasius boundary layer and downstream Goldstein wake. We adopted

this approach by introducing a singularity in the pressure distribution of a moving plate and showed the modifications that need to be applied in the classical models. As a result, we developed a viscous unsteady aerodynamics model that unlike Theodorsen model, which is only a function of reduced frequency, it is a function of both Reynolds number and reduced frequency. The analytical results are validated against computational results at high and low Reynolds numbers. Lower amplitude of the circulatory lift transfer function and more phase lag, which are enhanced at lower Reynolds number, are the important outcomes. In chapter 3, based on the developed methodology in chapter 2, we tackle the Kutta condition in the well-known unsteady vortex method (UVLM). Unlike the Theodorsen analytical model described above where the Kutta condition is explicitly formulated and satisfied, the application of the Kutta condition in UVLM is subtle. First, by realizing that the matrix system appearing in UVLM is a special kind called Hilbert matrix and by utilizing the Hilbert matrices algebra, we show how Kutta condition is implicitly applied in UVLM by dictating the layout of each panel. Then, it is attempted to replace the Kutta condition by the viscous condition from the triple-deck theory. This approach results in a time-varying layout of each panel. Then, the extended UVLM is used for several different motion inputs and very good results are obtained compared to the CFD results, which show a significant enhancement compared to the original inviscid UVLM. The captured dynamics of the aerodynamic forces in the previous chapter is linear. It is observed that under Laminar-to-turbulent transition, the lift (circulation) dynamics is no longer linear even under low deflections and low reduced frequencies. In chapter 4 by realizing that the amount of circulation of the airfoil is dictated by the Kutta condition, we use the numerical simulations to study the effect of transition on the circulation dynamics. In fact, in unsteady flows, the Kutta condition relates the amount of vorticity generated in the boundary layer to the vorticity being shed into the wake. This vorticity flux can be obtained by the velocities and pressures at the edges of the top and bottom boundary layers. It is shown that in the derivation of the classical Kutta condition, the pressure difference at the boundary layer edges was neglected. This

omission is in accordance with the boundary layer theory results where no pressure rise across the boundary layer is expected. However, the complicated flow-field near the trailing edge and the presence of transition can violate the boundary layer assumptions, resulting in a noticeable pressure rise in the boundary layer. After validating our numerical setup with an experimental study, we use the fact that the edge of the boundary layer is detectable under these circumstances and elaborate on the non-linear behavior of the circulation dynamics. Specifically, we show the contribution of each term in the exact definition of Kutta condition and study the effect of important parameters such as Reynolds number, reduced frequency and pitching amplitude through time-history and FFT analysis. The results are compared with the Theodorsens potential-flow based theory and the deviations are explained. Finally, chapter 5 provides the conclusion of this thesis and suggests a few projects for future work.

Chapter 2

Viscous Lift Frequency Response Problem Using Triple-Deck Theory

2.1 Background

Recalling the historical development of the classical theory of unsteady aerodynamics (unsteady aerodynamics of wings in an incompressible flow), we realize that it is mainly based on the following fundamental assumption due to Prandtl (1924) and Birnbaum (1924): For a *high Reynolds number, small angle of attack* flow around an *infinitely thin airfoil*, separation or sheets of vorticity are shed from the sharp edges only and the flow outside of these sheets can be considered irrotational. This brilliant assumption is quite accurate in the stated regime and was extremely enabling. Because an incompressible irrotational flow is simply governed by the Laplace equation, which is a linear equation admitting superposition, this framework was the basis for almost all analytical theories of aerodynamics in the linear regime: the steady ones such as the thin airfoil theory (Birnbaum & Ackermann, 1923; Glauert, 1926), Prandtl's lifting line theory (Prandtl, 1918), Weissinger's ex-

tended lifting line theory (Weissinger, 1949), the lifting surface theory (Truckenbrodt, 1953; Multhopp, 1950) which evolved to the vortex lattice/panel method; and the unsteady ones such as Theodorsen's lift frequency response (Theodorsen, 1935), Wagner's lift step response (Wagner, 1925), Kussner's sharp edged gust problem (Küssner, 1929), the developments of Von Karman & Sears (1938) among others. In addition, it is still acting as the pillar of many of the recent developments (Jones, 2003; Yongliang *et al.*, 2003; Pullin & Wang, 2004; Ansari *et al.*, 2006*b*; Michelin & Smith, 2009; Tchieu & Leonard, 2011; Wang & Eldredge, 2013; Ramesh *et al.*, 2013; Taha *et al.*, 2014; Ramesh *et al.*, 2014; Yan *et al.*, 2014; Li & Wu, 2015; Hussein *et al.*, 2018; Xia & Mohseni, 2017). However, this framework using potential flow is not complete and requires a closure or auxiliary condition (e.g., the Kutta condition). In particular, it does not quantify the vorticity shed at the sharp trailing edge. This quantity is essential as it immediately determines the circulation over the airfoil through conservation of circulation, which in turn dictates the lift via the Kutta-Joukowsky lift theorem Kutta (1902); Joukowsky (1910). Therefore, the potential flow theory *alone* cannot predict the generated lift force. However, if the potential flow theory is supplied by the generated lift force, it will provide a reasonable (sometimes accurate) representation of the flow field even in unsteady high angles of attack situations, as shown in the recent efforts of Ford & Babinsky (2013); Hemati *et al.* (2014). They basically showed that by using the "right" auxiliary condition to determine the circulation development over the airfoil, the resulting potential flow field is quite close to the actual flow field even at unsteady high angle of attack situations where vortices also shed from the leading edge. We interpret these results from a dynamical system perspective as an *observability* result: the flow dynamics are observable from the lift force (or circulation) output measurement and the observer (a reduced-order observer) is given by the potential flow dynamics. That is, given the generated aerodynamic forces, one can estimate (observe) the flow dynamical states (e.g., the velocity field). However, the generated aerodynamic forces are the primary unknowns of interest to an aerodynamicist.

The most common auxiliary condition that has been typically used throughout the history

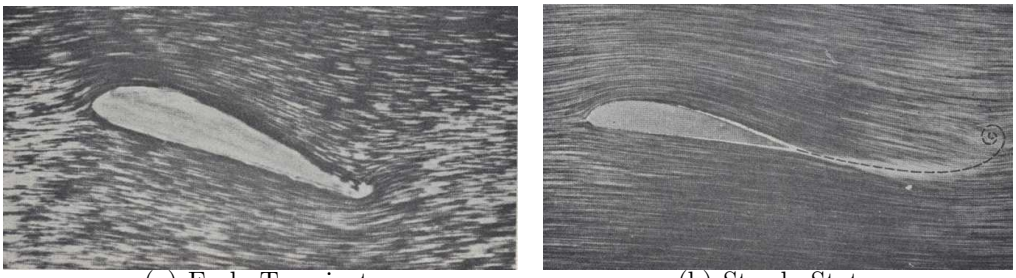

(a) Early Transient. (b) Steady State.

Figure 2.1: Visualization of the impulsive start flow around an airfoil (Tietjens & Prandtl, 1934, pp. 296-299). During the transient period, the flow rotates around the trailing edge. After reaching steady state, the flow leaves the trailing edge smoothly and the Kutta condition is satisfied.

of potential flow aerodynamics is the Kutta condition. It completes the potential flow framework by providing the circulation around the airfoil (equivalently the generated lift force). It has several representations: smooth flow-off the trailing edge, no flow around the trailing edge, or that the stagnation point is right at the trailing edge, among other forms. It is quite accurate for a *steady* flow (at high Reynolds number and small angle of attack) as can be seen from Prandtl's flow visualizations in his water channel early in the past century. Figure 2.1(b) shows smooth flow-off the trailing edge and that there is no flow around the trailing edge from the lower surface to the upper surface or vice versa; that is, the stagnation point is at the trailing edge and the Kutta condition is essentially satisfied. Indeed, it is a paradigm for engineering ingenuity where a mathematical condition is inferred from physical observations. However, for an unsteady case as the one shown in figure 2.1(a), it is already known that, in the early transient moments after an impulsive start, the flow goes around the trailing edge from the lower surface to the upper surface and the stagnation point is on the upper surface (Tietjens & Prandtl, 1934, pp. 158-168; Goldstein, 1938, pp. 26-36; Schlichting & Truckenbrodt, 1979, pp. 33-35).

The application of the Kutta condition to unsteady flows has been controversial. The reader is referred to the articles by Sears (1956, 1976*b*) and the review article on the topic by Crighton (1985), although, the latter's definition of the Kutta condition is different from the

current discussion or that by Sears. Crighton defined the Kutta condition as a condition of least singularity at the edge, which may even come from viscous considerations (i.e., boundary layer theory). However, in this case, we (similar to Sears viewpoint) would consider it as a viscous extension of the Kutta condition. The need for an auxiliary condition alternative to Kutta's can be traced back to the work of Howarth (1935) with a research flurry on the applicability of the Kutta condition to unsteady flows in the 1970's and 1980's (Basu & Hancock, 1978; Daniels, 1978; Satyanarayana & Davis, 1978; Bass *et al.*, 1982; Crighton, 1985). The present research was partly motivated by the failure to capture an accurate flutter boundary (Rott & George, 1955; Abramson & Chu, 1959; Henry, 1961; Abramson & Ransleben, 1965). Recall that the flutter phenomenon is simply an interaction between unsteady aerodynamics and structural dynamics. In addition, since structural dynamics could be captured with good accuracy (e.g., exact beam theory), it has been deemed that the flaw stems from the classical unsteady aerodynamic theory, particularly the Kutta condition, as suggested by Chu (1961) and Shen & Crimi (1965) among others. Moreover, since these deviations occurred even at zero angle of attack or lift (Woolston & Castile, 1951; Chu & Abramson, 1959), it was inferred that there is a fundamental issue with such a theory that is not merely a higher-order nonlinear effect (Chu, 1961). Therefore, there was almost a consensus that the Kutta condition has to be relaxed particularly at large frequencies, large angles of attack and/or low Reynolds numbers (Abramson *et al.*, 1967; Savage *et al.*, 1979; Satyanarayana & Davis, 1978). In fact, Orszag & Crow (1970) regarded the full-Kutta condition solution as "indefensible".

Interestingly, this dissatisfaction with the Kutta condition and the need for its relaxation has been recently rejuvenated. Several recent efforts invoked an alternative auxiliary condition to Kutta's. Ansari *et al.* (2006*b*,*c*) proposed a modified version of the Kutta condition, particularly during rapid pitching near stroke reversals, to avoid creating artificially strong vortices; the idea was that the pitch maneuver is so acute that the fluid may actually flow around the edge not along it. More recently, Ford & Babinsky (2013) experimentally studied

the leading edge vortex (LEV) dynamics over an impulsively started flat plate. They also developed a potential flow model that consists of a bound circulation, free LEVs and free trailing edge vortices. They determined the positions and strengths of the vortices by applying the γ_2-method (Graftieaux *et al.*, 2001) to their PIV measurements. Based on these values, they determined the value of the bound circulation that minimizes the deviation between the potential flow field and PIV measurements. During early stages, the optimum bound circulation was found to be considerably different from the Kutta's value (that ensures finite velocity at the trailing edge). In a similar setting, Hemati *et al.* (2014) improved their previous varying-strength discrete vortex model (Wang & Eldredge, 2013) by relaxing the Kutta condition via applying optimal control theory to determine the strengths of the recently shed vortices that minimize the discrepancy between the potential flow predicted forces and measurements, which was also found to be considerably different from Kutta's values.

Ramesh *et al.* (2014) developed a new LEV shedding criterion based on the first (singular) term in the well-known Fourier series representation of the bound circulation distribution in the classical thin airfoil theory. This term, which they called Leading Edge Suction Parameter (LESP), is a measure of leading edge suction (Garrick, 1937). Ramesh *et al.* (2014) showed that there is a critical value of the LESP (depending on airfoil shape and Reynolds number) that determines whether the flow is attached or separated at the leading edge, irrespective of the motion kinematics. Their LESP criterion not only predicts the onset and termination of LEV shedding but also the strength of the newly shed LEV, thereby removing the need for an auxiliary condition at the leading edge. Nevertheless, they applied the Kutta condition at the trailing edge. It is also noteworthy to mention the recent efforts of Xia & Mohseni (2017) who extended Jones (2003) auxiliary condition at the sharp edges of a flat plate to the case of a finite trailing edge angle. Jones (2003) used the Rott-Birkhoff equation (Rott, 1956; Birkhoff, 1962) to model the dynamics of free continuous vortex sheets emanating from the leading and trailing edges. He satisfied the Kutta condition at both

edges by imposing boundedness of the flow velocity everywhere. This formulation lead to the edge condition: the vortex sheet sheds tangentially to the plate. However, this result is applicable only to a flat plate or an airfoil with cusped trailing edge. Xia & Mohseni (2017) extended it to the case of an airfoil with finite trailing edge angle by requiring that the flow velocity be tangential to the vortex sheet at the edge. Using this condition, together with conservation of momentum, Xia & Mohseni (2017) derived two equations that generalize Jones edge condition (governing the shedding of a continuous vortex sheet from a sharp edge with zero angle) to the case of a finite edge angle.

Indeed, the development of an auxiliary condition that replaces the Kutta condition in highly unsteady flows is a pressing issue that persisted over almost a century. Since the vorticity generation and lift development are essentially viscous processes, a purely inviscid theory of unsteady aerodynamics might be fundamentally flawed. Here, we develop a viscous extension of the classical theory of unsteady aerodynamics. The problem setup, governing equations and boundary conditions are similar to the Theodorsen model shown in figure 1.2. The main difference is the way that the amount of bound circulation is calculated in the viscous extension. Similar to almost all the classical theories, Theodorsen used the Kutta condition for this purpose. However, in this effort, we relax the Kutta condition and show a new singularity that emerges at the trailing-edge with unknown strength, which cannot be found using just potential flow framework. Therefore, we revisit the unsteady boundary layer triple deck theory developed by Brown & Daniels (1975) and Brown & Cheng (1981) to develop a viscous extension of Theodorsen's lift frequency response. In section section 2.3, we extend their effort (on a flat plate pitching around its mid-chord point) to the more general case of an arbitrarily-deforming thin airfoil (or time-varying camber), while correcting for few minor mistakes. In section 2.4, using a describing function formulation, we develop for the first time a viscous (Reynolds number dependent) lift frequency response. Then, we perform a computational simulation using ANSYS Fluent for a harmonically pitching airfoil (NACA 0012) to assess the validity of the obtained results from the unsteady triple deck theory.

Finally, we provide in section 2.6 a physical explanation of the obtained results, namely a discussion on the relation between the viscosity-induced lag in circulation development and the Kutta condition. This chapter follows our journal (Taha & Rezaei, 2019*a*) and conference (Taha & Rezaei, 2018) articles.

2.2 The Boundary Layer Triple Deck Theory

During his PhD study under Prandtl, Blasius (1908) solved Prandtl's boundary layer equations subject to a no-slip boundary condition on a flat plate. Via similarity transformation, he obtained the celebrated Blasius solution resulting in a boundary layer thickness of order $R^{-1/2}$, where R is the Reynolds number based on the plate chord length. Later, Goldstein (1930) solved the exact same equations subject to a different boundary condition: zero stress on the wake centerline behind the flat plate. His solution for the stream function near the edge constituted of Blasius function at the edge plus corrections in the form of $x^{1/3}$, where x is the distance downstream of the trailing edge. As such, Goldstein's solution is not uniformly valid as $x \to 0$: the transverse velocity has a singularity at $x = 0$. Moreover, when taking into account the effect of Goldstein's boundary layer on the outside potential flow, it induces an adverse pressure gradient upstream of the edge (above the Blasius layer) and a favorable pressure gradient downstream of the edge (Messiter, 1970). That is, the removal of the plate's surface accelerates the flow behind the plate leading to a favorable pressure gradient. Therefore, in the vicinity of the trailing edge, there are two boundary layers interacting with each other. It is expected that neither Blasius nor Goldstein solution is valid in the immediate vicinity of the edge where the x-derivatives become large due to the abrupt change in the viscous boundary condition. The triple deck theory has been originally devised to model these local interactions near the trailing edge of an airfoil in steady flow due to the transition from a *modified* Blasius boundary layer with an adverse pressure gradient to a

modified Goldstein near-wake solution with a favorable pressure gradient (Crighton, 1985). In other words, the triple deck structure represents a solution to the discontinuity of the viscous boundary condition at the edge (Brown & Daniels, 1975): from a zero tangential velocity on the airfoil to a zero pressure discontinuity on the wake center line. As shown in figure 2.2, this interaction typically takes place over a short length of order $R^{-3/8}$, similar to Lighthill's supersonic shock-wave-boundary-layer interaction (Lighthill, 1953). Over this range, the correction in the boundary layer solution due to the non-zero pressure gradient becomes of the same order as the leading term (Messiter, 1970). Therefore, unlike the typical boundary layer theory where scaling (zooming) is applied to the y-axis only, the x-axis is also scaled in the triple deck theory to discern the details of such a transition. As shown in figure 2.2, aerodynamicists modeled this transition through three decks (triple deck theory): (i) the upper deck which consists of an irrotational flow outside of the main boundary layer; (ii) the main deck which consists of a Blasius-like layer, though it becomes inviscid; and (iii) the lower deck, which is a sub-layer inside the main boundary layer that takes care of the viscous boundary conditions on the centerline in the vicinity of the trailing-edge. The main and lower decks are governed by the full Navier-Stokes equations, although through the chosen scaling in each of them and keeping the leading terms, the obtained equations are reduced versions of Navier-stokes equations (similar to Prandtle's boundary layer equations). The upper deck ($y \sim R^{-3/8}$) is governed by the inviscid potential flow. The boundary conditions for the triple deck are as follows. In the upstream the solution should match to that of the perturbed Blasius solution and in the downstream to that of the perturbed Goldstein near wake solution. On the center line ($y = 0$), $u = 0$ for $x < x_{TE}$ and $\partial u/\partial y = 0$ for $x > x_{TE}$. Also, as $y \to \infty$ the outer potential flow solution should be recovered. The solution procedure is started by regarding the main deck and using the proper scaling (perturbation) in this region and expanding the velocities and pressure terms. By matching the obtained solution with the upstream Blasius and downstream Goldestein solutions, the unknown coefficients in the expansions of velocities and pressure in the main deck are derived. Then, it is observed

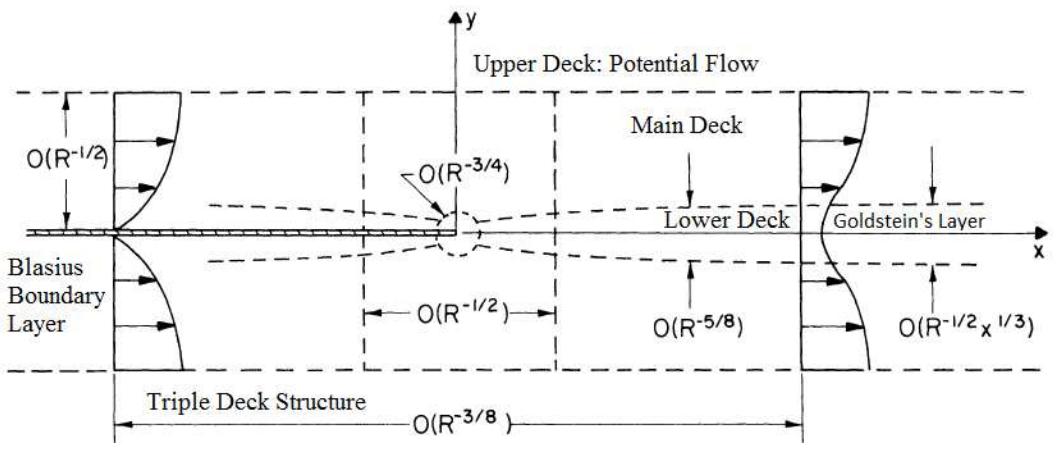

Figure 2.2: Triple deck structure and various flow regimes, adapted from Messiter (1970).

that this solution does not satisfy the viscous boundary conditions on the centerline and does not match with the potential flow solution as $y \to \infty$. Thus, the upper and lower decks are introduced to address these issues, and are asymptotically matched with the main deck solution as $y \to \infty$ and $y \to 0$, respectively. For more details, the reader is referred to the review articles (Stewartson, 1974, 1981; Smith, 1983; Messiter, 1983; Crighton, 1985, and the references therein).

One of the useful outcomes from the triple deck theory is its correction to the Blasius skin friction drag $C_D \simeq \frac{1.328}{\sqrt{R}}$, which is valid only for high enough Reynolds number. However, the triple deck correction

$$C_D \simeq \frac{1.328}{\sqrt{R}} + \frac{2.66}{R^{7/8}}$$

to the Blasius skin friction drag coefficient is in a very good agreement with both Navier-Stokes simulations and experiments down to $R = 10$ and even lower (Crighton, 1985). Another useful outcome from the triple deck theory, which is one stepping stone to the theory developed in this work, is the *trailing edge stall* concept and the viscous correction of the steady pressure distribution. This result is discussed next.

Stewartson (1968) and Messiter (1970) were the first to develop the triple deck theory for a flat plate in a steady flow at zero angle of attack. Brown & Stewartson (1970) extended such a work for a non-zero angle of attack in the order of $R^{-1/16}$. Over this range, the resulting adverse pressure gradient is of the same order as the favorable pressure gradient in the triple deck, leading to separation in the immediate vicinity of the trailing edge, which is called *Trailing Edge Stall*. To provide a viscous correction for the steady Kutta-Joukowsky lift, Brown & Stewartson (1970) introduced a singularity in the loading at the trailing edge.

Consider a flat plate with a semi-chord length b subject to a steady uniform flow U at an angle of attack α_s. Let $\tilde{x}$ be the plate coordinate normalized by b (i.e., $-1 \leq \tilde{x} \leq 1$ over the plate). Brown & Stewartson (1970) wrote the steady pressure distribution over the upper surface of the plate near the trailing edge (i.e., $\tilde{x} \to 1$) as [1]

$$P_s(\tilde{x} \to 1) = \rho U^2 \alpha_s \left[-\sqrt{\frac{1-\tilde{x}}{2}} + \frac{B_s/2}{2\sqrt{2}} \sqrt{\frac{1-\tilde{x}}{2}} + \frac{B_s/2}{b\sqrt{\frac{1-\tilde{x}}{2}}} \right], \tag{2.1}$$

where ρ is the fluid density and the pressure on the lower side is given by the negative of (2.1). The first term represents the potential flow pressure distribution with its leading edge singularity (at $\tilde{x} = -1$) and zero loading at the trailing edge (at $\tilde{x} = 1$). The second term represents a trailing edge singularity, which is supposed to be zero according to the Kutta condition. By contrast, Brown & Stewartson (1970) proposed to determine the value of B_s (trailing edge singularity) by matching the triple deck with the outer potential flow solution. Brown & Stewartson (1970) formulated such a problem and showed that the flow in the lower deck is governed by partial differential equations that are solved numerically for each value of $\alpha_e = R^{1/16} \lambda^{-9/8} \alpha_s$, where $\lambda = 0.332$ is the Blasius skin-friction coefficient. Jobe & Burggraf (1974) and Veldmann & Van de Vooren (1975) solved the $\alpha_e = 0$ case, while Chow & Melnik (1976) solved the case of $0 < \alpha_e < 0.45$ and concluded that the flow will

[1] Equation (2.1) is given as (2.2) by Brown & Stewartson (1970) and re-written in the terminology of this chapter.

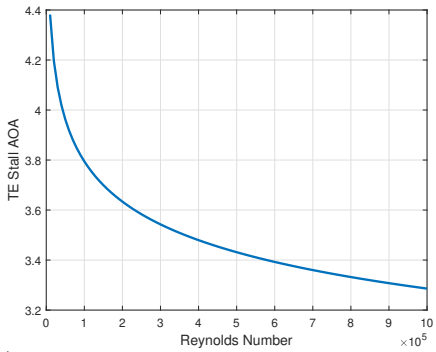

(a) Variation of the trailing edge stall angle of attack with Reynolds number.

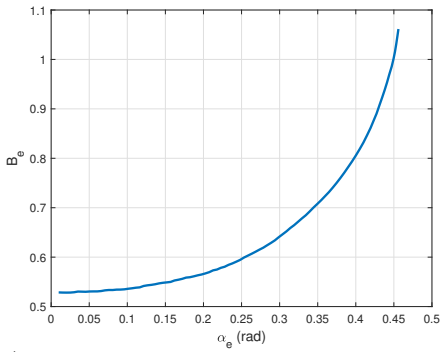

(b) Numerical solution of the steady lower deck equations for $0 < \alpha_e < 0.45$.

Figure 2.3: Results of the steady triple deck boundary layer theory. For 2.3(a), α_e is set to the trailing edge stall value (0.47) and the corresponding actual angle of attack α_s is determined from (2.2) based on the Reynolds number R. The trailing edge stall angle of attack decreases as R increases. Figure 2.3(b) is adapted from Chow & Melnik (1976).

separate from the suction side of the airfoil from the trailing edge at $\alpha_e = 0.47$ (trailing edge stall angle). This result leads to an inverse relation between Reynolds number and the actual trailing edge stall angle of attack, as shown in figure 2.3(a). This result yields quite a small value for the airfoil angle of attack before trailing edge stall: $\alpha_s = 3.1° - 4.2°$ for $R = 10^4 - 10^6$ (figure 2.4).

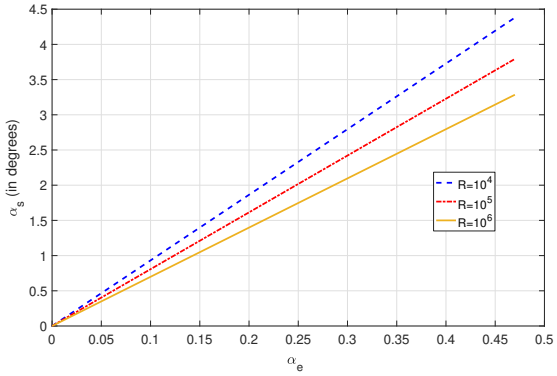

Figure 2.4: Variation of the α_s with α_e at three different Reynolds numbers

The numerical solution by Chow & Melnik (1976) provides B_e as a nonlinear function of α_e, which is represented here in figure 2.3(b), where

$$\alpha_e = \alpha_s \epsilon^{-1/2} \lambda^{-9/8}, \quad B_s = 2b\epsilon^3 \lambda^{-5/4} B_e(\alpha_e), \tag{2.2}$$

where α_s, α_e are in radians, and $\epsilon = R^{-1/8} \ll 1$ (Stewartson, 1968). In other words, they provide $B_s = B_s(\alpha_s)$: the strength of the trailing edge singularity in terms of the angle of attack. Using this approach, we determine the nonlinear variation of the steady lift coefficient C_L with the angle of attack α_s up to the trailing edge stall angle, as shown in figure 2.5

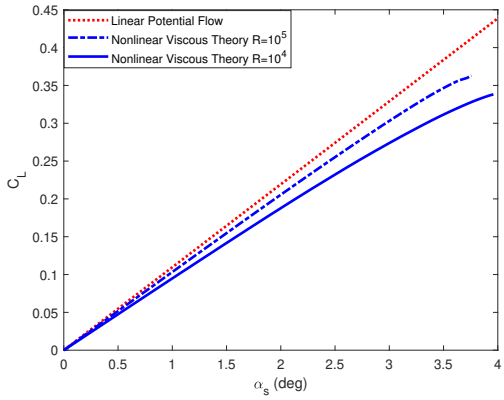

Figure 2.5: Nonlinear steady C_L-α relation from the viscous boundary layer theory. It is constructed based on the steady version of the theory detailed below, equivalently the viscous steady theory of Brown & Stewartson (1970) and the numerical solution of Chow & Melnik (1976). The C_L-α relation becomes more nonlinear as R decreases and there is a lift drop towards trailing edge stall.

2.3 Unsteady Triple Deck Theory

2.3.1 Background and Main Concept

Brown & Daniels (1975) were the first to extend the steady triple deck theory to the case of a high-frequency (ω), small-amplitude oscillatory pitching flat plate. Unlike the steady case, there is a Stokes layer near the wall that is of order $\sqrt{\nu/\omega}$ where the viscous term is balanced by the time-derivative term in the equations. Brown and Daniels assumed that the Stokes layer and the lower deck have the same thickness, which results in a reduced frequency $k = O(R^{1/4})$, where $k = \frac{\omega b}{U}$. This range is too large for engineering applications: $k \simeq 5-15$ for $R = 10^4 - 10^6$. Then, the matching between the adverse pressure gradient due

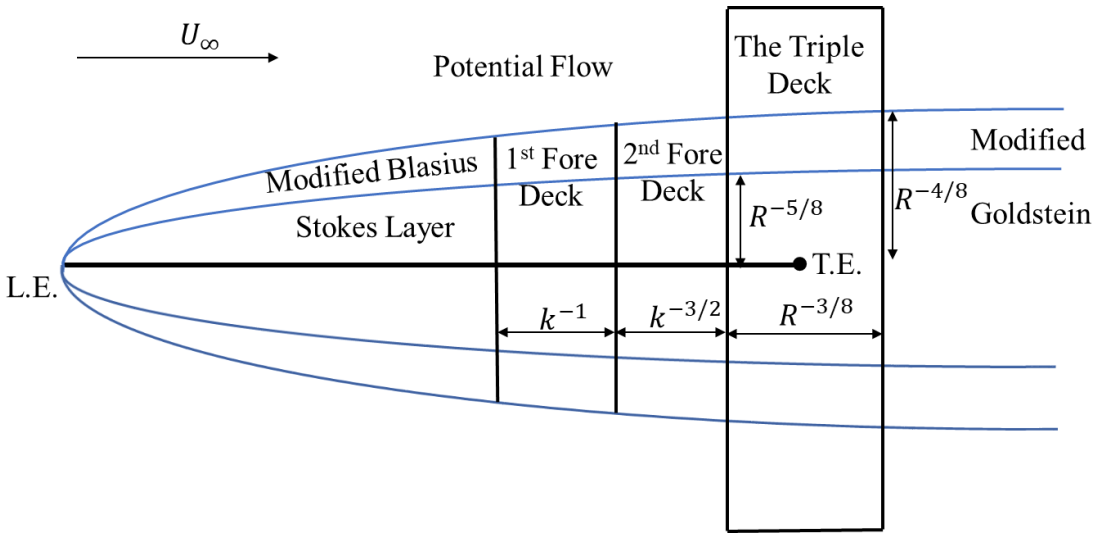

Figure 2.6: Low frequency triple deck structure and flow regimes.

to oscillation and the triple deck favorable pressure gradient results in a pitching amplitude in the order of $O(R^{-9/16})$, which is also impractically small for engineering applications: $\simeq 0.02^\circ - 0.32^\circ$ for $R = 10^4 - 10^6$. Indeed, their work is for very high-frequency, very small-amplitude oscillations. Note that over this range, in contrast to the engineering-relevant problem considered in this work, the triple deck problem becomes mathematically interesting as the time-derivative term appears in the lower deck equations.

Brown & Cheng (1981) extended the work of Brown & Daniels (1975) to a more practical range of parameters $0 < k \ll R^{1/4}$. They provided a solution for the case of a flat plate pitching about its mid-chord at $k = 1/2$. In this section, we extend their work to an arbitrarily deforming thin airfoil, arbitrary k in the range $0 < k \ll R^{1/4}$, and correct for few minor mistakes in their derivation. More importantly, we use the developed theory, within a describing function formulation (Krylov & Bogoliubov, 1943) assuming weakly-nonlinear dynamics, to provide a viscous extension of the classical Theodorsen's lift frequency response, which was not provided by Brown & Cheng (1981).

A key element in the theoretical development below is the vanishing of the time derivative term from the triple deck equations over the range $0 < k \ll R^{1/4}$. That is, the lower

deck equations are quite similar to those of the steady case at a non-zero α_s studied by Brown & Stewartson (1970) with a proper definition for the equivalent steady angle of attack. However, we emphasize that this approach is not a quasi-steady solution; although the time-derivative term does not show up in the lower deck equations, the correspondence with the steady equations implies an equivalent angle of attack that is dependent on the oscillation frequency, as shown below. Therefore, the lower deck system is dynamical (i.e., possesses a non-trivial frequency response). In fact, even with no time-derivative term in the lower deck equations, it is not obvious how the steady results of Brown & Stewartson (1970) can be readily applied because the upstream flow is unsteady with Stokes layer in the perturbed Blasius layer. Brown & Daniels (1975) encountered a similar problem: how to match the solution of the perturbed Blasius boundary layer (with its inner Stokes layer) with the main deck of the triple deck structure? They resolved this issue by introducing a transition region, whose length is $O(k^{-1})$, between the perturbed Blasius boundary layer and the triple deck, called the *fore deck*. It has similar structure to that upstream of the triple deck: outer potential flow, main boundary layer, and an inner Stokes layer, as shown in figure 2.6. Therefore, in the low-frequency problem where the triple deck equations are void of the time-derivative term, to match the unsteady flow upstream of the triple deck with the "quasi-steady" flow in the triple deck, Brown & Cheng (1981) inserted a second fore deck between the first fore deck and the triple deck, as shown in figure 2.6. As such, the numerical results of Chow & Melnik (1976) to the steady problem of Brown & Stewartson (1970) could be readily used with an equivalent angle of attack. Since the equivalent steady angle of attack α_s is proportional to $A_\alpha k^2$ (where A_α is the amplitude of oscillation), and the steady triple deck formulation of Brown & Stewartson (1970) is valid for $\alpha_s = O(R^{-1/16})$, the current unsteady formulation is valid for $A_\alpha k^2 = O(R^{-1/16})$, which is quite relevant to engineering applications (e.g., $R \simeq 10^6$, $A_\alpha \simeq 5^\circ$, and $k < 5$).

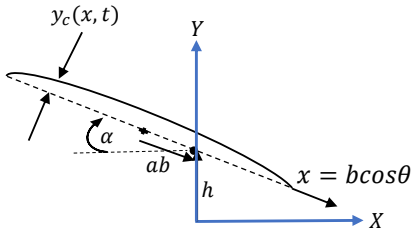

Figure 2.7: A flexible/deformable thin airfoil defined by the time-varying camber function $y_c(x,t)$.

2.3.2 Theoretical Development

Potential Flow Setup

Consider an arbitrarily deforming thin airfoil (i.e., of time-varying camber) in the presence of a uniform stream U, as shown in figure 2.7. In classical thin airfoil theory (e.g., Schlichting & Truckenbrodt, 1979; Bisplinghoff *et al.*, 1996; Robinson & Laurmann, 1956), it is convenient to define the acceleration potential $\Omega = \frac{D\Phi}{Dt}$, where $\frac{D}{Dt} = \frac{\partial}{\partial t} + U\frac{\partial}{\partial x}$ is the linearized material derivative and Φ is the velocity potential. Comparing with the linearized unsteady Bernoulli's equation, one can immediately relate the pressure P to the acceleration potential as $P = \rho\Omega$ and can show that Ω satisfies the Laplace equation ($\nabla^2\Omega = 0$). Then, using series expansion, it can be shown that the following series solution is obtained for the acceleration potential or pressure distribution over the upper surface, which automatically satisfies the Kutta condition (zero loading at the trailing edge)

$$P(\theta,t) - P_\infty = \rho\left[\frac{1}{2}a_0(t)\tan\frac{\theta}{2} + \sum_{n=1}^{\infty} a_n(t)\sin n\theta\right], \tag{2.3}$$

where θ is related to x via $x = b\cos\theta$ and a_0 represents the leading-edge singularity. The pressure on the lower side is given by the negative of (2.3). This series solution satisfies the unsteady Bernoulli's equation and basically bypasses the procedure of finding the velocity

field by dealing directly with the pressure distribution on the airfoil. Thus, if velocity distribution is needed, one can plug in the pressure distribution given by equations (2.3) into the unsteady Bernoulli's equation to find the velocity. Moreover, if the plate's normal velocity v_p, (refer to equation (2.15) that provides the relation for the harmonically pitching-plunging plate in a free stream at an angle of attack), is written as

$$v_p(\theta, t) = \frac{1}{2} b_0(t) + \sum_{n=1}^{\infty} b_n(t) \cos n\theta, \tag{2.4}$$

then the no-penetration boundary condition will provide a means to determine all the coefficients a_n's (except a_0) in terms of the plate motion kinematics (b_n's) as (Robinson & Laurmann, 1956, pp. 491)

$$a_n(t) = \frac{b}{2n} \dot{b}_{n-1}(t) + U b_n(t) - \frac{b}{2n} \dot{b}_{n+1}(t), \quad \forall\, n \geq 1. \tag{2.5}$$

The determination of a_0 is more involved in the sense that it requires solving an integral equation, which cannot be solved analytically for arbitrarily time-varying wing motion. It has been solved for some common inputs; e.g., step change in the angle of attack resulting in the Wagner's response (Wagner, 1925), simple harmonic motion resulting in Theodorsen's frequency response (Theodorsen, 1935), and sharp-edged gust (Küssner, 1929). Since the focus of this work is to provide a viscous extension of Theodorsen's frequency response, consider the simple harmonic motion

$$v_p(\theta, t) = V_p(\theta) e^{i\omega t}; \quad V_p(\theta) = \frac{1}{2} B_0 + \sum_{n=1}^{\infty} B_n \cos n\theta,$$

where the spatially-varying amplitude $V_p(\theta)$ may be complex and ω is the oscillation frequency. Then, a_0 is written as (Robinson & Laurmann, 1956, pp. 496) [1]

$$a_0(t) = U(B_0 + B_1)C(k)e^{i\omega t} - Ub_1(t), \tag{2.6}$$

where $C(k)$ is the Theodorsen's frequency response function, which depends on the reduced frequency $k = \frac{\omega b}{U}$ via

$$C(k) = \frac{H_1^{(2)}(k)}{H_1^{(2)}(k) + iH_0^{(2)}(k)}, \tag{2.7}$$

where $H_n^{(m)}$ is the Hankel function of m^{th} kind of order n. Finally, the potential flow coefficients of lift and pitching moment (positive pitching up) at the mid-chord point are written as

$$C_{L_P} = -\frac{\pi}{U^2}(a_0 + a_1) \quad \text{and} \quad C_{M_{0_P}} = \frac{\pi}{4}(a_2 - a_0). \tag{2.8}$$

Viscous Correction

Following the approach of Brown & Stewartson (1970) in the steady problem (described above), we relax the Kutta condition in the unsteady inviscid pressure distribution (2.3) by introducing a correction Γ_{v} to the Kutta circulation. This additional circulation will naturally introduce a singularity at the trailing edge. Similar to the steady case, there is no means within potential flow to determine the strength of such a singularity (additional circulation); the essence behind the Kutta condition is to remove such a singularity (*condition of least singularity* Crighton, 1985). This additional circulation will have two effects on the unsteady inviscid pressure distribution (2.3): (i) a steady-like effect with two singularities

[1] Note that the presentation of Robinson and Laurmann is adapted to a more common and modern notation.

at the leading and trailing edges, similar to the B_s-term in (2.1); and (ii) an unsteady effect from the interaction with the wake. The latter has a singularity only at the leading edge. As such, the modified pressure distribution can be written as

$$P(\theta,t)-P_\infty=\rho\left[\frac{1}{2}a_0(t)\tan\frac{\theta}{2}+\sum_{n=1}^{\infty}a_n(t)\sin n\theta+\frac{1}{2}B_{\mathrm{v}}(t)\left(\cot\frac{\theta}{2}+a_{0_{\mathrm{v}}}(t)\tan\frac{\theta}{2}\right)\right], \quad (2.9)$$

where the correction B_{v} is related to the additional circulation as $B_{\mathrm{v}}=\frac{U\Gamma_{\mathrm{v}}}{2\pi b}$ and $a_{0_{\mathrm{v}}}$ is the total leading edge singularity effect from the two contributions of Γ_{v}, mentioned above. This term has a non-trivial dynamics (there is a non-trivial transfer function from Γ_{v} to $a_{0_{\mathrm{v}}}$). It can be determined from potential flow considerations: it is the a_0 term in the unsteady inviscid pressure distribution (2.3) over the plate due to a bound circulation Γ_{v}, ignoring the quasi-steady contribution (i.e., the wake effects only). Therefore, similar to the general a_0 term, it cannot be determined analytically for arbitrary kinematics; there is an analytical expression in the special case of harmonic motion ($a_{0_{\mathrm{v}}}=2C(k)-1$ Brown & Cheng, 1981).

To determine the viscous correction B_{v}, without resorting to the Kutta condition ($B_{\mathrm{v}}=0$), we use the unsteady triple deck theory. Since $x=\cos\theta$, then $\cos\frac{\theta}{2}=\sqrt{\frac{1+x}{2}}$ and $\sin\frac{\theta}{2}=\sqrt{\frac{1-x}{2}}$, and $\tan\frac{\theta}{2}$ and $\cot\frac{\theta}{2}$ can be calculated accordingly. Approaching the trailing edge ($\theta\to 0$ or $\tilde{x}\to 1$), the inviscid pressure (with the B_{v} term) is written as

$$P(\tilde{x}\to 1,t)-P_\infty=\rho\left[\left(\frac{1}{2}a_0(t)+2\sum_{n=1}^{\infty}na_n(t)+\frac{B_v/2}{2\sqrt{2}}\sqrt{\frac{1-\tilde{x}}{2}}+\frac{1}{2}B_{\mathrm{v}}(t)a_{0_{\mathrm{v}}}(t)\right)\sqrt{\frac{1-\tilde{x}}{2}}+\frac{B_{\mathrm{v}}(t)/2}{\sqrt{\frac{1-\tilde{x}}{2}}}\right]. \quad (2.10)$$

Equation (2.10) reduces to (2.2) in the work of Brown & Stewartson (1970) for the steady case ($k=0$). In this case, $a_n=0\ \forall\ n\geq 1$; $a_0=-2U^2\alpha_s$; and $a_{0_{\mathrm{v}}}=0$, which yields equation (2.1) in this work. It also reduces to (2.7) in the work of Brown & Daniels (1975) for their case of a harmonically pitching flat plate about its mid-chord point at very high

frequency ($k \gg 1$). In this case, a_0 and a_1 (proportional to $\dot{\alpha}$) are neglected with respect to $a_2 = -b^2\ddot{\alpha}/4$, and $a_n = 0 \; \forall \; n > 2$.

The unsteady inviscid pressure (2.10) has the same form as the steady one (2.1) with

$$\alpha_s(t) \equiv \frac{1}{U^2}\left|\frac{1}{2}a_0(t) + 2\sum_{n=1}^{\infty} n a_n(t) + \frac{1}{2}B_{\mathrm{v}}(t)a_{0_{\mathrm{v}}}(t)\right|, \tag{2.11}$$

$$B_{\mathrm{v}}(t) \equiv B_s = -2\epsilon^3\lambda^{-5/4}\left(\frac{1}{2}a_0(t) + 2\sum_{n=1}^{\infty} n a_n(t) + \frac{1}{2}B_{\mathrm{v}}(t)a_{0_{\mathrm{v}}}(t)\right) B_e(\alpha_e). \tag{2.12}$$

Note that after matching with the steady pressure at the trailing-edge, the second term in the right hand side of equation (2.1) cancels the third term on the right hand side of the equation (2.10) as $B_s = B_v$. Therefore, this term does not contribute in the developed theoretical model. This comparison, along with the fact that the time-derivative term does not enter the triple deck equations, points to the possibility of directly using the steady solution by Chow & Melnik (1976) of the inner deck equations for the unsteady case with the equivalence shown above, valid in the range $0 < k \ll O(R^{1/4})$. In the above equivalence, if the term $\frac{1}{2}a_0 + 2\sum_{n=1}^{\infty} n a_n + \frac{1}{2}B_{\mathrm{v}}a_{0_{\mathrm{v}}}$ is negative, then the top of the oscillating thin airfoil will correspond to the top of the steady plate; and if is positive, then the top of the oscillating thin airfoil should correspond to the bottom of the steady plate. In either case, the equivalent steady angle of attack α_s would be positive. In fact, this correspondence has lead to the following interesting behavior: While there is always a significant lift decrease at the trailing edge stall angle in the steady case as shown in figure 2.5, there can be either increase or decrease in the unsteady lift when α_s reaches the trailing edge stall value, as shown by Brown & Cheng (1981). The above equivalence was mistakenly performed in (Brown & Cheng, 1981, see equations (2.2,2.9,2.12) in their work).

The application procedure will be as follows. The airfoil kinematics will be used to determine

the instantaneous values of $a_n(t)$ via the no-penetration boundary condition (2.5,2.6). These coefficients will define the equivalent steady angle of attack α_s according to (2.11), which defines α_e according to (2.2), resulting in B_e via the numerical solution of Chow & Melnik (1976). Finally, the $B_{\rm v}$ will be determined from B_e and the a_n's according to (2.12), which represents the viscous correction to the Kutta condition and consequently to the lift and moment as

$$C_L = -\frac{\pi}{U^2}\left[a_0 + a_1 + B_{\rm v}\left(1 + a_{0_{\rm v}}\right)\right] \quad \text{and} \quad C_{M_0} = \frac{\pi}{4U^2}\left[a_2 - a_0 + B_{\rm v}\left(1 - a_{0_{\rm v}}\right)\right]. \tag{2.13}$$

This procedure is iterative at each time step because the input (α_s) depends on the output ($B_{\rm v}$): to determine α_s, one needs $B_{\rm v}$, which would not be determined until α_s is known. However, our computational results show that the $B_{\rm v}$-contribution to α_s is quite negligible. As such, it is fair to consider the following equivalence instead of (2.11,2.12)

$$\alpha_s(t) \equiv \frac{1}{U^2}\left|\frac{1}{2}a_0(t) + 2\sum_{n=1}^{\infty} n a_n(t)\right|, \quad B_{\rm v}(t) \equiv -2\epsilon^3\lambda^{-5/4}\left(\frac{1}{2}a_0(t) + 2\sum_{n=1}^{\infty} n a_n(t)\right) B_e(\alpha_e), \tag{2.14}$$

which eliminates the need for iteration at each time step.

It should be noted that this procedure admits arbitrary time variation of the airfoil camber (not necessarily harmonic); only a_0 should be modified accordingly instead of using (2.6). Nevertheless, because there might not be exact closed-form expressions for $a_0(t)$ due to other kinematics (e.g., step input), we recommend using (2.6) to construct a viscous frequency response (describing function Krylov & Bogoliubov, 1943), assuming a weakly nonlinear system, and then using the Fourier transform to obtain the viscous lift force and pitching moment due to an arbitrarily time-varying camber (as shown in Garrick, 1938; Bisplinghoff *et al.*, 1996, pp. 282-283). This procedure is demonstrated in more detail in the next section. For more examples on describing function analysis, please refer to Slotine *et al.* (1991).

2.4 Viscous Lift Frequency Response

2.4.1 Setup of the Frequency Response (Describing Function)

The above approach can be used to construct a viscous extension of Theodorsen's function at a given Reynolds number. For practical use, we opt to show such an extension for a pitching-plunging flat plate. The problem setup, governing equation and boundary condition are shown in figure 1.2 when pitching and plunging motions are harmonic. In this case, the normal velocity of the plate (assuming small disturbances $\dot{h}$ and α) is written as

$$v_p(x,t) = \dot{h}(t) - \dot{\alpha}(t)(x - ab) - U\alpha, \quad -b \leq x \leq b, \tag{2.15}$$

where h is the plunging displacement (positive upward) and α is the pitching angle (angle of attack, positive clockwise), and ab represents the chordwise distance from the mid-chord point to the hinge point, as shown in figure 2.7. This kinematics results in

$$b_0(t) = 2\left[\dot{h}(t) + ab\dot{\alpha}(t) - U\alpha\right] = 2v_{1/2}(t), \quad b_1(t) = -b\dot{\alpha}(t) \text{ and } b_n = 0 \; \forall n > 1,$$

where $v_{1/2}$ is the normal velocity of the mid-chord point. As such, for the harmonic motion

$$h(t) = Hbe^{i\omega t} \text{ and } \alpha(t) = A_\alpha e^{i\omega t}, \tag{2.16}$$

equations (2.5,2.6) result in the following coefficients

$$a_0(t) = U\left[2V_{3/4}C(k)e^{i\omega t} + b\dot{\alpha}(t)\right], \quad a_1(t) = b\dot{v}_{1/2} - bU\dot{\alpha}(t), \quad a_2(t) = -\frac{b^2\ddot{\alpha}(t)}{4}, \tag{2.17}$$

where $v_{3/4}(t) = V_{3/4}e^{i\omega t}$ is the normal velocity at the three-quarter-chord point. Also, the coefficient a_{0_v} is given by (Brown & Cheng, 1981)

$$a_{0_v} = 2C(k) - 1.$$

Note that in this harmonic formulation, equation (2.17) may yield complex values for the coefficients a_n's; the actual coefficients, to be used in the series (2.9), are determined by taking the real parts of those in (2.17). In the common classification proposed by Theodorsen (1935), the coefficient a_0 represents the circulatory contribution while the other two coefficients (a_1, a_2) represent the non-circulatory contribution. The lift coefficient is then written as

$$C_L(t) = \underbrace{\underbrace{-\pi\frac{b\dot{v}_{1/2}(t)}{U^2}}_{\text{Non-circulatory}} + \underbrace{2\pi\alpha_{3/4}(t)C(k)}_{\text{Circulatory}}}_{\text{Potential Flow Solution}} - \underbrace{2\pi\tilde{B}_v(t)C(k)}_{\text{Viscous Correction}}, \tag{2.18}$$

where $\tilde{B}_v = \frac{B_v}{U^2}$, $\alpha_{3/4}$ is the local angle of attack at the three-quarter-chord point (as recommended by Pistolesi theorem Schlichting & Truckenbrodt, 1979, pp. 80), and the multiplication $\alpha_{3/4}(t)C(k)$ is interpreted after writing $\alpha_{3/4}(t) = \overline{\alpha_{3/4}}e^{i\omega t}$ as

$$\left(\alpha_{3/4}C(k)\right)(t) = \Re\left(\overline{\alpha_{3/4}}C(k)e^{i\omega t}\right),$$

where $\overline{\alpha_{3/4}}$ may be a complex number and $\Re(.)$ denotes the real part of its complex argument.

Recall that if $u(t) = Ae^{i\omega t}$ is the input to a linear dynamical system whose frequency response is $G(i\omega)$, then the steady state output is simply written as $y(t) = A|G(i\omega)|e^{i\omega t + \arg G(i\omega)}$ (Ogata & Yang, 1970). The describing function technique represents an extension of the frequency response concept for weakly nonlinear systems
(Krylov & Bogoliubov, 1943). In this technique, only the response at the fundamental frequency is considered and the higher harmonics are neglected. As such, the response of a

weakly nonlinear system to the input $u(t) = Ae^{i\omega t}$ is approximated as $y(t) = Y(A,\omega)e^{i\omega t+\phi(A,\omega)}$. That is, unlike linear systems, the magnitude and phase of the transfer function depend on the input amplitude. Using such a technique, we provide below a viscous extension of Theodorsen's frequency response; i.e., the frequency response between the quasi-steady lift (input) and the viscous circulatory lift (output).

The system possesses two nonlinearities as shown in figure 2.9: a multiplicative nonlinearity and the triple deck viscous nonlinearity. The former is due to interactions between the airfoil motion (represented by a_n's) and the trailing edge singular behavior (represented by B_s) while the latter is due to the steady triple deck nonlinear characteristics, determined numerically by Chow & Melnik (1976), and shown here in figure 2.3(b). The effect of these nonlinearities is minimal with respect to the main linear contribution at small angles of attack as evident from the power spectra (FFT) of the total circulatory lift coefficient C_{L_C} shown in figure 2.8(a) for the case of pitching around the mid-chord point with $A_\alpha = 1^\circ$ at $k = 0.8$ and $R = 10^5$. The FFT of C_{L_C} has a single distinct peak at the operating frequency ($k = 0.8$). In fact, even the viscous contribution (the B_v-term) is mostly linear despite the existence of a weak cubic nonlinearity as evident from its FFT shown in figure 2.8(b). This weakly nonlinear behavior of the system justifies the use of the describing function approach (akin to linearization) to construct a frequency response. It is interesting to note that the triple deck theory confirms the common expectation that the most significant term in the power series expansion of lift in terms of the angle of attack after the linear term is the cubic one (Ding & Wang, 2006; Librescu *et al.*, 2003). It is also interesting to point out that even at this small amplitude ($A_\alpha = 1^\circ$) and relatively large Reynolds number ($R = 10^5$), the viscous contribution is about 19%, as shown in figure 2.8(a).

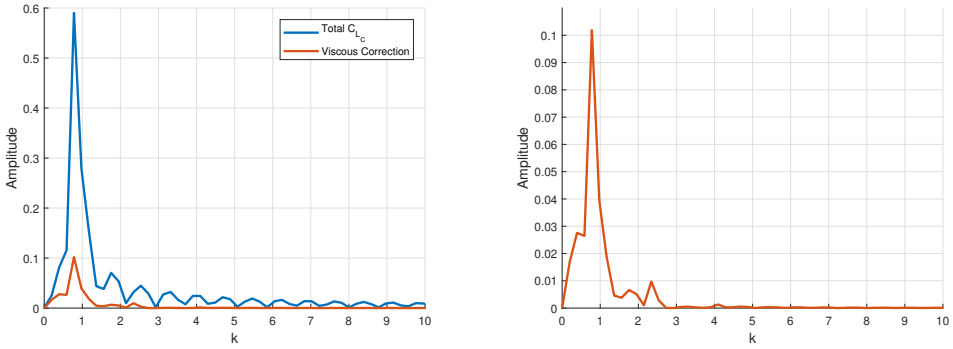

(a) Total C_{L_C} normalized by $2\pi A_\alpha$. (b) Viscous contribution.

Figure 2.8: Power spectra (FFT) of the total circulatory lift coefficient C_{L_C} and the viscous correction $\pi\tilde{B}_v$, both normalized by $2\pi A_\alpha$, for the case of a flat plate pitching around the mid-chord point with $A_\alpha = 1^\circ$ at $k = 0.8$ and $R = 10^5$. The behavior is almost linear with single distinct peak at this small amplitude.

2.4.2 Computation Procedure

As described in chapter 1, the ultimate goal in unsteady aerodynamics is to determine the aerodynamics loads on a moving airfoil. Following the problem setup by Theodorsen shown in figure 1.2 and the circulatory non-circulatory classification by him, we show how the new viscous correction is accommodated. Let k and R be given. Then, the quasi-steady lift coefficient (input to the sought lift dynamical system) is written as

$$C_{L_{QS}}(t) = 2\pi\alpha_{3/4}(t).$$

Also, the coefficients a_0, a_1, and a_2 are given from (2.17). Thus, α_s can be obtained accordingly from (2.14), however, care should be taken when applying (2.14). It should be applied instantaneously as

$$\alpha_s(t) = \frac{1}{U^2}\left|\frac{1}{2}a_0(t) + 2a_1(t) + 4a_2(t)\right|.$$

As such, the scaled angle of attack $\alpha_e(t)$ for the numerical solution of Chow & Melnik (1976) is obtained from (2.2) with $\epsilon = R^{-1/8}$. Using, figure 2.3(b), one can obtain $B_e(t)$, which in

turn is substituted in (2.2) to determine the strength B_s of the equivalent steady trailing edge singularity. Then, (2.14) will yield the viscous correction $B_{\mathrm{v}}(t)$. As such, the unsteady viscous circulatory lift coefficient is determined from (2.18) by excluding the first term, i.e.,

$$C_{L_C}(t) = \Re\left[2\pi\alpha_{3/4}(t)C(k) - \pi\tilde{B}_{\mathrm{v}}(t)\right]. \tag{2.19}$$

Finally, a spectral analysis (e.g., FFT) is applied to $C_{L_C}(t)$ to extract its relative amplitude and phase shift with respect to $C_{L_{QS}}(t)$. That is, the circulatory-lift viscous transfer function C_{v} is defined as

$$C_{\mathrm{v}}(k; Re) \triangleq \frac{C_{L_C}(k; Re)}{C_{L_{QS}}(k)}.$$

Figure 2.9 shows a block diagram for the dynamics of the unsteady viscous circulatory lift.

Note that if $\alpha_e(t)$ exceeds 0.47, then the simulation should be terminated because such a value implies trailing edge stall beyond which the current analysis is not valid. This limitation defines the region of applicability of the developed model. For example, the model can handle an oscillation about the mid-chord point with 3° amplitude at 0.4 reduced frequency and $10,000$ Reynolds number. However, it cannot handle the same situation when the amplitude is increased to 4° as $\alpha_e(t)$ would exceed 0.47 during the course of the simulation.

Following the above procedure, we construct frequency responses of the unsteady, viscous, circulatory lift coefficient C_{L_C} at different Reynolds numbers, which are shown in figure 2.10 in comparison to Theodorsen's. Intuitively, as R increases, the viscous response approaches the inviscid Theodorsen's response and vice versa. The current theory does not predict a considerable change in the magnitude from the inviscid Theodorsen's solution. However, it is found that viscosity induces a significant phase lag beyond Theodorsen's; the larger the oscillation frequency and the smaller the Reynolds number are, the larger the discrepancy is between Theodorsen's phase lag and the viscous results. Interestingly, this finding supports

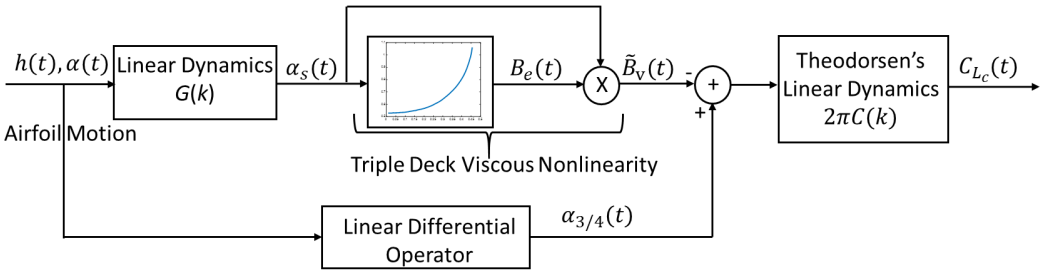

Figure 2.9: A block diagram showing the different components constituting the dynamics of the viscous circulatory lift. The airfoil motion dictates the angle of attack $\alpha_{3/4}$ at the three-quarter-chord point, which is the main input to Theodorsen's inviscid linear dynamics, resulting in the potential flow circulatory lift. The upper branch represents the viscous correction developed in this work. The correction term $\tilde{B}_v$ represents a singularity in the inviscid pressure distribution at the trailing edge. It should be set to zero according the Kutta condition. Rather, it is obtained here from the triple deck boundary layer theory. The airfoil motion goes into some linear dynamics (that includes Theodorsen function) to obtain an equivalent steady angle of attack, which will be used in the nonlinear triple deck theory to obtain the viscous correction to the circulatory lift.

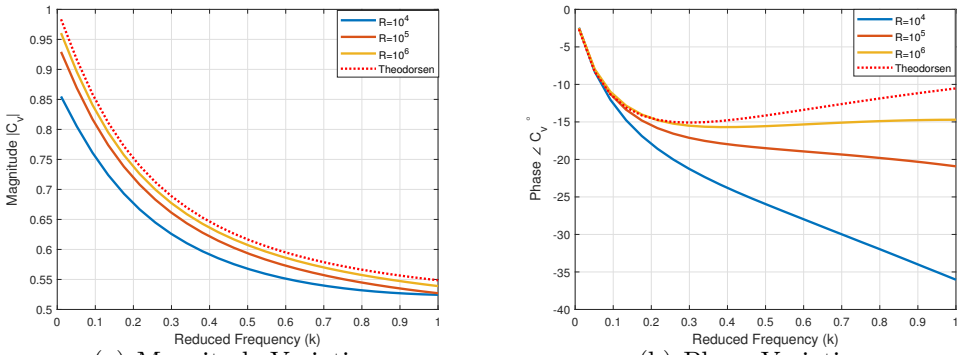

(a) Magnitude Variation.

(b) Phase Variation.

Figure 2.10: Comparison between the frequency responses of the unsteady, viscous, circulatory lift coefficient C_{L_C} at different Reynolds numbers and that of the potential flow circulatory lift coefficient (i.e., Theodorsen's). The larger the frequency and the lower the Reynolds number, the larger the discrepancy in phase between Theodorsen function and the viscous frequency response.

the conclusions of some of the earlier experimental efforts (Chu & Abramson, 1959; Bass *et al.*, 1982): Chu & Abramson (1959) suggested adding a phase lag of -10° to Theodorsen function for a better estimate of the unsteady lift and flutter boundary when $k \simeq 0.5$. Bass *et al.* (1982) conducted a water tunnel experiment for a NACA 16-012 undergoing pitching oscillations around its quarter-chord point in the range of $0.5 < k < 10$ and $R = 6,500 - 26,500$. They compared their force measurements to Theodorsen's potential flow frequency response. They found bad agreement in the range $0.5 < k < 2$ where the most pronounced boundary layer activity is observed and the flow near trailing edge being separated and alternating around the trailing edge. They concluded that adding a phase lag of -30° to the Theodorsen's $C(k)$ would make the predicted lift from the classical theory of unsteady aerodynamics match their experimental measurements over this range, which supports the current results shown in figure 2.10.

This finding is particularly important for the determination of the flutter boundary (e.g., Alben, 2008; Mandre & Mahadevan, 2010; Zakaria *et al.*, 2015; Hussein & Canfield, 2017). Note that the flutter instability, similar to any typical Hopf bifurcation, is mainly dictated by when energy is added/subtracted during the cycle. That is, the phase difference between the applied loads (aerodynamic loads) and the system motion (e.g., angle of attack) plays a crucial role in dictating the stability boundary (Bisplinghoff *et al.*, 1996, pp. 280). Therefore, if the Theodorsen function does not capture such a phase difference correctly, it will typically lead to an erroneous flutter stability boundary. Hence, if the current model better captures the phase lag, it may enhance our flutter predictability, if occurring at high reduced frequencies. Based on this discussion, we suggest using the obtained viscous frequency responses in place of Theodorsen's for a more accurate, yet efficient, estimate of the flutter boundary. This point will be discussed further below from an added mass point of view in the last section.

2.5 Validation via Computational Simulation

In this section, we investigate the effect of viscosity on the lift frequency response using a higher fidelity simulation of the Navier Stokes equations to support/refute the theoretical findings in the last section. Although the developed theory should be valid only for the laminar regime, it is interesting to assess its performance in high Reynolds number turbulent flows as well to investigate its ability to capture the global picture of the flow field and some important integrated quantities such as the generated aerodynamic loads. For this purpose, two computational setups have been constructed using the finite volume based software package ANSYS FLUENT: (1) unsteady laminar simulation and (2) Unsteady Reynolds-averaged-Navier-Stokes (URANS). For the latter setup, it is important to select an appropriate turbulence model that accurately captures the behavior of the integrated global quantities of interest (e.g., the lift dynamics). Note that details of the small-scale features in the flow will not be captured by averaging; large eddy or direct numerical simulations will be needed instead. However, this is beyond the scope of this work. The $k-\omega$ turbulence model is well-known for its superiority in handling complex boundary layer flows with adverse pressure gradients (Wilcox, 1998; Menter, 1994). However, it may result in early transition and separation and is sensitive to inlet boundary conditions. Nevertheless, no severe adverse pressure gradient and separation are expected in the current investigations with small amplitudes. We also assume a fully turbulent flow in the high Reynolds number simulation cases (i.e., no transition). Therefore, the $k-\omega$ model should be quite suitable for the current application, with the caveat of being sensitive to free stream inlet conditions. This issue is resolved by selecting its extension: the shear-stress-transport (SST) $k-\omega$, which makes use of the $k-\omega$ model near the wall and the $k-\epsilon$ model in the free stream and wake regions. As such, the $k-\omega$ SST exploits the $k-\omega$ capabilities in capturing the boundary layer and its adverse pressure gradient while mitigating its sensitivity to inlet conditions (such as the free stream turbulence intensity). Hence, it is an almost perfect choice for the current study

when performing simulations at high Reynolds numbers, assuming a fully turbulent flow.

In relation to the numerical setup, the pressure velocity coupling was tackled by the SIMPLE algorithm. All the spatial discretization were second order upwind. Implicit second order discretization was chosen for transient terms. The convergence criterion for all the variables were set to be 10^{-6} at each time step. To select an appropriate value for the time step, three numerical simulations were performed using 500, 250, and 150 time steps per pitching cycle (n_t). For instance, if the period of pitching motion is T, the simulation time steps will be T/n_t. It was found that 250 sample per cycle is sufficient to obtain well-converged results. In each simulation, the number of cycles are chosen to be sufficient for a periodic lift pattern to establish.

2.5.1 Computational Setup

The O-Type far field located $25c$ away from the solid body has been implemented for grid generation around the standard NACA 0012 airfoil with sharp trailing edge. In return of closing the blunt trailing edge of the original NACA 0012, the thickness of the airfoil altered to 11.9%. To construct the dynamic mesh due to the airfoil motion, the computational domain is divided into three rings as shown in figure 2.11. The inner ring (red), which encloses the airfoil, has the radius of $6c$. In this region, hybrid mesh is used such that a boundary layer structure dense mesh near the airfoil guarantees dimensionless distance $y^+ \equiv \frac{\rho u_\tau y}{\mu} < 1$ (where $u_\tau = \sqrt{\frac{\tau_w}{\rho}}$ is the friction velocity, $\tau_w = \frac{dU}{dy}|_{y=y_w}$ is the wall shear stress, and y is the distance from the nearest wall) for all the case studies, in conjunction with an unstructured tri-mesh attached to it. The distance of the first layer of the mesh was set to be $10^{-5}c$ with 1.1 growth factor, which guarantees that the triple deck structure, $O(R^{-3/4})$, is well resolved at the highest Reynolds number (10^6) in this simulation. A total of 300 mesh points were used on each side of the airfoil. A size function has been used to

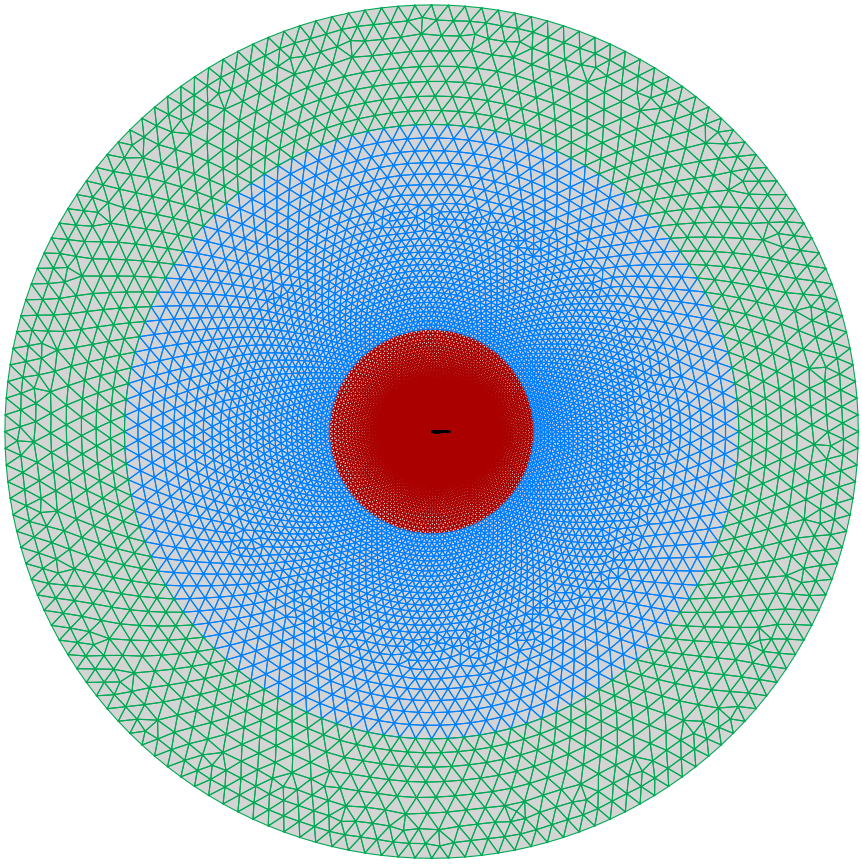

Figure 2.11: O-Type mesh around the airfoil with the outer ring being fixed, the inner ring moves rigidly with the airfoil, and the intermediate ring represents the deforming dynamic mesh.

ensure that the unstructured mesh in the inner ring is dense enough to capture the shed vortices if needed. The whole inner ring including the airfoil undergos a rigid body pitching motion. No dynamic mesh is used in this region to ensure that the grids near the airfoil maintain their fine configuration and quality as they were before the motion.

The outer ring located at $25c$ away from the airfoil is stationary as if no motion is taking place inside the domain. This fixed mesh near the outer boundaries certifies that the farfiled boundary conditions are applied correctly. The intermediate ring plays the main role of the dynamic mesh. The inner radius of this ring is $6c$ and the outer radius is $18c$; it occupies a large region inside the domain. It should be noted that these values ($6c$ and $18c$) are obtained based on a few tries and errors to minimize the mesh deformations in this region and to leave enough room for the outer and inner grids to be generated. Based on the airfoil geometry, prescribed deflections and required accuracy, these numbers might change, although did not seem to have a significant effect on the results based on the author's experience as long as reasonable values are chosen. Moreover, since the computational time is not a big concern in this project, it is tried to have very good grid resolution. Both remeshing and deforming techniques are utilized to damp the deformations in the region caused by the motion of the inner ring. A User Defined Function is attached to the solver to impose an arbitrary motion to the airfoil and prevent high skewness in the dynamic mesh zone. The advantage of this method may not be sensible when deflections are small, yet it demonstrates its ability in damping mesh deformations at large motion amplitude. The large size of the intermediate region gives enough room to handle excessive deflections. The total number of grids is roughly 2×10^5. For more information about the computational setup, the reader is referred to our earlier effort (Rezaei & Taha, 2017). Mesh independence study has been performed by running another case in which the grids were twice denser and no alternation in the results has been observed. Thus, the aforementioned mesh configuration was utilized in all of the forthcoming simulations.

Since the flow is assumed to be incompressible, velocity inlet and pressure outlet, corresponding to left semi-circle and right semi-circle respectively, were set as the far field boundary conditions. In all the simulations, the gauge pressure at the outlet boundary condition was set to zero. The no-slip boundary condition is imposed on the airfoil which is undergoing the harmonic pitching motion $\alpha = A_\alpha \sin \omega t$ with a pitching amplitude of $A_\alpha = 3$ degrees to ensure that the airfoil is in the pre-stall regime (Schlichting & Truckenbrodt, 1979). The chord length of the airfoil is $18cm$ and the magnitude of the velocity at the inlet boundary is 1 m/s and 10 m/s corresponding to $R = 10^4$ and $R = 10^5$, respectively. The laminar solver is used in the lower Reynolds number $R = 10^4$ and the unsteady Reynolds averaged Navier-stokes equations (URANS) are used in the case of the high $R = 10^5$. Although in the theoretical development in the previous sections the effect of turbulence is not considered, the URANS simulations are carried out as they calculate average quantities and to assess the applicability of the theory to find the global aerodynamic loads at higher Reynolds numbers where the flow is no longer laminar. For these cases, the turbulent intensity of the flow was set to 0.1%. Note that the free stream turbulence intensity is not expected to significantly affect the results because the $k - \omega$ SST turbulence model utilizes the $k - \epsilon$ model in the free stream region, which is robust to changes in the inlet conditions; our simulations with changing the inlet turbulence intensity ten folds did not show an appreciable change in the lift dynamics.

As mentioned above, $y^+ < 1$ is required for the grid resolution near the wall since the adopted turbulence model ($k - \omega$ SST) does not utilize wall function, but is valid all the way down to the near-wall region. To quantify that the lower deck ($\sim cR^{-5/8}$) provided in figure 2.2 is resolved, the length of the first layer of the grids near the wall h_w is compared against the lower deck length scale. Since $h_w = 10^{-5}c = 1.8 \times 10^{-6}m$ and $cR^{-5/8} = 1.35 * 10^{-4}$, the grid resolution is capable of resolving the triple-deck structure.

Figure 2.12 shows the distribution of the pressure difference (i.e., lift distribution) over the

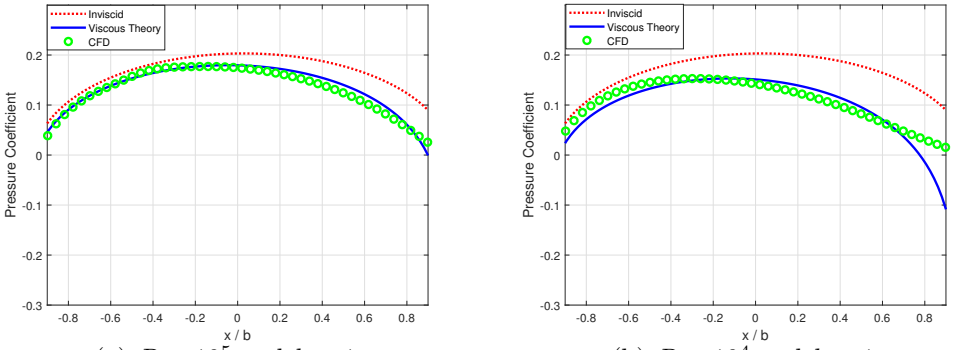

(a) $R = 10^5$ and $k = 1$. (b) $R = 10^4$ and $k = 1$.

Figure 2.12: Comparison for the pressure distribution over the flat plate from the inviscid theory, the current viscous theory, and computational simulations in the case of a harmonically pitching airfoil about its quarter-chord with 3° amplitude at $k = 1$ and (a) $R = 10^5$, (b) $R = 10^4$. In the former case, a URANS solver is used whereas a laminar solver is used in the latter case. The figures show the pressure distributions at the instant of zero pitching angle $\alpha(t) = 0$ and maximum upward pitching velocity $\dot{\alpha}$.

flat plate for the case of pitching about the quarter-chord with 3° amplitude at $k = 1$ for two Reynolds numbers $R = 10^5$, $R = 10^4$. The figure shows results from the inviscid theory (i.e., twice the result of (2.3)), which is insensitive with respect to R; the developed viscous theory (i.e., twice the result of (2.9)); and the computational simulations described above. Very good matching between the computational simulations and the developed theory is found. It should be noted that the selected instant ($\alpha(t) = 0$ and $\dot{\alpha}$ maximum) is a critical instant during the cycle where the flat plate is on the verge of trailing edge stall, as shown in figure 2.13: when $\alpha(t) = 0$ and $\dot{\alpha}$ is maximum, at this relatively high k, the equivalent α_e becomes very close to the trailing edge stall value 0.47. Both results from computational simulations and the current boundary layer theory indicate that, as R decreases, the pressure distribution at this critical moment deviates more from the inviscid one; the pressure distribution decreases and shifts to the left (i.e., the pressure attains its maximum earlier on the airfoil). The developed theory captures this behavior by adding a singularity at the trailing edge, which bends the pressure distribution curve downward and to the left. However, it is precisely this trailing edge singularity that causes discrepancy between the predicted singular pressure and the actual non-singular pressure at the trailing edge.

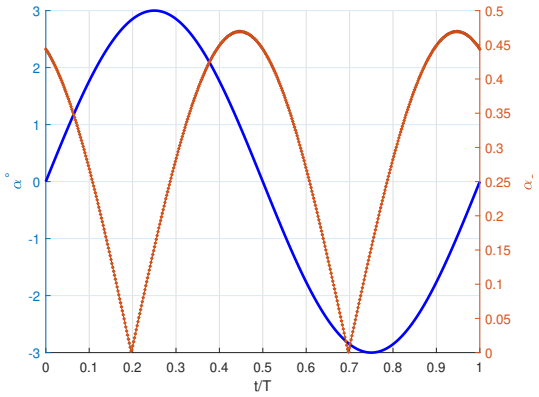

Figure 2.13: Variation of the equivalent angle of attack α_e over the cycle along with the actual angle of attack α for the case of a harmonically pitching flat plate about its quarter-chord with 3° amplitude at $k = 1$ and $R = 10^4$. At this relatively high k, the instant of maximum $\dot{\alpha}$ renders the airfoil on the verge of trailing edge stall in comparison to the instant of the maximum α.

Nevertheless, the strength of this singularity decreases as R increases and the discrepancy becomes more confined to the immediate vicinity of the trailing edge (i.e., agreement with the computational simulations over a wider range of the airfoil). We emphasize that the developed theory should be valid only for high Reynolds numbers. In other words, the results of the developed theory should be only interpreted as providing a first-order correction to the inviscid results for finite Reynolds numbers; from this point of view, it is quite satisfactory. One more point that is noteworthy, though it does not seem to be significant here, is that the developed theory is for an infinitely thin airfoil whereas the computational simulations are performed for a finite-thickness airfoil (NACA 0012) that can affect the potential flow pressure outside of the boundary layer due to curvature. This induces adverse pressure gradient downstream of the maximum thickness point; thus, the flow becomes more prone to separation.

2.5.2 Computation of the Viscous Lift Frequency Response Function

In this study, we show how the viscous lift frequency response (describing function) is determined from computational simulations at a given Reynolds number. Similar to Theodorsen (1935), this transfer function is defined as the ratio between the circulatory lift coefficient and the quasi-steady lift coefficient. As such, given a combination of k and R, our computational setup is simulated to result in a time history of the total lift coefficient $C_{L_{tot}}$. According to the describing function approach (Krylov & Bogoliubov, 1943), the Fourier transform $\hat{C}_{L_{tot}}$ of the total lift coefficient at the fundamental frequency k is considered; it is a complex number, as shown in figure 2.14. To extract the circulatory contribution $\hat{C}_{L_C}$ from $\hat{C}_{L_{tot}}$, the non-circulatory contribution must be subtracted. Adopting Theodorsen's estimate [1] for the non-circulatory loads in the case of a pitching airfoil around the quarter-chord point, we obtain

$$C_{L_{NC}} = \pi \frac{b}{U}\left(\dot{\alpha} + \frac{b\ddot{\alpha}}{2U}\right) \quad \Rightarrow \quad \hat{C}_{L_{NC}}(k) = \pi A_\alpha \left(ik - k^2/2\right).$$

As such, the circulatory lift frequency response is obtained as $\hat{C}_{L_C} = \hat{C}_{L_{tot}} - \hat{C}_{L_{NC}}$, as shown graphically in figure 2.14. Then, the complex number $\hat{C}_{L_C}$ is divided by the quasi-steady lift

$$C_{L_{QS}} = 2\pi\alpha_{3/4} = 2\pi\left(\alpha + \frac{\dot{\alpha}b}{U}\right) \quad \Rightarrow \quad \hat{C}_{L_{QS}} = 2\pi A_\alpha \left(1 + ik\right)$$

to obtain the viscous lift transfer function $C_{\mathrm{v}}(k;R) = \frac{\hat{C}_{L_C}(k;R)}{\hat{C}_{L_{QS}}(k)}$.

Figure 2.15 shows the computed viscous lift frequency response function at two different Reynolds numbers: $R = 10^5$ and $R = 10^4$; the former is obtained using URANS and the latter is obtained using the laminar solver. The figure also shows the inviscid Theodorsen's

[1] Theodorsen's estimate for the non-circulatory loads may not be accurate as will be discussed below.

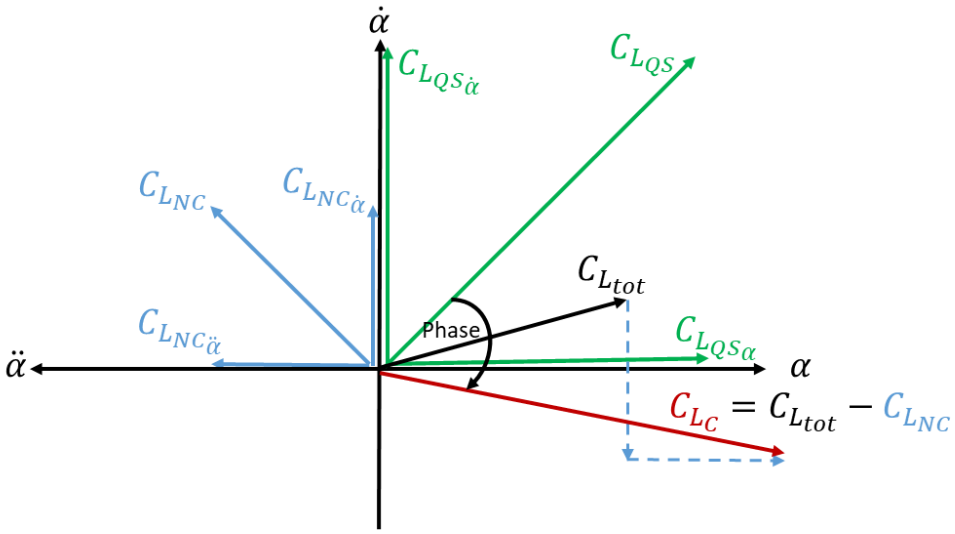

Figure 2.14: Complex plane showing the different lift components.

lift frequency response function and the developed viscous extension for comparison. For the case of $R = 10^4$, the convergence properties of the laminar solver at lower k values were not satisfactory and therefore omitted. It is found that the magnitude of the transfer function decreases as R decreases and k increase (conforming with the results of Zakaria *et al.*, 2017), which was not captured using the triple deck theory. However, the computational phase results corroborate the theoretical findings discussed above. That is, at lower Reynolds numbers and higher frequencies, there is a significant deviation from Theodorsen's phase prediction. In fact, there is a satisfactory quantitative agreement between the theoretical phase lag predictions and computational results. This additional phase lag may significantly affect the prediction of an instability boundary (e.g., flutter) as discussed above. Note that Bisplinghoff *et al.* (1996, pp. 280) emphasized the importance of unsteady phase lag in dictating flutter boundary even at low reduced frequencies (e.g., $k = 0.1$) where the phase lag is already very small. Therefore, since the developed theory provides a better estimate of the unsteady phase lag than Theodorsen function, particularly at large k and low R, it is expected to enhance our retarding capability in predicting flutter, which is discussed further below from an added mass point of view. It should be noted that most of the earlier experimental efforts that reported failure in predicting flutter (or unsteady loads) lie in the

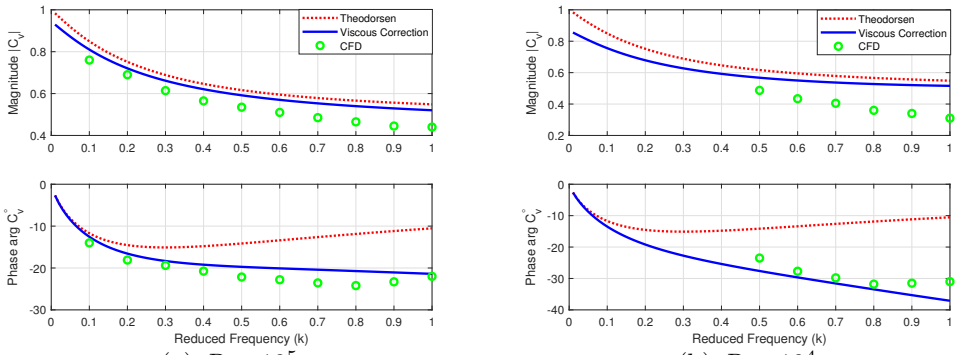

(a) $R = 10^5$. (b) $R = 10^4$.

Figure 2.15: Computational results of the frequency responses of the unsteady, viscous, circulatory lift coefficient C_{L_C} at different Reynolds numbers. The computational results support the theoretical finding that the larger the frequency and the lower the Reynolds number, the larger the discrepancy in phase between Theodorsen function and the viscous frequency response.

high-frequency range: $k \simeq 0.5$ (Chu & Abramson, 1959), $k \simeq 0.6 - 1.4$ (Henry, 1961), $k \simeq 0.7$ (Abramson & Ransleben, 1965), and $k \simeq 0.5 - 10.0$ (Bass *et al.*, 1982). Therefore, it is expected that the developed theory may help reconcile the concerns raised in these efforts; a quantitative assessment of the effect of the predicted additional phase lag on the flutter boundary will be addressed in future work. Having said that, one should emphasize that the flutter frequency of conventional airplane wings is usually in the order of $k = 0.1$ (Bisplinghoff *et al.*, 1996, pp. 280), for which the current theory results in a phase close to Theodorsen's. However, it is expected that the developed theory will be useful for the flutter prediction of the next generation unconventional designs with highly flexible wings (typically with higher flutter frequencies).

It is noteworthy to mention that a better matching between the theoretical phase lag predictions and computational results is obtained when using the eddy viscosity in the developed boundary layer theory, as shown in figure 2.16 for the case of $R = 10^6$. In this case, a Reynolds number based on the average value of the eddy viscosity (obtained from the URANS simulations) is used in the developed theoretical model. That is, even when operating at a high Reynolds number where the deviations between Theodorsen results and the

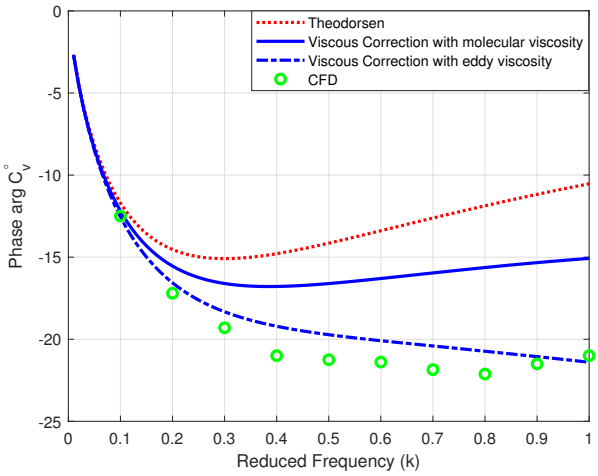

Figure 2.16: Phase of the lift frequency response at $R = 10^6$ when using molecular and eddy viscosity. Using eddy viscosity enhances the matching between the theoretical phase lag predictions and computational simulations. Turbulent viscosity ratio of 10 is used based on URANS simulations.

developed theory and computational simulations are minimal, the effective Reynolds number is actually less implying that the phase predictions of Theodorsen function are quite off at high frequencies. Note that as R decreases, the turbulent viscosity ratio decreases and its effect on the developed theory may be neglected.

2.6 Physical Illustrations: Viscosity Induced Lag and the Kutta Condition

2.6.1 Viscosity Induced Lag

The fact that viscosity induces phase lag in the flow response is well known from classical fluid problems. For example, the laminar viscous flow in a pipe due to an oscillatory pressure gradient shows phase lag between the input pressure gradient and the flow response (e.g., velocity distribution, wall shear or vorticity Langlois & Deville, 2014, pp. 113-116). Also,

recall the Stokes second problem: the flow above an oscillating infinite plate, shown in figure 2.17. This problem is one of the few simple problems where an analytical solution of the Navier Stokes equations is available (Batchelor, 2000, pp. 191-193; Lamb, 1932, pp. 619-623; Langlois & Deville, 2014, pp. 109-111), which results in the following velocity distribution

$$u(y,t) = Ue^{-y/\delta}\cos\left(\omega t - y/\delta\right), \tag{2.20}$$

where $\delta = \sqrt{2\nu/\omega}$ is the thickness of the boundary layer (Stokes layer) and ν is the fluid's kinematic viscosity. Equation (2.20) clearly shows the phase lag between the input (plate motion) to the flow dynamics and the flow response and that this phase lag increases with the fluid viscosity. Moreover, the vorticity in the boundary layer experiences even more lag in development with respect to the plate motion than the fluid velocity as shown in the vorticity response

$$\zeta(y,t) = -\frac{\partial u}{\partial y} = \frac{\sqrt{2}U}{\delta}e^{-y/\delta}\cos\left(\omega t - y/\delta - \pi/4\right). \tag{2.21}$$

The generation of vorticity in the boundary layer is particularly important for the explanation of the observed lag in the lift frequency response of an oscillating airfoil, for the lift evolution is intimately related to vorticity generation and circulation development.

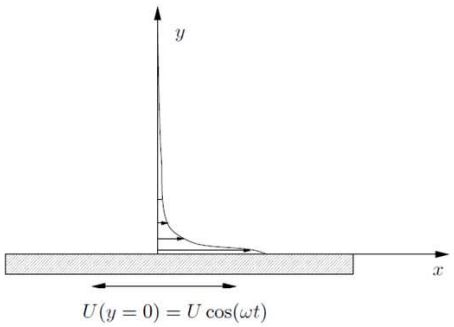

Figure 2.17: Stokes Second Problem: Flow above an oscillating infinite plate.

2.6.2 Viscous Damping and Lag in Circulation Development

To show that the observed phase lag in the lift frequency response is due to lag in the development of the bound circulation, we computed the latter by performing a line integral of the tangential velocity along a closed contour around the airfoil. Then, we followed a similar procedure to the one presented in the last section to construct a frequency response (describing function) between the quasi-steady circulation Γ_{QS} as an input and the viscous unsteady bound circulation Γ as an output. The former is determined as

$$\Gamma_{QS} = UbC_{L_{QS}} = 2\pi bU\left(\alpha + \frac{\dot{\alpha}b}{U}\right) \quad \Rightarrow \quad \hat{\Gamma}_{QS} = 2\pi UbA_{\alpha}\left(1 + ik\right). \tag{2.22}$$

Figure 2.18 shows a comparison between the viscous transfer function $\frac{\hat{\Gamma}}{\hat{\Gamma}_{QS}}$ of the circulation response from computational simulations and the corresponding potential flow one, which is different from the Theodorsen function $C(k)$. Rather, it is given as (Bisplinghoff *et al.*, 1996, pp. 275-276)

$$\frac{\hat{\Gamma}_P}{\hat{\Gamma}_{QS}}(k) = \frac{-2e^{-ik}}{ik\pi\left(H_1^{(2)}(k) + iH_0^{(2)}(k)\right)}, \tag{2.23}$$

where Γ_P denotes the potential flow unsteady bound circulation. Similar to the lift transfer function $C_{\mathrm{v}}(k;R) = \frac{\hat{C}_{L_C}(k;R)}{\hat{C}_{L_{QS}}(k)}$, the circulation transfer function $\frac{\hat{\Gamma}}{\hat{\Gamma}_{QS}}$ experiences more phase lag due to viscosity at high frequencies than its potential flow counterpart.

Figure 2.19 shows the vorticity contours during the cycle of a harmonically pitching NACA 0012 airfoil about its quarter-chord with 3° amplitude at $k = 1$ and two different Reynolds numbers $R = 10^5$ and $R = 10^4$. First, figure 2.19(a) shows that for this relatively high k, the wake is more deformed at the instants of zero pitching angle ($\alpha = 0$) and maximum angular velocity $\dot{\alpha}$ in comparison to the instants of maximum α with $\dot{\alpha} = 0$. This fact, similar to the theoretical findings above, implies that the airfoil would be more prone to trailing edge stall

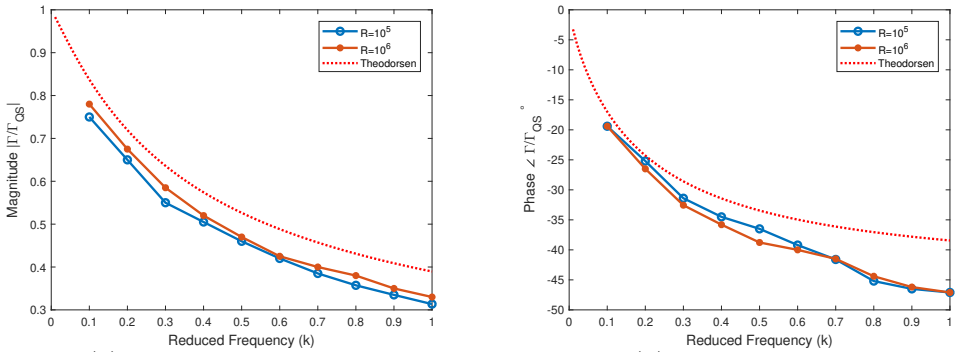

(a) Magnitude Variation. (b) Phase Variation.

Figure 2.18: Computational results of the frequency responses of the unsteady, viscous, bound circulation at different Reynolds numbers. A behavior similar to the circulatory lift frequency response is observed: the larger the frequency, the larger the discrepancy in phase between inviscid and viscous responses.

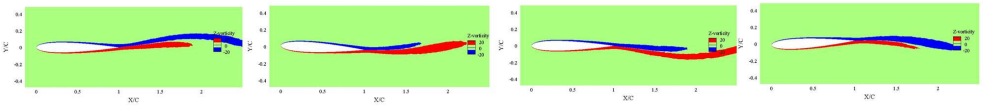

$\alpha = 0, \dot{\alpha} > 0$ $\alpha = 3°, \dot{\alpha} = 0$ $\alpha = 0, \dot{\alpha} < 0$ $\alpha = -3°, \dot{\alpha} = 0$

(a) $R = 10^5$ and $k = 1$.

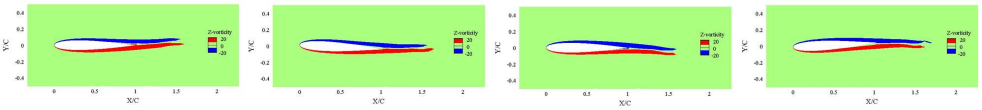

$\alpha = 0, \dot{\alpha} > 0$ $\alpha = 3°, \dot{\alpha} = 0$ $\alpha = 0, \dot{\alpha} < 0$ $\alpha = -3°, \dot{\alpha} = 0$

(b) $R = 10^4$ and $k = 1$.

Figure 2.19: Vorticity contours during the cycle of a harmonically pitching NACA 0012 airfoil about its quarter-chord with 3° amplitude at $k = 1$ and (a) $R = 10^5$, (b) $R = 10^4$. As R decreases, viscosity damps the deformation of wake vorticity.

at the instants of maximum $\dot{\alpha}$ when oscillating at high frequencies. Second, the comparison between the two sets of figures at the two values of R indicates a much less wake activity (deformation) for lower R, which is intuitively expected due to viscous damping. From a dynamical system perspective, this damping of wake vorticity will be typically associated with lag in its development which, via conservation of circulation, points to a lag in the bound circulation development. Therefore, it may explain the larger phase lag of the lift frequency response found at lower Reynolds numbers and higher frequencies.

2.6.3 Lag in Circulation Development and the Kutta Condition

One may be able to relate the observed lag in the circulatory lift frequency response (due to lag in the circulation development) to the Kutta condition. Note that the trailing edge singularity term in the pressure distribution (2.9) is the main modification introduced to the inviscid pressure distribution (2.3). Therefore, the observed additional lag in the lift response may be related to the pressure near the trailing edge, which motivates the following analysis.

The Kutta condition at the sharp trailing edge can be stated in several ways such as (i) finite velocity, (ii) zero loading, or (iii) continuous pressure, among others (see Sears, 1956). In fact, some of these representations are, indeed, exact. For example, clearly, the pressure must be continuous at the trailing edge. That, is

$$\lim_{y\to 0^+} P(TE, y) = \lim_{y\to 0^-} P(TE, y). \tag{2.24}$$

However, the inviscid pressure distribution over the plate represents the distribution at the edge of the boundary layer. That is, applying the condition (2.24) within the framework of potential flow results in $P_1 = P_2$, where the points 1 and 2 lie on the edge of the boundary layer at the trailing edge station as shown in figure 4.7.

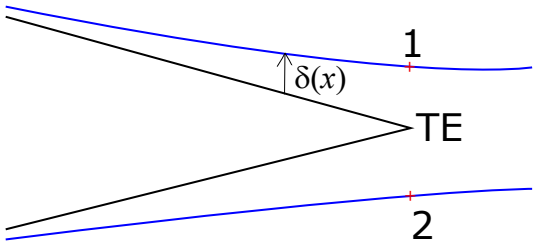

Figure 2.20: A zoom at the trailing edge and its boundary layer. The blue lines represent the edge of the boundary layers and the red dots (points 1 and 2) represent the edge of the boundary layers at the trailing edge x station. The potential flow theory, ignoring the boundary layers, assumes the points 1, 2, and the trailing edge all lie on the top of each other. Hence, the Kutta condition (continuous pressure at the trailing edge) would dictate $P_1 = P_2$ neglecting the pressure rise across the boundary layer and its effect on the circulation development over the airfoil.

While Prandtl's boundary layer assumption (pressure is constant along the boundary layer thickness) is valid over the majority of the airfoil length, it is not necessarily valid in the singular trailing edge region. As such, if ΔP is the pressure rise across the boundary layer, then the condition (2.24) results in

$$P_1 - \Delta P_1 = P_2 - \Delta P_2, \tag{2.25}$$

which is also suggested by Preston (1943) and Spence (1954) as a modification of the classical Kutta condition ($P_1 = P_2$). Since the points 1 and 2 lie on the edge of the boundary layer, one can use the unsteady Bernoulli's equation to relate P_1 and P_2 as (Bisplinghoff *et al.*, 1996; Katz & Plotkin, 2001)

$$\frac{P_1}{\rho} + \frac{1}{2}V_1^2 + \frac{\partial \phi_1}{\partial t} = \frac{P_2}{\rho} + \frac{1}{2}V_2^2 + \frac{\partial \phi_2}{\partial t}, \tag{2.26}$$

where V is the potential flow velocity at the edge of the boundary layer and ϕ is the corresponding velocity potential. Combining (2.25) and (2.26) and realizing that $\phi_1 - \phi_2 = \Gamma$, one obtains

$$\dot{\Gamma} = \frac{1}{2}\left(V_2^2 - V_1^2\right) + \frac{\Delta P_2 - \Delta P_1}{\rho}. \tag{2.27}$$

Equation (2.27) represents an exact (derived) version of the hypothesized Kutta condition. In particular, it governs the evolution of the bound circulation over the airfoil; i.e., it provides the dynamics of the bound circulation. Interestingly, it can be derived from a completely different point of view than the continuity argument (2.24) which we opt to show below. The underpinning concept is that the circulation is instantaneously conserved. That is, the instantaneous rate of change of circulation $\dot{\Gamma}$ is related to the total vorticity flux at separation (Sears, 1976*b*). As such, assuming that separation occurs at the trailing edge (complying

with the triple deck theory used in this section), we write

$$\dot{\Gamma} = -\left[\int_0^{\delta_1} \zeta(y)u(y)dy + \int_{-\delta_2}^{0} \zeta(y)u(y)dy\right], \tag{2.28}$$

where ζ is the clockwise vorticity, u is the velocity parallel to the wall inside the boundary layer, and δ is the boundary layer thickness. Also, Γ is assumed clockwise positive in this chapter. Then, one can use the boundary layer theory along a curved surface (Goldstein, 1938, pp. 119-120; Sears, 1956) to write

$$\int_0^{\delta_1} \zeta u dy = \int_0^{\delta_1} \left(\frac{\partial u}{\partial y} + \kappa u\right) u dy = \frac{V_1^2}{2} + \frac{\Delta P_1}{\rho}, \tag{2.29}$$

where κ is the curvature of the wall. Note that base on boundary layer theory (Goldstein, 1938), $\kappa \int_0^{\delta_1} u^2 dy$ can be written as $-1/\rho \int_0^{\delta_1} \frac{\partial P}{\partial y} dy$. Writing an expression for the vorticity flux out of the boundary layer on the lower surface similar to (2.29) and substituting both in (2.28), one immediately arrives at the condition (2.27).

Setting $\Delta P_1 = \Delta P_2 = 0$ along with $V_{1,2} = U \pm \frac{1}{2}\gamma_{TE}$ as typically done in the classical theory of unsteady aerodynamics, the condition (2.27) results in

$$\dot{\Gamma}_{\text{Kutta}}(t) = -U\gamma_{TE}(t), \tag{2.30}$$

where γ_{TE} is the circulation distribution at the trailing edge (instantaneous strength of the shed vortex sheet per unit length at the shedding time). Equation (4.6) is equivalent to the classical Kutta condition ($P_1 = P_2$) and it is ubiquitously used in the classical theory of unsteady aerodynamics (Wagner, 1925; Loewy, 1957; Bisplinghoff *et al.*, 1996, equation 5-318; Peters, 2008, equation 11-c, among others). Note that the main difference between the exact condition (2.27) and the classical Kutta condition (4.6) is two assumptions: (i) linearization ($V_{1,2} = U \pm \frac{1}{2}\gamma_{TE}$) and (ii) negligence of the curvature terms ΔP_1, ΔP_2. The first assumption may be valid for small disturbance (small angle of attack). Using a higher

fidelity computational simulations, we assess the validity of the second assumption. Figure 2.21 shows a comparison between the Kutta's rate of circulation development $\dot{\Gamma}_{\text{Kutta}}$ and the viscous contribution proportional to $\Delta P_{TE} = P_2 - P_1$, at different frequencies and Reynolds numbers. It is found that the viscous contribution $\dot{\Gamma}_{\Delta P}$ relative to the inviscid $\dot{\Gamma}_{\text{Kutta}}$ is not sensitive to frequency; it mainly depends on Reynolds number. This ratio is about 18%, irrespective of the frequency k, at the lower Reynolds number $R = 10^4$ versus 6-7% at $R = 10^5$. Moreover, a higher frequency, though does not significantly affect the magnitude, causes a significant phase shift for the viscous contribution, which will in turn affect the phase of the total lift force at high-frequencies.

In summary, the lower Reynolds number, the larger the viscous contribution to the bound circulation development relative to the inviscid one; and the higher the frequency, the larger phase shift of this viscous contribution. That is, at higher frequencies and lower Reynolds numbers, the viscous contribution to the bound circulation rate of development is of relatively larger magnitude and phase shift. This point, in addition to the wake viscous damping discussed above, may help explain the physical reasons behind the additional phase lag in the lift response at high k and low R that could not be captured by the inviscid theory even at very small amplitudes. Since this viscous contribution is essentially neglected in the classical potential flow framework by virtue of the classical Kutta condition (4.6), it is inferred that the Kutta condition is one of the reasons behind the inaccurate phase prediction of Theodorsen's lift frequency response function.

2.6.4 Viscous Reduction in Virtual Mass

A closer look at the viscous contribution B_{v} in (2.14) and its contribution to the lift in (2.19) implies that the viscous lift contribution is proportional to (in phase with) the "effective"

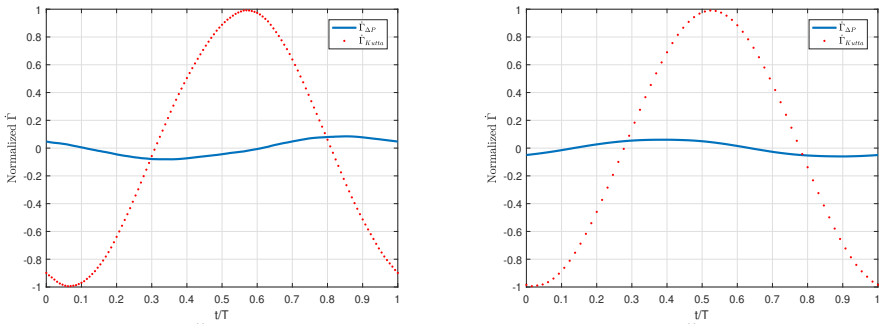

(a) $R = 10^5$ and $k = 0.1$.

(b) $R = 10^5$ and $k = 1$.

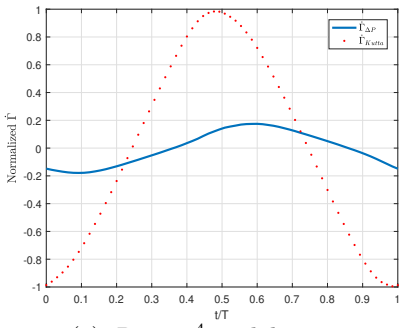

(c) $R = 10^4$ and $k = 0.3$.

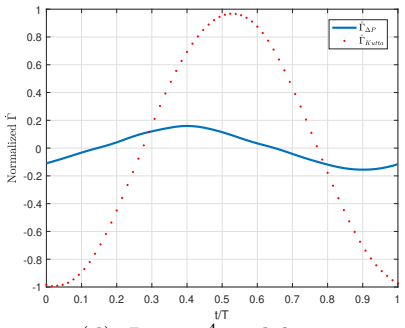

(d) $R = 10^4$ and $k = 1$.

Figure 2.21: Inviscid and viscous contributions ($\dot{\Gamma}_{\text{Kutta}}$, $\dot{\Gamma}_{\Delta P}$) to the rate of bound circulation development over NACA 0012 undergoing a pitching oscillation about the quarter-chord point at different reduced frequencies and Reynolds numbers.

angle of attack

$$\alpha_{\text{eff}} = \frac{1}{U^2}\left[\frac{1}{2}a_0(t) + 2\sum_{n=1}^{\infty} n a_n(t)\right].$$

Note that this α_{eff} is different from the common notion of the effective angle of attack in potential flow. The former is a term special to the developed theory while the latter is simply given by the angle of attack $\alpha_{3/4}$ at the three-quarter-chord point (Schlichting & Truckenbrodt, 1979, pp. 80). Equation (2.14) implies that the viscous contribution $-\pi\tilde{B}_v$ to the lift coefficient is simply proportional to α_{eff}:

$$-\pi\tilde{B}_v(t) = f\left(|\alpha_{\text{eff}}(t)|\right)\alpha_{\text{eff}}(t),$$

where $f(.)$ is a nonlinear function coming from the numerical solution of Chow & Melnik (1976) to the triple deck problem, specifically from figure 2.3(b) and equation (2.2). This nonlinear function mainly affects the magnitude of $\tilde{B}_v$ with a very weak effect on its phase, as shown in Figs. 2.22, 2.23: the viscous contribution is almost exactly in phase with α_{eff}.

Considering the studied case of a pitching flat plate about its quarter-chord point, the above definition of the effective angle of attack can be manipulated to write its Fourier transform as

$$\hat{\alpha}_{\text{eff}} = \hat{\alpha}_{3/4}C(k) - A_\alpha\left(3ik - 2k^2\right).$$

Since the viscous contribution is proportional to α_{eff}, it is fair to write

$$-\pi\hat{\tilde{B}}_v(t) = 2\pi A\left[\hat{\alpha}_{3/4}C(k) - A_\alpha\left(3ik - 2k^2\right)\right], \tag{2.31}$$

where A is the proportionality constant (actually dependent on α_{eff}). Written this way, equation (2.31) implies that the viscous contribution actually has a component that is in phase

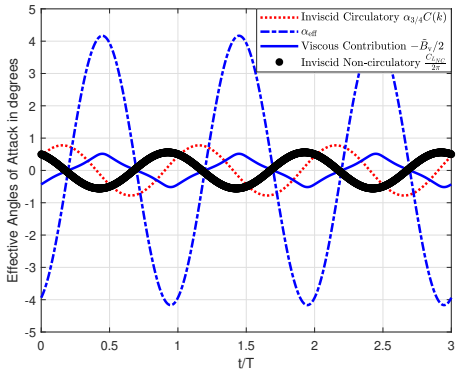

Figure 2.22: A comparison between the time history of the inviscid circulatory lift $\alpha_{3/4}C(k)$, the effective angle of attack α_{eff} for the developed viscous theory, the weighted effective angle of attack or the viscous contribution $-\pi\tilde{B}_v$, and the inviscid added-mass lift. All lift coefficients are represented as effective angles of attack (i.e., normalized by 2π). Simulation of the developed viscous model is performed for a flat plate pitching about its quarter-chord point with amplitude 1° at $k = 1$ and $R = 10^4$. The viscous contribution $-\pi\tilde{B}_v$ is opposite to the inviscid non-circulatory lift, decreasing the added mass effect by 92%.

with the inviscid circulatory lift $\hat{\alpha}_{3/4}C(k)$. Moreover, recalling the inviscid non-circulatory lift in this case:

$$\hat{C}_{L_{NC}} = \pi A_\alpha \left(ik - k^2/2\right),$$

equation (2.31) implies that the second component $-A_\alpha\left(3ik - 2k^2\right)$ of the viscous contribution is opposite to the non-circulatory lift (added mass). This fact is clearly seen in Figs. 2.22, 2.23. Therefore, adding $-\pi\tilde{B}_v$ to the inviscid lift coefficient would decrease the added mass and cause a phase lag for its contribution.

It is noteworthy to comment on the results shown in figure 2.22 for a pitching flat plate about its quarter-chord point with amplitude 1° at $k = 1$ and $R = 10^4$. In addition to the points addressed above ($-\pi\tilde{B}_{\text{v}}$ is almost-exactly in phase with α_{eff} and out of phase with $C_{L_{NC}}$), it is interesting to see the apparent nonlinear response of the viscous contribution even at this very small amplitude. Moreover, the phase lag between the inviscid circulatory lift and viscous contribution is very clear, also in the Argand diagrams in figure 2.23. More

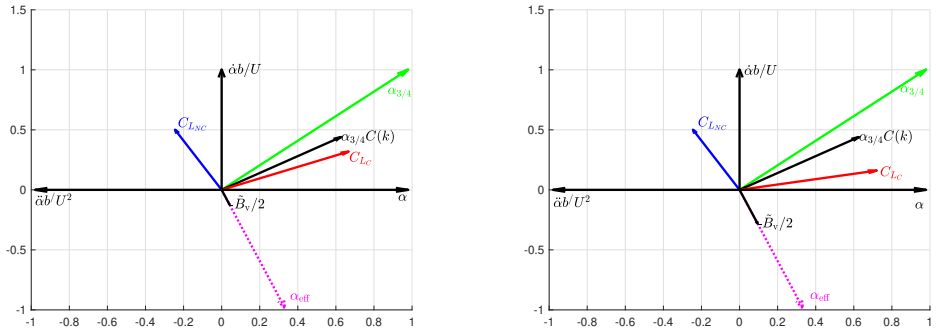

(a) $R = 10^5$ and $k = 1$.

(b) $R = 10^4$ and $k = 1$.

Figure 2.23: Argand diagram showing different components of lift for a pitching flat plat about its quarter-chord point at $k = 1$ and two different Reynolds numbers. All lift coefficients are represented as effective angles of attack (i.e., normalized by 2π). The term α_{eff} is scaled down to one fourth to enhance visualization. The viscous contribution $\tilde{B}_v$ increases as R decreases, resulting in a larger phase difference between the inviscid circulatory contribution $\alpha_{3/4}C(k)$ and the total (viscous) circulatory component C_{L_c}, or a larger decrease in the added mass effect.

importantly, the viscous contribution is as strong as the inviscid one at this low R and high k: its magnitude is 66% of the inviscid circulatory lift or 92% of the non-circulatory lift. Of course, decreasing the added mass by 92% would have a significant effect on flutter (Bisplinghoff *et al.*, 1996), if it happens at this low R and high k.

2.7 Conclusion

The triple deck theory is a boundary layer theory developed in the 1970's to model local interactions in the vicinity of the trailing edge of an airfoil due to the discontinuity of the viscous boundary condition: from a zero-slip on the airfoil to a zero-stress on the wake center line. We utilized this theory to develop a viscous extension of the classical theory of unsteady aerodynamics, equivalently an unsteady extension of the viscous boundary layer theory. In particular, we developed an analytical model for the viscous unsteady lift response over a two-dimensional airfoil due to small amplitude maneuvers. The developed model admits airfoil flexibility (i.e., time-varying camber). The main modification to the classical

thin airfoil theory is the introduction of a trailing edge singularity term in the pressure distribution. The amplitude of such a correction cannot be obtained from potential flow. The Kutta condition dictates that it must vanish. We dodged the Kutta condition and determined such a correction from pure viscous considerations: by drawing connections with the steady triple deck theory. Using the developed model, we constructed, for the first time, a theoretical viscous (Reynolds number dependent) extension of Theodorsen's lift frequency response. It was found that viscosity induces a significant additional lag in the lift development that is not captured by Theodorsen, particularly at higher reduced frequencies and lower Reynolds numbers. This finding was also supported by laminar simulations of Navier Stokes equations on a sinusoidally pitching NACA 0012 at low Reynolds numbers and using Reynolds-Averaged Navier Stokes equations at relatively high Reynolds numbers. It was found that the viscosity-induced lag in the lift response can be interpreted as lag in the circulation development. This lag in the circulation dynamics was related to the Kutta condition via deriving an equation for the rate of change of circulation around the airfoil in terms of the pressure rise across the boundary layer at the trailing edge. It was concluded that the viscous contributions due to this pressure rise, which are typically neglected in a potential flow analysis (employing the Kutta condition at the trailing edge), affect the magnitude of circulation development at lower Reynolds numbers and induce phase shift at higher frequencies. That is, the Kutta condition is one of the reasons behind the inaccurate phase prediction of Theodorsen's lift frequency response function. From a different perspective, the viscous contribution to the unsteady lift was shown to significantly decrease the virtual mass at low Reynolds numbers and high frequencies. Recalling that both the unsteady phase lag of the circulatory lift and the virtual mass play crucial roles in determining the flutter boundary, these findings may shed some light on the reasons behind our meager state of flutter predictability using potential flow; it is expected that the developed theory would enhance flutter prediction, particularly when occurring at high frequencies and low Reynolds numbers.

Chapter 3

Viscous Extension of the Unsteady Vortex Lattice Method

3.1 Background

As discussed in chapter 2, potential flow theory has been used in a wide range of applications. These potential flow based approaches (e.g. Birnbaum & Ackermann (1923) thin airfoil theory, Prandtl (1918) lifting line theory, Wagner (1925) and Theodorsen (1935) models, etc), typically result in integral equations with singular kernels. As discussed by Belotserkovskii (1977), one of the most convenient techniques to solve singular integral equations is via discretization resulting in linear algebraic system of equations (James, 1972). This approach constructs the basis of the so-called Vortex Lattice Method (VLM) introduced by Falkner (1943), which is customarily ascribed to the steady-state scenarios. In the case of transient problems such as those associated with a moving airfoil (pitching, plunging or surging), the Unsteady Vortex Lattice Method (UVLM) is used, which allows for wake deformation and any arbitrary time-varying motion.

Kutta condition has been extensively used as the needed auxiliary condition potential flow framework (either the analytical or numerical version). Therefore, it is essential for aerodynamicists to have a fundamental grasp of the Kutta condition and how the viscosity is explicitly neglected in potential flow, but implicitly plays a vital role through the Kutta condition. It is a proper condition for steady attached flows at high Reynolds numbers, which may also be applicable to the unsteady problems at a relatively small oscillation frequency. However, the discontent with the Kutta condition at highly unsteady flows (high reduced frequency) or more viscous ones (low Reynolds numbers) has been reported in numerous studies (Archibald, 1975; Ho & Chen, 1981; Poling & Telionis, 1986; Ansari *et al.*, 2006*b*; La Mantia & Dabnichki, 2009; Xia & Mohseni, 2013; Darakananda & Eldredge, 2019). The reader is referred to chapter 2 for more references that reported flaws with the application of Kutta condition. In chapter 2, we developed a viscous extension of the classical potential flow unsteady aerodynamics (with emphasis on the lift frequency response problem) by relaxing the Kutta condition. This approach naturally introduces a singularity at the trailing-edge, which must vanish according to the Kutta condition. In contrast, its strength is obtained from the triple-deck boundary layer theory, which is dependent on the Reynolds number and angle of attack. Consequently, unlike the Theodorsen inviscid response which is only a function of motion reduced frequency, the new model provides dependence on both the motion frequency and Reynolds number.

The natural extension of our previous work (provided in chapter 2) is to adopt a numerical model to account for the viscous Kutta condition while considering wake deformation (in contrast to the flat wake assumption in the analytical model- see Kadlec & Davis (1979) for the effect of wake roll-up) and arbitrary motion kinematics (not just harmonic and step inputs), hence making it useful for many applications in aeronautical engineering. In fact,

because of the ability of the potential flow-based methods, such as VLM or discreet-vortex method (DVM), to capture the essential macroscopic physics of the flow, they are adopted for variety of engineering and research problems. There have been several previous efforts to develop extensions of UVLM or DVM to regions where the primary potential flow assumptions fade out, hence broadening the applicability of the aforementioned methods. For instance, Wang & Eldredge (2013); Ford & Babinsky (2013); Hemati *et al.* (2014); Ramesh *et al.* (2014); Darakananda & Eldredge (2019); SureshBabu *et al.* (2019); Epps *et al.* (2019) among others have developed extensions of the UVLM or DVM to high angle of attack maneuvers, necessary for the analysis of the modern applications of bio-inspired flight and dynamic stall.

Our contribution in this chapter revolves around the integration of the developed unsteady viscous theory in chapter 2 and the numerical unsteady vortex lattice method (UVLM). This goal is achieved by replacing the Kutta condition with a viscous condition based on the triple-deck boundary layer theory. However, unlike the DVM and analytical models, the Kutta condition is not explicitly applied in the UVLM. In fact, the application of the Kutta condition is quite subtle; there are nuances between various potential flow methods in this regard. For example, in analytical models, whether steady (such as thin airfoil theory), or unsteady (such as Wagner and Theodorsen), the Kutta condition is explicitly imposed as a separate equation, which completes the system of equations. On the other hand, in some discrete numerical approaches such as the traditional VLM (Hedman, 1966; Katz & Plotkin, 2001), the no-penetration boundary condition which must be satisfied on each panel, fulfills the number of equations required to calculate the unknown strength of the vortices on each panel; apparently there is no need for an additional equation (Kutta condition). However, a unique solution cannot be obtained with this system of equations as described above and the resulting outcome will not generate the correct lift force (circulation). Then, one might inquire about how the Kutta condition can be applied (or relaxed) in the vortex lattice

method (steady or unsteady).

To answer the above questions and develop the targeted viscous UVLM, we first show how the Kutta condition is implicitly satisfied in the original (inviscid) (U)VLM relying on Hilbert matrices algebra that constitutes the basis of (U)VLM. We show that the Kutta condition is related to the locations of the collocation point (the point at which a vortex is assigned on each panel) and control point (the point at which the no-penetration boundary condition is satisfied on each panel) in (U)VLM. As such, the conventional locations of the collocation and control points on each panel (which were dictated to be at quarter-chord and three-quarter-chord points, respectively, according to the Kutta condition) are updated at each time step according to the viscous correction coming from the triple-deck boundary layer theory, depending on the instantaneous angle of attack and the value of the Reynolds number. As a result, we develop a viscous extension of the UVLM by adapting the mesh at each time step to account for the deviation from the Kutta condition obtained from the triple-deck boundary layer theory. In the coming sections, we firstly touch upon the role of the Kutta condition in potential flow framework and how the results from the triple-deck boundary layer theory can be utilized to relax the Kutta condition. Then, we show the relation between the Kutta condition and the collocation and control points in VLM followed by the development of the viscous UVLM via modifying the Kutta condition and employing the triple-deck theory. Finally, we provide results and validations in terms of frequency response (i.e. Theodorsen function), step response (i.e. Wagner function), and lift history for an arbitrary time-varying (e.g. multi-frequency) input.

3.2 The Kutta condition and triple-deck boundary layer theory

Based on the information in chapter 2, this section provides a summary of how the triple-deck theory is implemented in potential flow framework after relaxing the Kutta condition. In almost all the introductory fluid mechanics courses, after constructing the flow field around a cylinder by adding two elementary flows (an angled free stream and a doublet), it is shown that no lift force can be generated unless a vortex is placed at the center of a cylinder, which retains the cylinder as a streamline yet generate circulation or lift force through Kutta-Joukowsky theorem. The question is that how can the strength of the circulation be found? There is no means to find the strength of this circulation in the potential flow framework unless an auxiliary condition (Kutta condition) is utilized. In the above scenario where the problem is formulated in the cylinder domain, the Kutta condition dictates the value of the circulation by forcing the TE (the most downstream point of the cylinder) to be a stagnation point. To better comprehend the role of the Kutta condition, it is better to convert the velocity field to the pressure field through the Bernoulli's equation and observe that the TE singularity is removed by applying the Kutta condition. It should be noted that there is also a singularity at the leading-edge (LE), which remains intact.

It can be seen that, conceptually, the Kutta condition introduces some viscous effects, although it is just a mathematical trick to remove the TE singularity. Therefore, any attempt to include viscous effects in the potential flow framework is to be performed through the edge condition. If the Kutta condition is relaxed which corresponds to adding a new vortex of unknown strength at the center of the cylinder, by utilizing the Joukowsky transformation the velocity u on the flat plate of length $2b$ in a free stream U_∞ at a steady angle of attack

α_s can be written as

$$\frac{u}{U_\infty} = 1 \pm \alpha_s \sqrt{\frac{1-x}{1+x}} \mp \frac{B_s}{\sqrt{(1-x^2)}}, \tag{3.1}$$

where x is the plate coordinate normalized by b (i.e. $-1 \leq x \leq 1$). The first row of signs corresponds to the suction side and the second row corresponds to the pressure side of the plate. The first two terms on the right hand side of Equation (3.1) represent the potential flow solution, satisfying the Kutta condition. However, the third term is the result of deviation from the Kutta condition. In other words, the Kutta condition dictates $B_s = 0$ so that TE singularity is removed. It should be noted that similar to the common leading edge singularity, the new TE singularity is an integrable singularity: although the velocity (or pressure) is singular, the integrated lift and moment are finite. Thus, by applying Bernoulli's equation to Equation (3.1) and integrating over the plate, the lift and moment coefficients can be written as

$$C_l = 2\pi \left(\alpha_s - B_s\right) \ , \tag{3.2}$$

$$C_m = 0.5\pi \left(\alpha_s - 2B_s\right) \ . \tag{3.3}$$

respectively. If the formulation is transformed into the cylinder domain, it can easily be shown that after relaxing the Kutta condition, the new stagnation point sits at $\theta_{st} = \arcsin B_s$.

In order to find the strength of B_s, Brown & Stewartson (1970) devised the triple-deck boundary layer theory for a lifting flat plate, to model the local interactions between the Blasius boundary layer and the shear layer in the wake in the immediate vicinity of the TE. They constructed an asymptotic solution ($\epsilon \longrightarrow 0$ where ϵ is related to the Reynolds

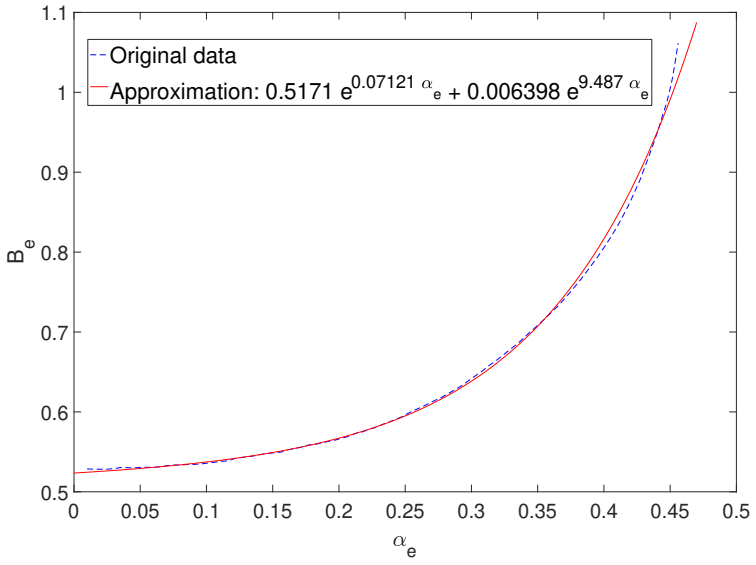

Figure 3.1: Numerical solution of the lower deck equations

number Re as $\epsilon = Re^{-1/8}$) for this viscous interaction near the TE to determine the value of B_s. Their approach resulted in a nonlinear boundary value partial differential equation, which they solved by linear approximations. Six years later, Chow & Melnik (1976) solved this partial differential equation numerically, and provided the strength of the singularity $B_s = 2\alpha_s\epsilon^3\lambda^{-5/4}B_e(\alpha_e)$ in terms of the normalized angle of attack $\alpha_e = \alpha_s\epsilon^{-1/2}\lambda^{-9/8}$, where $\lambda = 0.334$ is the Blasius skin friction coefficient. Note that if α_s is zero, then B_s is also zero. Figure 3.1 shows the nonlinear relation between B_e and α_e, which possesses a vertical asymptote at $\alpha_e = 0.47$ where TE stall occurs according to the triple-deck results (Brown & Stewartson, 1970). This value of α_e yields $\alpha_s = 3.1 - 4.2°$ for $Re = 10^4 - 10^6$ before the flow separates further away from the TE (TE stall). Moreover, to facilitate the usage of this plot, an exponential function that approximates the numerical results of the steady lower deck is provided in Figure 3.1.

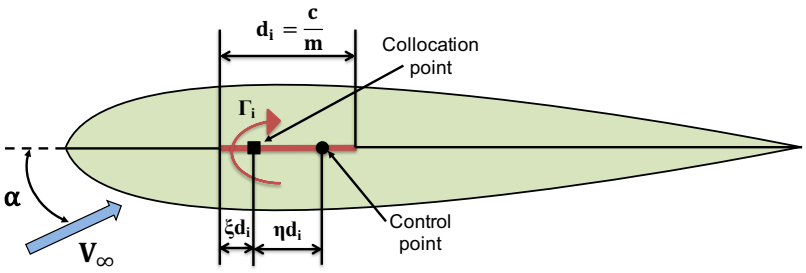

Figure 3.2: Schematic of the problem setup in the VLM.

3.3 Relation between the VLM mesh and the Kutta condition

The UVLM represents the airfoil by its camber-line, which is divided into several panels. One vortex and one control point are assigned to each panel, as shown in Figure 3.2. At each panel of length $d_i = \frac{c}{m}$, where c is the chord length and m the number of panels, two values are crucial for the current problem: the fraction ξ of the panel length where the vortex is located and the fraction η between this point and the control point, where the no-penetration boundary condition is going to be applied.

To show the relation between the Kutta condition and the values of ξ and η, consider the steady case of a symmetric airfoil subject to a free stream U_∞ at a small angle of attack α. According to the Biot-Savart law for a vortex induced velocity, the no-penetration boundary condition is satisfied on each control point as

$$\sum_{i=1}^{m} \frac{-m\Gamma_i}{2\pi c} \frac{1}{j-i+\eta} + U_\infty \alpha = 0 \ , j = 1, 2, ..., m. \tag{3.4}$$

It can be seen from Equation (3.4) that the evaluation of the no-penetration boundary condition does not depend on ξ and is only a function of η. Let $A_{ij} = \frac{-m}{2\pi c} \frac{1}{(i-j+\eta)}$ be the influence coefficient. Then, Equation (3.4) can be expressed in matrix form for all the control

points as

$$[A]\begin{Bmatrix}\Gamma_1\\ \Gamma_2\\ \vdots\\ \Gamma_m\end{Bmatrix} = -U_\infty\alpha\begin{Bmatrix}1\\ 1\\ \vdots\\ 1\end{Bmatrix} . \tag{3.5}$$

The Γ_i's are the unknown circulations on each panel. It is noteworthy to mention that the form of the influence coefficients $A_{ij} = \frac{-m}{2\pi c}$ defines a special kind of the Hilbert matrix (Collar, 1951). Exploiting the properties of the Hilbert matrix the circulations Γ_i's are given by

$$\Gamma_i = 2\pi U_\infty\alpha\frac{c}{m}\sum_{j=1}^{m} R_{ij} , \tag{3.6}$$

where $[R] = \frac{1}{2\pi d}[A]^{-1}$ and $d = c/m$. Then, the resulting lift and moment coefficients are given by

$$C_l = \frac{2}{U_\infty c}\sum_{i=1}^{m}\Gamma_i , \tag{3.7}$$

$$C_m = \frac{2}{U_\infty c^2}\sum_{i=1}^{m}\Gamma_i x_i , \tag{3.8}$$

respectively. According to Collar (1951), we have:

$$\sum_{i=1}^{m}\sum_{j=1}^{m} R_{ij} = m\eta \ . \tag{3.9}$$

Substituting equations (3.6) and (3.9) into Equation (3.7), the lift coefficient can be found as

$$C_l = 4\pi\alpha\eta \ . \tag{3.10}$$

Equation (3.10) provides the lift coefficient given by the VLM. If this equation is compared with the lift coefficient ($C_l = 2\pi\alpha$) dictated by the Kutta condition, it is clear that $\eta = 0.5$. This condition, which is based on global matching of the VLM and analytical potential flow theory, stipulates that the clearance between the collocation point and the control point is half of the panel length.

In order to determine the location of the collocation point, the moment coefficient should be considered. The sum in Equation (3.8) can be written as

$$\sum_{i=1}^{m} \Gamma_i x_i = \frac{c}{m}\xi \sum_{i=1}^{m} \Gamma_i + \frac{c}{m} \sum_{i=1}^{m} \Gamma_i (i-1) \ . \tag{3.11}$$

Note that the first term in Equation (3.11) can be determined from Equation (3.9). In addition, making use of the properties of the Hilbert matrix (Collar, 1951), we write

$$\sum_{i=1}^{m} (i-1) \sum_{j=1}^{m} R_{ij} = -0.5m(m-1)\eta(\eta-1) \ . \tag{3.12}$$

Combining equations (3.9), (3.11), and (3.12) and substituting into Equation (3.8), the

moment coefficient at the leading edge calculated by the VLM is written as

$$C_m = 4\pi\alpha \frac{1}{m} \left[\xi - 0.5(m-1)(\eta-1)\right] \eta \; . \tag{3.13}$$

If C_m is compared to the Kutta's value $C_m = \frac{\pi\alpha}{2}$ at the leading edge of a flat plate and considering $\eta = 0.5$ coming from lift matching, then $\xi = 0.25$ independent of the number of panels m. In conclusion, the ubiquitous choice of the collocation point and control point at the quarter-chord and three-quarter-chord implicitly satisfy the Kutta condition in the VLM framework.

Since the main goal of this effort is to develop a viscous extension of (U)VLM, we tackle the problem with the same procedure discussed above, but using the results of the viscous extension of potential flow. Comparing the VLM lift coefficient given by Equation (3.10) to the viscous lift coefficient given by Equation (3.2), we find the value of η as

$$\eta = 0.5 \left(1 - \frac{B_s}{\alpha_s}\right) \; . \tag{3.14}$$

Note that B_s varies nonlinearly with α_s, so the term B_s/α_s approaches zero as $\alpha_s \to 0$. Equation (3.14) provides a new rule for mesh spacing in the VLM to account for the viscous correction of the Kutta condition. In fact, η is no longer a constant value as it is in the classical VLM but a function of the TE singularity B_s, which depends on the angle of attack α_s and the Reynolds number Re.

Similarly, matching the moment coefficient would provide a new viscous rule for ξ. The comparison between equations (3.13) and (3.3) after replacing the viscous value of η from Equation (3.14) results in

$$\xi = \frac{1}{4}\left(1 + \frac{B_s}{\alpha_s}\right) + \frac{mB_s}{4\alpha_s}\left(\frac{\alpha_s - 2B_s}{\alpha_s - B_s}\right) \; . \tag{3.15}$$

Equations (3.14) and (3.15) provide viscous corrections to the common mesh spacing of quarter and three-quarter in the vortex lattice method.

In Equation (3.15), a clear dependence of ξ on the number of panels m is observed. This dependence vanishes only if $B_s = 0$ or $B_s = 0.5\alpha_s$. The latter choice outside the scope of the current theory as it corresponds to situation well beyond the TE stall. For instance, when $Re = 10^5$ the latter choice results in $B_e \cong 4.7$, which is not in the valid region of triple-deck theory (see Figure 3.1). As described above, when the Kutta condition is applied ($B = 0$), the dependence on the number of panels disappears. Therefore, after relaxing the Kutta condition ($B \neq 0$) the dependence of ξ on m cannot be avoided.

3.4 UVLM Methodology and Its Extension

It is a common practice to carry the obtained results for the panel layout from the VLM to UVLM. In other words, the location of the collocation point (quarter-chord) and control point (three-quarter-chord) on each panel that are calculated from a steady analysis are typically used in the unsteady version as well. The only difference is that for the unsteady cases, the wake must be considered. In that regard, a vortex is shed from the TE at each time step. The strength of the shed vortex Γ_{TE} is calculated at each time step such that it satisfies Kelvin's conservation of circulation as follows

$$\sum_{i=1}^{N} \Gamma_i \left(t_k\right) + \sum_{i=1}^{N_W} \Gamma_{Wi} = 0 \tag{3.16}$$

or equivalently

$$\sum_{i=1}^{N} \Gamma_i \left(t_k\right) + \Gamma_{TE} = -\sum_{i=1}^{N_W - 1} \Gamma_{Wi} = \sum_{i=1}^{N} \Gamma_i \left(t_{k-1}\right) \equiv \Gamma_B \left(t_{k-1}\right), \tag{3.17}$$

where Γ_i's are the bound circulations (the strength of the vortices on the airfoil), Γ_W's are the wake circulations, t_k is the current time and t_{k-1} is the previous time-step. Therefore, equation (3.5) is modified to account for the shed vortices in the wake and the following system of equations is obtained:

$$\begin{bmatrix} a_{11} & a_{12} & \cdots & a_{1N} & a_{1W} \\ a_{21} & a_{22} & \cdots & a_{2N} & a_{2W} \\ \vdots & \vdots & \ddots & \vdots & \vdots \\ a_{N1} & a_{N2} & \cdots & a_{NN} & a_{NW} \\ 1 & 1 & \cdots & 1 & 1 \end{bmatrix} \begin{bmatrix} \Gamma_1(t_k) \\ \Gamma_2(t_k) \\ \vdots \\ \Gamma_N(t_k) \\ \Gamma_{WN_W} \end{bmatrix} = \begin{bmatrix} \mathrm{RHS}_1 \\ \mathrm{RHS}_2 \\ \vdots \\ \mathrm{RHS}_N \\ \Gamma_B(t_{k-1}) \end{bmatrix} \tag{3.18}$$

where a_{iW}'s are the influence coefficients at the collocation points of the newly shed vortex. It is worth noting that these coefficients are only computed once in the original UVLM as they only depend on the airfoil shape and not on its position (or the maneuver type). In the unsteady cases where the airfoil is prescribed to a certain motion, the right-hand side coefficients of equation (3.18) must be corrected as

$$\mathrm{RHS}_i = -(u_\infty - u_i) \cdot \vec{n_i}, \tag{3.19}$$

where u_i is the velocity of the collocation point i due to the airfoil motion on an inertial frame of reference and $\vec{n_i}$ is to normal vector on each panel.

As it has been discussed, the wake vortices are allowed to convect freely with local fluid velocity (Kirckhhoff velocity) to satisfy Helmholtz laws of vortex dynamics (Helmholtz, 1858; Saffman, 1992). To do so, in each iteration the position of a wake vortex i is updated as

$$\vec{r}_{Wi}(t_k) = \vec{r}_{Wi}(t_{k-1}) + u_{Wi}\Delta t \tag{3.20}$$

where Δt is the time increment at each time-step, $\vec{r}$ is the position vector of each vortex and

u_{Wi} is total computed velocity of each wake vortex computed by taking into account the freestream velocity and the induced velocities by the bound and other wake vortices as

$$u_{Wi} = u_\infty + \sum_{j=1}^{N} u_{ij} + \sum_{j=1, j\neq i}^{N_W} u_{ij}. \tag{3.21}$$

After obtaining all the circulations by solving the system equations (3.18), the pressure difference on each panel is given by the unsteady Bernoulli's equation written as

$$\Delta P_i = \rho U_\infty \frac{\Gamma_i}{d_i} + \rho \frac{\partial}{\partial t} \sum_{j=1}^{i} \Gamma_j, \tag{3.22}$$

and this pressure distribution is integrated to provide the lift force.

The proposed viscous extension of the UVLM via modification of the location of the control and collocation points on each panel is performed as follows. The influence coefficient A_{ij} remains a function of η for each time step obeying Equation (3.14); unlike the original UVLM where $\eta = 0.5$ for all the instances. The velocities induced by the new shed vortex in the wake and all the older ones on each panel remain a function of η and ξ that are updated at each time step as B_e is a function of time for the moving plates. To clarify more, for a pitching motion ($\alpha = \alpha(t)$), the instantaneous angle of the plate $\alpha(t)$ is used to find the value of B_e for updating the position of the collocation and control points. For a plunging motion ($y = h(t)$), the relative angle of attack serves as the instantaneous angle of attack $\alpha_s = \dot{h}(t)/U_\infty$ to calculate B_e.

3.5 Results

Based on the proposed viscous UVLM, three different cases are considered: the step response, the frequency (harmonic) response, and response due to an arbitrary time-varying input

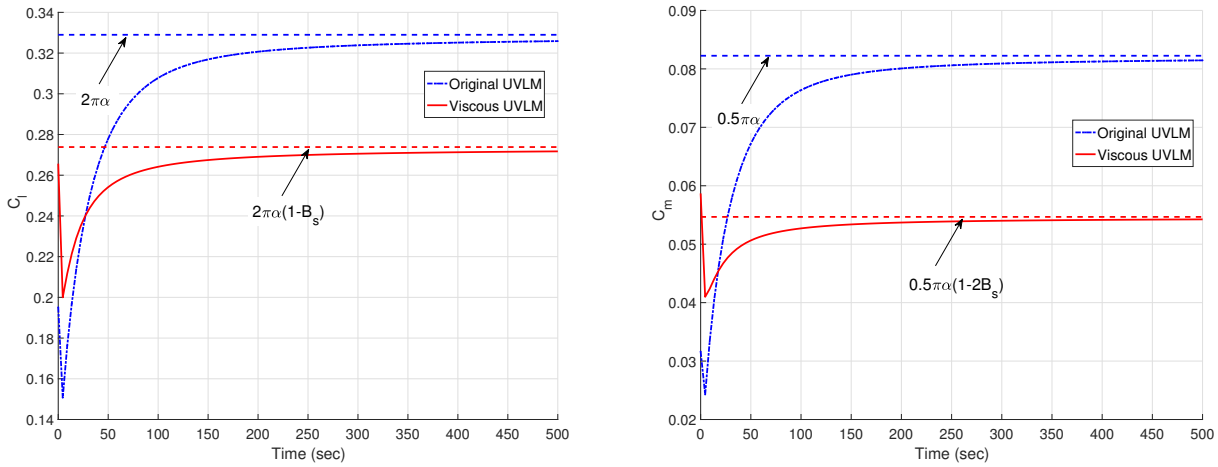

(a) (b)

Figure 3.3: Wagner (step) response at $Re = 10^4$ and $\alpha = 3°$: (a) Lift coefficient response and (b) moment coefficient response

(taken to be a multi-frequency harmonic signal). Figure 3.3 shows the lift and moment history of the foil subjected to a step change in the angle of attack (pitching angle). This is also known as the Wagner response. Even though the lift dynamics (evolution) are similar for both the original and modified (viscous) UVLM, they approach different asymptotes. Expectedly, the original UVLM approaches Kutta's potential flow values, while the modified UVLM approaches the viscous values given by equations (3.2) and (3.3), which are smaller than the Kutta's values as the viscous term B_s tend to decrease C_l and C_m. In fact, these results verify that the coupling between the UVLM and the viscous theory is correctly achieved.

Figure 3.4 shows the lift frequency response of a harmonically pitching airfoil. For more information on how to build a frequency response from an unsteady solver, the reader is referred to Rezaei & Taha (2017). The original UVLM matches perfectly with the Theodorsen inviscid results in both amplitude and phase of the lift frequency response (i.e. Theodorsen function). The modified UVLM is compared against the lift frequency response constructed from URANS computational simulations using $k - \omega$ SST turbulence model. The reader is referred to chapter 2 for more details about the setup in the computational fluid dynamics

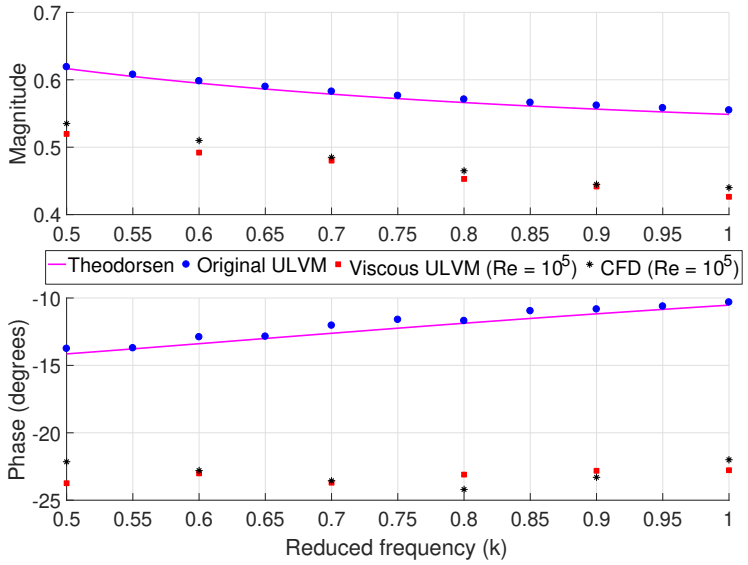

Figure 3.4: Comparing the frequency response of a pitching airfoil using different methods at $Re = 10^5$

(CFD) solver. The frequency response is constructed using a 3-degrees pitching amplitude for NACA 0012 at $Re = 10^5$. A very good agreement is observed between the modified UVLM and CFD results; both showing more phase lag and lower amplitude of the transfer function at a higher reduced frequency.

The lift history of the foil for a multi-frequency input in the form of $\alpha(t) = A\sin(\omega t) + 0.1A\sin(3\omega t)$ is plotted in Figure 3.5, where $A = 1^\circ$ and ω corresponds to a reduced frequency of $k = \frac{\omega c}{2V_\infty} = 1$, which is a relatively fast oscillation. The chord-based Reynolds number is set to be 10^5. Unlike the original UVLM which predicts higher peaks for the lift history, the modified UVLM matches the CFD results. In order to evaluate the local performance of the developed viscous UVLM, distribution of the pressure difference over the flat plate due to the same multi-frequency input at two critical instances during the maneuver is provided in Figure 3.6. The first instant is at the beginning of the upstroke motion when the geometric angle of the plate with respect to free stream is zero ($\alpha = 0$) but the relative velocity is maximum ($\dot{\alpha}_{max}$). The second instant is when the geometric angle of the plate with respect to free stream is maximum (α_max) but the plate relative velocity is zero ($\dot{\alpha} = 0$).

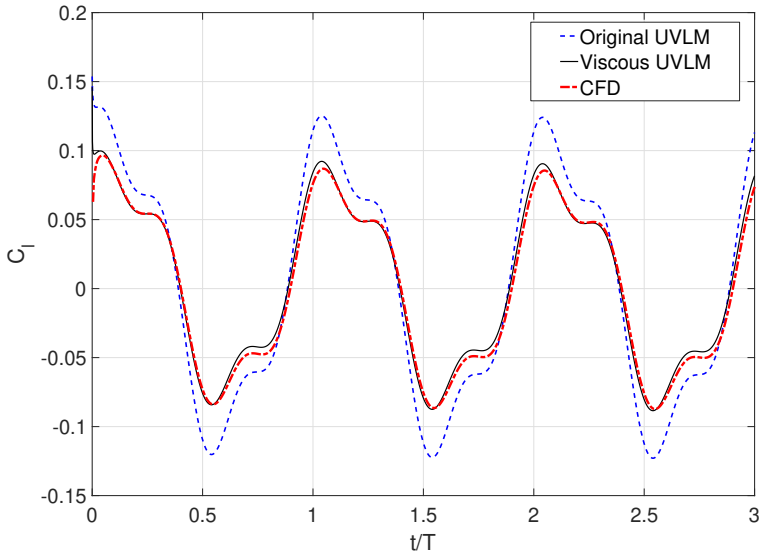

Figure 3.5: Comparison of the lift history from the original UVLM, viscous UVLM, and computational simulation due to a generic multi-frequency input $\alpha(t) = A\sin(\omega t) + 0.1A\sin(3\omega t)$ with $A = 1^\circ$ at $Re = 10^5$

A remarkable agreement is observed between the CFD results and the viscous UVLM in both cases in Figure 3.6. The main enhancement is observed near the TE region where the original UVLM over-predicts the value of the pressure by generating high-strength vortices near the TE due to Kutta condition. By considering the viscous effects in the developed viscous UVLM, this issue is addressed. Furthermore, the wake structure of the original and developed viscous UVLM due to the same input is shown in Figure 3.7. A significant difference is seen in the peaks and valleys. The figure shows a more damped wake activity in the viscous solution, which is physically intuitive.

3.6 Discussion

The ultimate purpose of this effort is to incorporate the viscous edge condition in the UVLM. Similar to the viscous theory (chapter 2), the viscous extension of UVLM was developed by tackling the Kutta condition and replacing it by a viscous condition from the triple-deck theory, described in the above sections. The author also tried two other intuitive methods

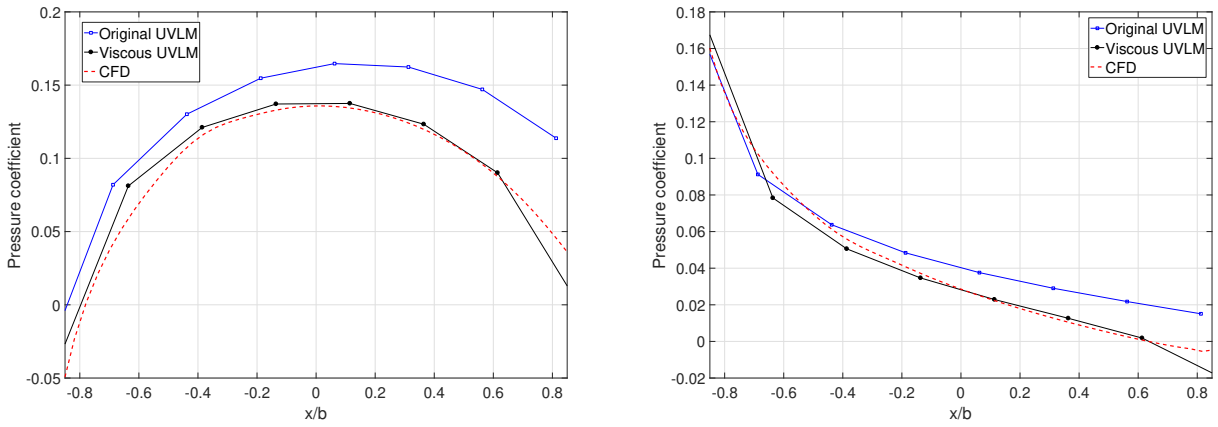

Figure 3.6: Comparison of the pressure distribution over the flat plate from the original UVLM, viscous UVLM and computational simulation due to a generic multi-frequency input $\alpha(t) = A\sin(\omega t) + 0.1A\sin(3\omega t)$ with $A = 1^\circ$ at $Re = 10^5$ and (a) $\alpha = 0$, $\dot{\alpha}_{max}$ and (b) α_{max}, $\dot{\alpha} = 0$

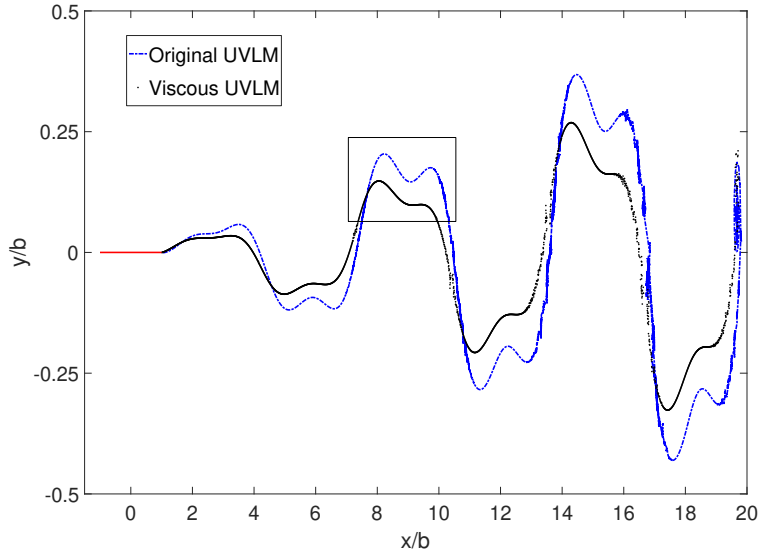

Figure 3.7: Comparing the wake structure of the original and viscous UVLM due to a generic multi-frequency input $\alpha(t) = A\sin(\omega t) + 0.1A\sin(3\omega t)$ at $Re = 10^5$ and $A = 1^\circ$

to accommodate the viscous condition in the UVLM, which could potentially be an easier approach compared to replacing the Kutta condition, yet, did not lead to useful results. Therefore, it may be prudent to report the failure of these other intuitive approaches.

First, by realizing that the new TE singularity B_s in Equation (3.1) can be related to an additional viscous circulation Γ_v as $B_e = U_\infty \Gamma_v/(2\pi b)$, it was attempted to modify the Kelvins's equation by adding the Γ_v to the right hand side of Equation (1.5) account for the effect of the viscous term Γ_v. Based on this idea, the generated wake circulation is updated at each time step, which not only modifies the strength of the shed vortices, but also changes the wake shape. In this case, the resulting aerodynamic load deviates significantly from the CFD or analytical results. In the second trial, the effect of new viscous condition was interpreted as a modification to the free stream angle of attack based on the fact that the singularity emerging from relaxing the Kutta condition can be seen as a change in the stagnation point angle in the cylinder domain (see the discussion after equations (3.2) and (3.3)). Since the angle of the rear stagnation point in the cylinder domain can be varied with the angle of the free stream velocity α_s and the conformal map from the cylinder domain to the plate domain preserves the angles, this new angle α_v given by $\alpha_v = \Gamma_v/2U_\infty = 2\pi B_e/U^2$ was subtracted from α_s in the UVLM (in the plate domain). Again, the results were not satisfying based on this approach. Therefore, the attempts to modify other conditions in UVLM rather than the Kutta condition to accommodate the viscous correction did not work properly.

3.7 Conclusion

The unsteady vortex lattice method was developed in the 1950s based on the potential flow formulation, Kutta condition and Kelvin's conservation of circulation. UVLM does not explicitly account for viscous effects, although it possesses some flavor of viscosity through Kutta (similar to almost all of the potential flow-based models). Exploiting the Hilbert

matrices algebra, it is shown how the Kutta condition is implicitly applied in the UVLM by dictating the location of the collocation and control point on each panel. Then, it is discussed that the relaxation of Kutta condition introduces an integrable singularity in the potential flow solution, which cannot be determined from the potential flow framework. In fact,the Kutta condition assumes this singularity to be zero. To obtain the strength of the singularity, the analytical triple-deck boundary layer theory, developed in 1970s, is employed and the corrections to the lift and moment coefficients are provided. The strength of the singularity is Reynolds number and angle of attack dependent. By incorporating the viscous corrections of the lift and moment in the UVLM through Hilbert matrix algebra, the viscous extension of the UVLM is developed. It is shown that the panel mesh is updated at each time step based on the airfoil motion and Reynolds number. The performance of the viscous UVLM is compared against the original UVLM and CFD results. To this end, three different cases are studied. First, the lift history of a flat plate subjected to the step input is provided that demonstrates the correctness of the coupling between UVLM and viscous theory as the lift and moment coefficients reach to the value predicted by the viscous theory. Second, the comparison of the frequency response is provided, which shows a very good agreement with the CFD results. Lastly, a multi-frequency input is used as the plate motion and the results are compared in term of lift history, pressure distribution and wake structure. A remarkable enhancement is observed in the viscous UVLM compared to the original UVLM when comparing against CFD results.

Chapter 4

Nonlinear Effects of Laminar-to-Turbulent Transition on Lift Dynamics

4.1 Background

There are many recent applications in aeronautical engineering that operate in the low-to-moderate Reynolds number regime, such as high-altitude flying ships (Greer *et al.*, 2000) or unmanned-aerial-vehicles and micro-air-vehicles (Mueller & DeLaurier, 2003; Taha *et al.*, 2012). These vehicles typically operate at low speeds and possess short characteristic length scales, necessitating more research to obtain a deeper understanding of the low-to-moderate Reynolds number aerodynamics for various configurations. The corresponding Reynolds number for these applications ranges from $10^4 - 10^5$, at which laminar-to-turbulent transition is prone to happen (Pelletier & Mueller, 2000; McMasters & Henderson, 1980). In general, the airfoils operating at low-to-moderate Reynolds numbers, $\sim O(10^5)$, are vulnerable to

laminar boundary layer separation and transition that have either adverse or uncommon effects on the aerodynamic performance.

A large body of publications have investigated the transition phenomenon in steady aerodynamics for a wide range of Reynolds numbers (Narasimha, 1985; Yarusevych *et al.*, 2009; McAuliffe & Yaras, 2010; Boutilier & Yarusevych, 2012; Hosseini *et al.*, 2016); several studies have discussed the unsteady effects on transition (Lee & Basu, 1998; Lian & Shyy, 2007; Garmann & Visbal, 2011; Kim & Chang, 2014; Raffel *et al.*, 2015; Liu *et al.*, 2018; Benton & Visbal, 2019). From a fluid dynamics perspective, the subject of unsteady aerodynamics of moving airfoils can be divided into attached (typically small deflections) and separated (typically large deflections) flows on the body. The latter is mainly known as the light or deep (dynamic) stall, which is encountered in helicopters, turbines and compressors where the blades experience high incident angles beyond the linear region of the flow (Xia & Mohseni, 2013; Zakaria *et al.*, 2017; Santos & Marques, 2018; Gupta & Ansell, 2018; Benton & Visbal, 2019; Deparday & Mulleners, 2019). However, the focus of this chapter is on the former case (small deflections). The previous efforts in this direction (McCroskey & Puccif, 1982; Dowell *et al.*, 1983; Dovgal *et al.*, 1994; Lee & Basu, 1998; Yarusevych *et al.*, 2009; Poels *et al.*, 2015; Kurtulus, 2018) have mostly studied the temporal-spatial growth or decay of different types of instabilities and mechanisms triggering the transition onset, which are enhanced at lower Reynolds numbers. Some articles have focused on the influence of transition on the flutter analysis (Lorber & Carta, 1994; Poirel & Mendes, 2014). There are several factors, such as Reynolds number, surface roughness, free stream properties, geometry and airfoil kinematics (Arena & Mueller, 1980; Lian & Shyy, 2007), that can affect the transition process. It has been shown that laminar separation is followed by instabilities which in many cases eventually lead to laminar-to-turbulent transition (Smith, 1986; Dovgal *et al.*, 1994). Depending on the values of the Reynolds number, angle of attack, free stream turbulent intensity, airfoil thickness, etc, the separated flow may reattach shortly after departure, forming a laminar separation bubble (LSB).

When the Reynolds number is moderate, transition is usually accompanied by a slight separation forward to the trailing-edge even at small angles of attack as the initial laminar boundary layer is not strong enough to overcome the downstream adverse pressure gradient. The reattachment is typically turbulent and may persist to the trailing-edge station. It should be noted that if the Reynolds number is very high, LSB is not created and the flow remains attached on the entire length of the airfoil while transition is happening at some location on the airfoil. (Richter *et al.*, 2014)

As discussed by Poirel & Mendes (2014) and Negi *et al.* (2018), transition significantly influences the aerodynamic characteristics of the airfoil and often introduces non-linearities in the response. Therefore, the transition effect on the dynamics of circulation and force generation is of particular importance for preliminary design purposes where the aerodynamic forces are the main concern. Kim & Chang (2014) experimentally investigated the effect of transition at low to moderate Reynolds numbers ($2 \times 10^4 - 5 \times 10^4$) on a pitching airfoil. Utilizing pneumatic tubing for the pressure measurements and flow visualization, they reported the time history of the aerodynamic forces and flow behavior near the trailing-edge. They characterized the transition from the pressure drop on the suction side of the airfoil and showed that the transition point moves toward the leading edge as either angle of attack or Reynolds number increases. Furthermore, it can be seen from their results that the aerodynamic loads reveal non-linear behavior. Raffel *et al.* (2015) utilized the Differential Infrared Thermography (DIT) to measure the onset and end of the transition location of a pitching NACA 0012 at $Re = 1 \times 10^6$. Later, Liu *et al.* (2018) validated their three-equation transition model with the experimental results of Raffel *et al.* (2015) and concluded that the transition location of a pitching airfoil possesses a non-trivial frequency response.

It is a very common goal to develop simple and sufficiently accurate aerodynamic models that can be utilized for analyses and design. Almost all of the classical efficient tools, whether analytical (e.g. Theodorsen (Theodorsen, 1935) and Wagner (Wagner, 1925)) or numerical

(e.g. unsteady vortex lattice method:UVLM (Hedman, 1966)), originated from the linear potential flow theory (valid for high Reynolds number flows). In these approaches, the effect of viscosity is taken into account solely through the auxiliary condition at the sharp edges, which determines the rate of vorticity shed from the boundary layer to the wake and dictates the amount of circulation (or lift) on the airfoil as discussed in chapter 2. The most utilized condition is the well-known Kutta condition, which assumes smooth flow off the trailing-edge (TE), and has been discussed in detail by Sears (1976*a*) and Crighton (1985), and recently by Xia & Mohseni (2017) and in chapter 2 of the present dissertation. The classical Kutta condition neglects any uncommon effects that might happen in the vicinity of the trailing-edge or inside the boundary layer (e.g. flow around the trailing-edge or non-linear effects from transition). As a result, the classical models based on potential flow cannot predict transition effects on the resulting aerodynamic loads in the low-to-moderate range of Reynolds numbers. While this fact is well-known to aerodynamicists, what these models exactly lack to better capture transition effects is less known. In other words, how can one augment potential flow models with high-fidelaty simulation data to account for transition effects on the lift dynamics in a simple way? The current effort provides an answer to this question.

The objective of this work is to investigate the non-linear effects of transition on the lift and circulation dynamics of a pitching airfoil at low-to-moderate Reynolds number. By deriving the exact version of the hypothesized Kutta condition, we show the contribution of the pressure gradient across the boundary layer in the presence of transition (and LSB), which was neglected in the classical Kutta condition. To this end, the unsteady incompressible Reynolds-averaged Navier-Stokes equations have been numerically solved. The finite-volume computational fluid dynamics (CFD) solver ANSYS Fluent 18.2 has been employed using the $\gamma - Re_\theta$ (or transition-SST) closure model by Langtry and Menter (Langtry & Menter, 2009), which showed satisfactory results in transition prediction for aerodynamic applications including complex cases involving dynamic stall (Wang *et al.*, 2010; Gharali & Johnson,

2013). In this study, the considered pitching amplitudes are far below the dynamic stall, and the oscillation reduced frequencies are low. Therefore, the SST transition model is a good candidate for this study. The numerical setup is explained in Sec 4.2. Validation against an experimental study by Kim & Chang (2014) on a pitching airfoil at a moderate Reynolds number where transition occurs is presented in Sec 4.3. Note that the numerical setup and validation sections follow the recent paper (Rezaei & Taha, 2019) and are presented here with more details for completeness. Lastly, in Sec 4.4, the effect of different parameters such as Reynolds number, pitching amplitude and reduced frequency on the circulation dynamic is studied, and a connection is drawn between transition and the rate of circulation development (equivalently the rate of vorticity shed at the sharp edge). Based on this connection, extension of the classical unsteady approaches can be performed to account for the non-linear lift dynamics in the transition regime by modifying the edge condition (i.e., the Kutta condition).

4.2 Numerical setup

The farfield unstructured mesh and the conformal grid resolution near the airfoil is shown in Figure 4.1. This hybrid mesh comprises a very dense structured mesh near the airfoil, which contains the boundary layer in all the studied cases, followed by an unstructured mesh, which facilitates the dynamic mesh approach. The O-type farfield has been used and divided into three rings where the intermediate ring (red) accommodates the airfoil motion via a dynamic mesh, the inner ring (blue) moves with the airfoil like a rigid body, and the outer ring (green) is fixed. This technique maintains the generated high quality grid near the airfoil described below as no deformation or remeshing occurs in the inner ring. The geometry and methodology are almost identical to that in Taha & Rezaei (2018) except for two changes. The first alteration is the addition of grid layers inside the boundary layer to guarantee

that the $y^+ < 1$. Also, a coarser mesh was also generated for grid independence study and similar results were observed. However, the denser mesh was chosen for the rest of the study since the computational time was not a big concern and to be conservative. This high grid resolution helps to better capture the events inside the boundary layer and the flow field near the trailing-edge, which requires capturing the edge of the boundary layer and finding the vorticity fluxes into the wake as proposed by Sears (1976*a*) and demonstrated below. The high-performance computer (HPC) at the University of California, Irvine, was utilized for all the simulations with 32 CPUs in parallel, where the clock speed of the processors was 2.2 GHz. The total simulation time for running 4 complete pitching cycles of the airfoil was almost 15 hours. (For more details about the grid topology, dynamic mesh and solution setup in the solver, the reader is referred to chapter 2)

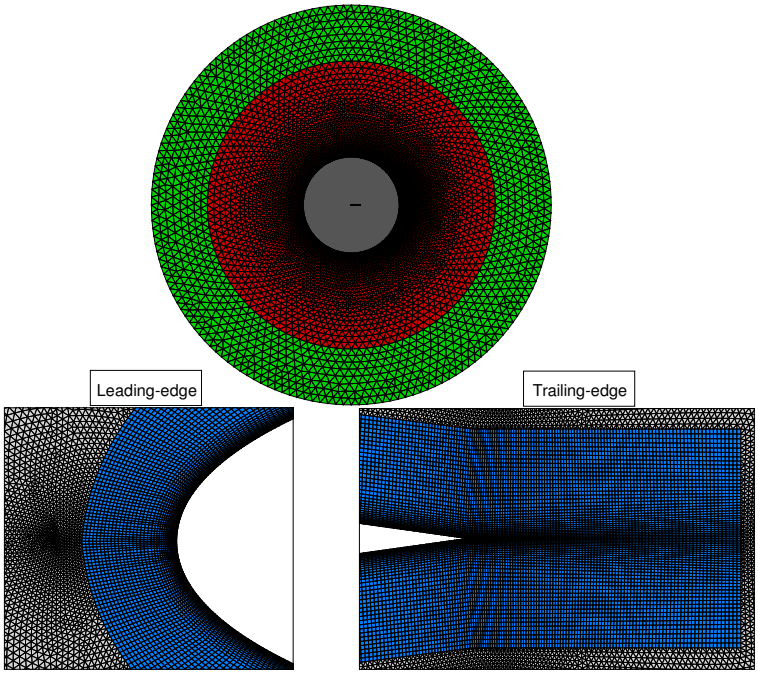

Figure 4.1: Mesh topology in the farfield (top picture) and near the leading edge and trailing-edge (bottom pictures) of the airfoil. The blue region near the airfoil constitutes of high resolution structured grids that contains the boundary layer and the gray region is made of unstructured triangular elements.

The second difference is employing the local correlation-based $\gamma - Re_\theta$ transition model (Menter *et al.*, 2006) which is compatible with the unstructured mesh. It involves two

transport equations for the intermittency, γ, and the transition onset momentum thickness Reynolds number, $\hat{Re}_{\theta t}$, as follows:

$$\frac{\partial(\rho\gamma)}{\partial t} + \nabla \cdot (\rho\gamma \boldsymbol{U}) = P_\gamma - E_\gamma + \nabla \cdot \left((\mu + \frac{\mu_t}{\sigma_f}) \nabla(\gamma) \right) \tag{4.1a}$$

$$\frac{\partial \left(\rho \hat{Re}_{\theta t} \right)}{\partial t} + \nabla \cdot (\rho \hat{Re}_{\theta t} \boldsymbol{U}) = P_{\theta t} + \nabla \cdot \left(\sigma_{\theta t} (\mu + \mu_t) \nabla(\hat{Re}_{\theta t}) \right), \tag{4.1b}$$

where σ_f and $\sigma_{\theta t}$ are the model constants that are set to 1 and 2, respectively. The two source terms, P_γ and E_γ, in the right hand side of Equation (4.1a) are responsible for the transition onset and destruction/relaminarization, respectively. The production term $P_{\theta t}$ in Equation (4.1b) adjusts the value of the transition onset momentum thickness Reynolds number to match the value obtained from the empirical correlations (equations 35 and 36 in the paper by Langtry & Menter (2009)) outside the boundary layer, and vanishes inside the boundary layer. These transport equations are discretized with second order upwind method and calculated at each cell. The intermittency equation initiates the transition by affecting the turbulent kinetic energy (TKE) production downstream of the transition point.

Unlike typical transition models that suffer from non-local calculations, by utilizing the vorticity Reynolds number ($Re_v = \frac{\mu y^2}{\rho} |\frac{\partial U}{\partial y}|$ where y is again the distance from the nearest wall), the $\gamma - Re_\theta$ transition model correlates the transition onset with the local boundary-layer quantities through empirical relations. Since Re_v can be calculated locally, this model has the advantage that can be easily implemented into RANS equations. Aside from all the local calculations and correlations in the γ-equation to treat transition, the non-local events outside the boundary layer, such as free stream TKE decay and pressure gradient, impact the transition process by altering the turbulent intensity. In fact, these non-local effects form the basis of the empirical-based models of transition (Abu-Ghannam & Shaw, 1980). The momentum thickness Reynolds number, which is an important part of this model, is devised to handle these non-local effects on the transition onset by manipulating

the source term in the intermittency equation. These equations interact with the $k-\omega$ SST model by modifying some of the source terms in the $k-$equation (Fluent, 2009), while the $\omega-$equation remains intact. Unlike the turbulence models, which were devised to model the physics of turbulence to some extent (e.g. the turbulent kinetic energy equation is derived from the time-averaged Navier-Stokes equations), the provided transport equations for γ and $\hat{Re}_{\theta t}$ do not exactly model the transition physics as pointed out by Langtry & Menter (2009), yet contain the parameters (correlations) that have been proved to play a vital role in transition process due to different mechanisms and possess sufficient accuracy at lease under the conditions studied in this dissertation (see the validation section). The added transport equations require boundary conditions on the airfoil surface, inlet and outlet. On the no-slip wall (aifoil) and constant pressure outlet, zero normal flux condition is prescribed for γ and Re_θ. At the inlet station, γ is set to 1 and Re_θ is to be found from empirical correlations in the model based on the inlet turbulent intensity. These correlations are provided in equations 35 to 38 in (Langtry & Menter, 2009).

4.3 Validation

The numerical setup is validated against the experimental results of Kim & Chang (2014) who studied the boundary layer events at moderate Reynolds numbers. The corresponding case that is chosen for validation is a NACA 0012 airfoil pitching around the quarter chord point with a zero mean angle of attack and 6 degrees pitching amplitude. The reduced frequency is $k = 0.1$, Reynolds number is $Re = 48 \times 10^3$, and the free stream turbulent intensity reported in the paper is $TI < 0.4\%$, so we set $TI = 0.35\%$ for our numerical simulation. Under these conditions, the flow experiences transition which magnifies as the Reynolds number decreases (Kim & Chang, 2010). From computational side, modeling transition in unsteady flows has been always a challenge due to the difficulty in predicting the transition point on

the dynamically moving surface.

Figure 4.2 shows a comparison between the experimental results of Kim & Chang (2014) and our numerical results, which shows a good agreement in the lift history. It should be noted that the SST transition model shows dissipative behavior for $Re < 70 \times 10^3$ based on our simulations. The ripples seen in Figure 4.2 for the curve of $Re = 48 \times 10^3$ occur near the instants of maximum pitching velocity where the flow is more prone to separation. At these instants, the interaction between the laminar separation bubble and downstream adverse pressure gradient is significant, and the model is unable to find the correct transition point. That is the reason why $Re = 75 \times 10^3$ has also been used for the validation with the experiment.

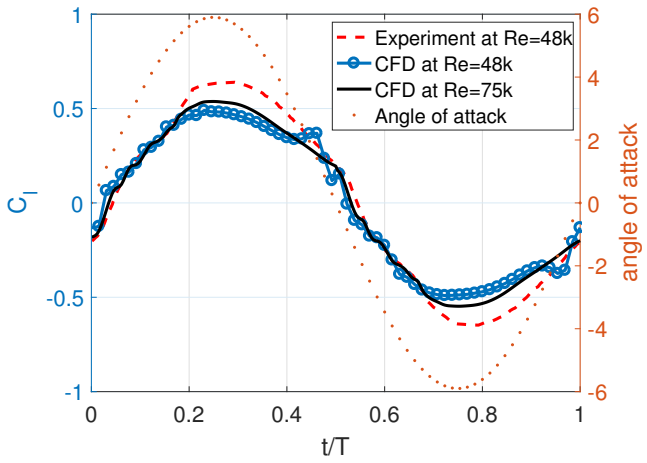

Figure 4.2: Validation of the computational setup adopted from (Rezaei & Taha, 2019). Comparison between the lift history from CFD and the experimental study (Kim & Chang, 2014) for a pitching NACA 0012 with $\alpha(t) = 6^\circ \sin(\omega t)$ and $k = 0.1$ undergoing transition.

The discrepancy in the maximum lift coefficient may actually be attributed to the experimental results per se. The maximum lift coefficient in the experimental data is almost equal to the one obtained from thin airfoil theory: $2\pi(6^\circ \times \frac{\pi}{180}) = 0.66$, which is not expected because (i) an actual airfoil has a lift curve slope that is smaller than the theoretical value of 2π, and (ii) the amplitude of the unsteady lift must be attenuated due to wake effects:

Theodorsen lift deficiency (Theodorsen, 1935).

To validate the local flow details and the transition point dynamics, we consider the pressure coefficient C_p at three important instances, i.e. two instances ($\alpha_u = 5, 6$) in the upstroke near stroke reversal and one instance ($\alpha_d = 3$) in the downstroke, as shown in Figure 4.3. As described by Arena & Mueller (1980) and recently by Boutilier & Yarusevych (2012), the start of the short plateau in the mid-chord region corresponds to the laminar separation, followed by a sudden drop indicating the transition point. Then the pressure recovery region is attributed to turbulent reattachment. A good agreement is observed in terms of the magnitude of the pressure coefficient and transition point. The reason for slightly higher values of C_p in the experimental results compared to CFD is the same as the above explanation for C_l difference near the stroke reversal. The $\alpha_d = 3$ case corresponds to the instant where the airfoil is at the three-quarter of the downstroke motion where more complicated flow events are expected due to the interaction with the vortical region formed in the upstroke near the trailing-edge. Under this condition, the transition point obtained from the CFD results is delayed roughly 10 percent.

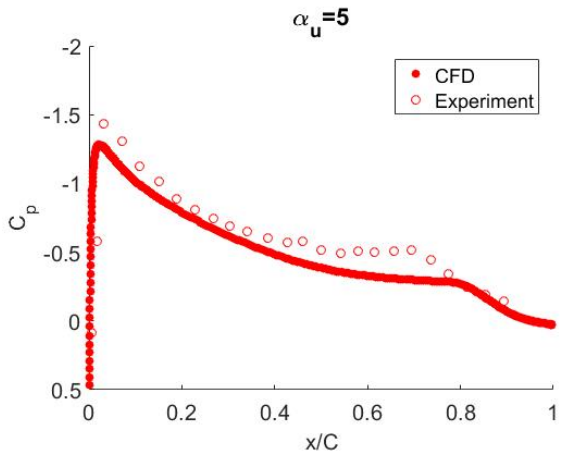

(a) +5 degrees upstroke

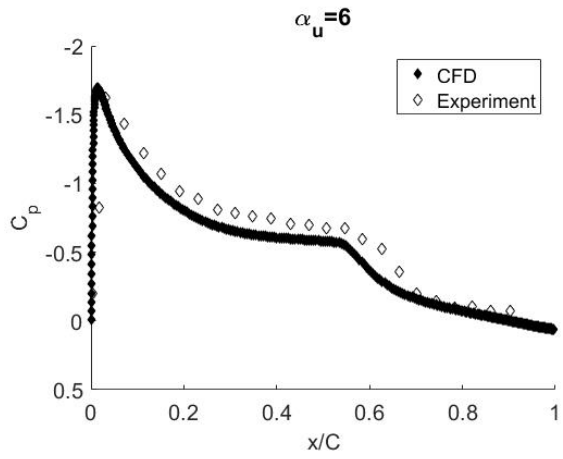

(b) +6 degrees upstroke

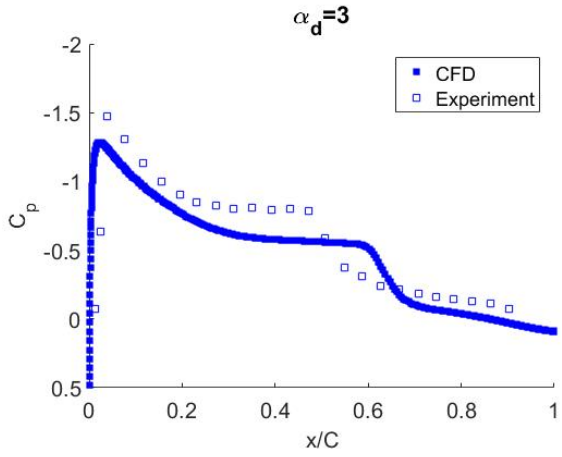

(c) +3 degrees downstroke

Figure 4.3: Comparison of the pressure coefficient on the suction side between the CFD results and experiment

Figure 4.4 indicates the flow field near the trailing edge at different instants during the cycle. As it is addressed by Kim & Chang (2014), a mushroom structure is clearly seen in figure 4.4a when $\alpha_u = +3$ which is the consequence of the interaction between two consecutive produced vortices at the trailing edge. The growth of the third vortex at the trailing edge (Figure 4.4b) tends to disrupt the mushroom structure followed by a big vortical region on the suction side (Figure 4.4c). The same scenario happens when the new LEV starts to form (Figures 4.4d, 4.4e & 4.4f).

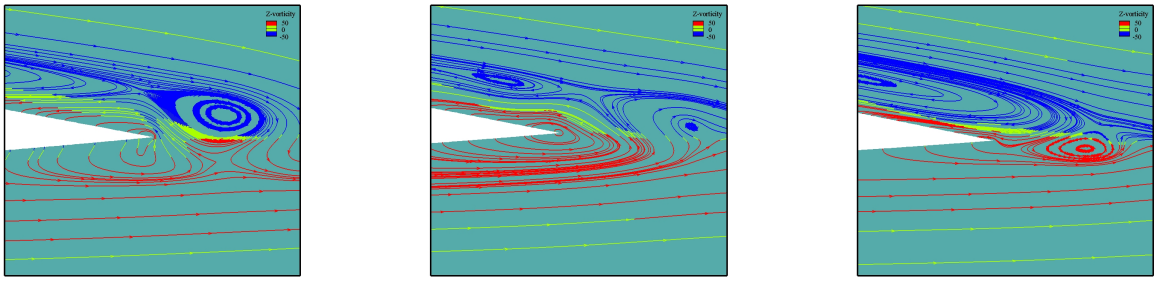

(a) $\alpha_u = +3$ (b) $\alpha_u = +3.3$ (c) $\alpha_u = +3.9$

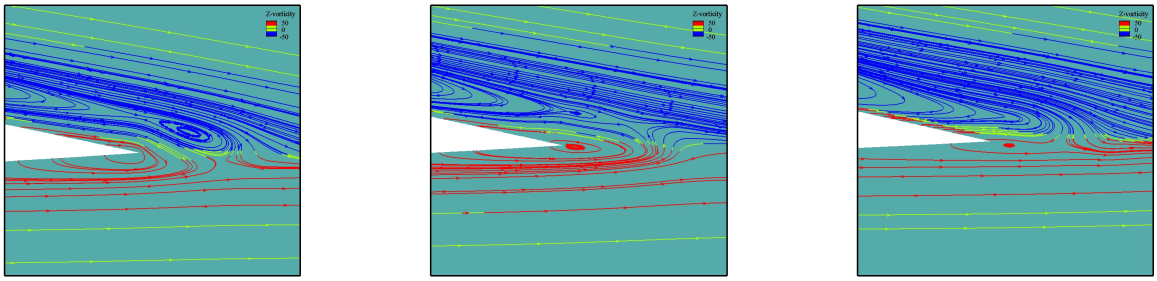

(d) $\alpha_u = +4.2$ (e) $\alpha_u = +4.6$ (f) $\alpha_u = +5$

Figure 4.4: Flow visualization near the trailing edge of the pitching airfoil colored with the Z-vorticity

4.4 Results

4.4.1 Effect of Transition on the Lift Dynamics

CFD simulations have been carried out in the range of moderate Reynolds number, $Re = 75 \times 10^3 - 400 \times 10^3$ and motion reduced frequency $k = 0.1$ to investigate the effect of transition on the lift dynamics of a pitching airfoil at zero mean angle of attack with 3 degrees pitching amplitude. As shown in our preliminary analysis (Rezaei & Taha, 2019), it should be emphasized that in this regime, the effect of transition on the lift dynamics

is significant. That is, if transition is not taken into account or properly modeled, the computed aerodynamic loads will be noticeably different. Based on Figure 4.5a, assuming a fully turbulent flow without modeling the transition, using a single harmonic motion as an input for the pitching airfoil (time-varying angle of attack) results in a harmonic lift response at the same frequency (i.e., linear dynamics). However, at the same Reynolds number, the same input results in a different lift dynamics when transition is considered. In fact, in the presence of transition, the dynamics of the flow is no longer linear as the output (lift) possesses higher harmonics compared to the single-harmonic input (angle of attack), which will be the focus of the coming sections. For better comparison, the Theodorsen results at $k = 0.1$ is also plotted, which matches the linear results of the fully turbulent case. To put in a nutshell, a fully turbulent flow results in a linear lift dynamics whereas laminar-to-turbulent transition induces non-linearity in the lift dynamics.

This criterion can be used as an indicator for transition. To further investigate this point, the effect of Reynolds number on the lift history is shown in figure 4.5b. It can be seen that increasing the Reynolds number makes the output signal (lift) to resemble more a pure sinusoid. It is found that, under the conditions used in this study, the lift dynamics becomes very close to the fully turbulent case for $Re > 400 \times 10^3$, and below this value, careful consideration is required to capture the transition, specifically when $Re < 200 \times 10^3$ where transition effects are significant.

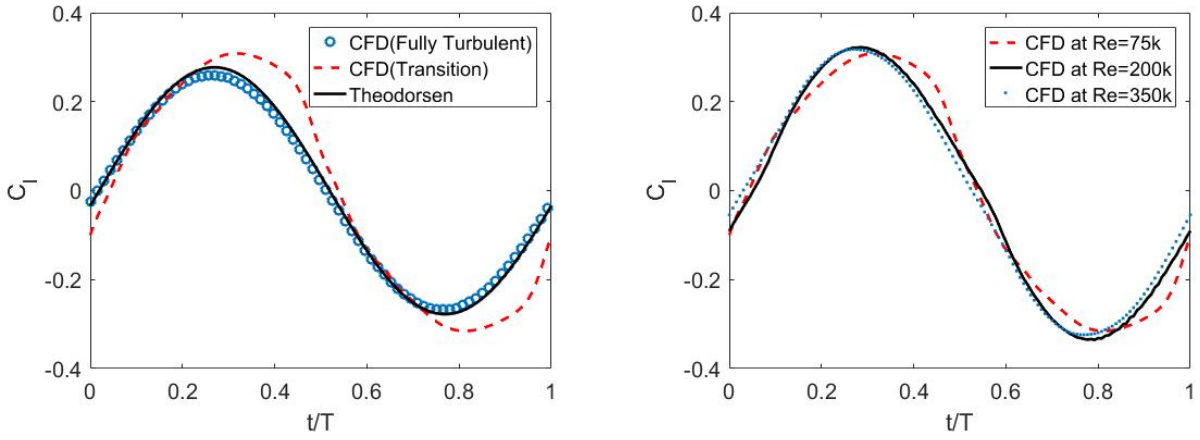

(a) (b)

Figure 4.5: Lift history of a pitching NACA 0012 with $\alpha(t) = 3^\circ \sin(\omega t)$ and $k = 0.1$ undergoing transition: (a) Comparison of the lift history between Theodorsen model and CFD results at $Re = 75 \times 10^3$ using transition and fully turbulent models and (b) Effect of Reynolds number on the lift history utilizing transition model in CFD.

Figure 4.6 shows the flow field for three cases where in the first two cases, the transition is assumed to occur in the flow field and in the third one is fully turbulent. It can be seen that at lower Reynolds number, two vortical regions exist at the top and bottom, and they disappear as the Reynolds number increases. When the Reynolds number is high, the transition and fully turbulent cases are similar and that is the reason that the lift history of the cases is also identical.

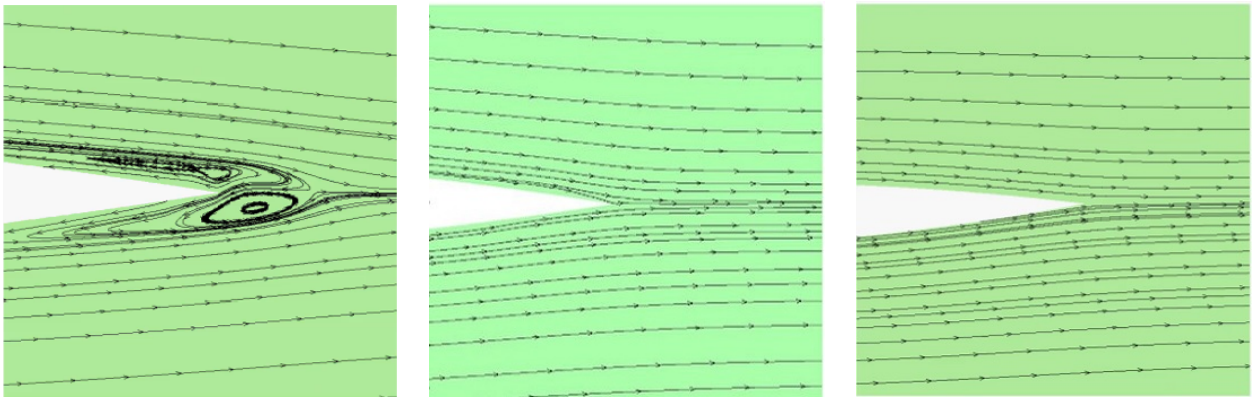

(a) (b) (c)

Figure 4.6: Streamlines near the trailing edge at $\alpha_u = 0$ at: (a) $Re = 7.5 \times 10^4$ using transition model (b) $Re = 35 \times 10^4$ using transition model and (c) $Re = 35 \times 10^4$ using fully turbulent model

4.4.2 Flow near the trailing-edge and the Kutta condition

Potential flow theory is indeed a milestone in the history of aerodynamics, forming the basis of almost all the analytical theories in steady and unsteady aerodynamics. It states that for a thin airfoil subjected to small deflections at high Reynolds numbers, the flow can be assumed everywhere irrotational except for a thin layer around the airfoil (boundary layer) and in the wake (only appears in the unsteady theories). These regions are modeled with sheets of (or point) vortices whose strength is determined from the kinematic boundary condition on the airfoil (no-penetration). Laboring this algorithm, a unique solution cannot be determined unless the value of the circulation is known. Therewith the Kutta condition comes to play, which dictates vanishing circulation distribution at the trailing-edge (zero loading at the trailing-edge) based on physical observations from the flow field around the airfoil trailing-edge. This condition forms the bridge that connects potential flow to viscous flow and essentially relates the amount of generated vorticity flux in the boundary layer to the vorticity in the wake (Sears, 1976*a*). In the potential flow framework, there are many representations of the Kutta condition; one dictates zero loading at the trailing-edge, which

is stated as

$$\lim_{y\to 0^+} P(\mathrm{TE}, y) = \lim_{y\to 0^-} P(\mathrm{TE}, y), \tag{4.2}$$

where $P(\mathrm{TE}, y)$ represents the pressure at the trailing-edge (TE) station at a distance y above the trailing-edge point; that is the trailing-edge is approached from the top by taking the limits as $y \to 0^+$ and from the bottom as $y \to 0^-$. In the corresponding viscous flow accompanied by the boundary layer development on the top and bottom surfaces, this condition means equal pressure at the edges of the boundary layers on each side, which is indeed generally true. Nevertheless, under certain conditions such as low Reynolds number flows, high frequency motion of the airfoil and laminar-to-turbulent transition, deviation is observed from the classical Kutta condition as shown in chapters 2 and 3. To elaborate more, consider the viscous flow around an airfoil and regard the flow near the trailing-edge, shown in Figure 4.7. Since the potential flow pressure distribution over the thin airfoil represents the pressure distribution at the edge of the boundary layer in the viscous flow, Equation (4.2) applied within the potential flow solver, yields $P_1 = P_2$ in the presence of boundary layers, where the points 1 and 2 lie on the edge of the boundary layer at the trailing-edge station (Figure 4.7).

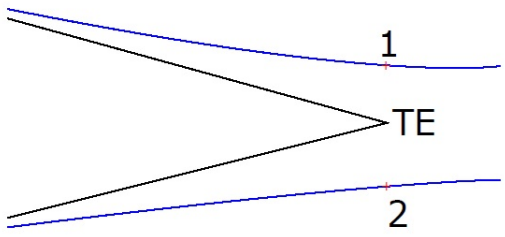

Figure 4.7: A zoom at the trailing-edge and its boundary layer. The blue lines represent the edge of the boundary layers and the red dots (points 1 and 2) represent the edge of the boundary layers at the trailing-edge station.

In the second chapter, we have shown while the main assumption underpinning Prandtl's

boundary layer theory (pressure is constant along a direction perpendicular to the surface inside the boundary layer thickness) is valid over the majority of the airfoil length, it may not be valid in the immediate vicinity of the trailing-edge. The situation is exacerbated when laminar-to-turbulent transition occurs. That is, there may be a considerable pressure rise ΔP across the boundary layer. In this case, the physical condition (4.2) results implies

$$P_1 - \Delta P_1 = P_2 - \Delta P_2, \tag{4.3}$$

In addition, the unsteady Bernoulli's equation provides a relation between P_1 and P_2 (note that point 1 and 2 lie on the edge of the boundary layer) as:

$$\frac{P_1}{\rho} + \frac{1}{2}V_1^2 + \frac{\partial \phi_1}{\partial t} = \frac{P_2}{\rho} + \frac{1}{2}V_2^2 + \frac{\partial \phi_2}{\partial t}, \tag{4.4}$$

where V is the potential flow velocity at the edge of the boundary layer and ϕ is the corresponding velocity potential. Combining Eqs.(4.3) and (4.4) and realizing that $\phi_1 - \phi_2 = \Gamma$, we obtain

$$\dot{\Gamma} = \frac{1}{2}\left(V_2^2 - V_1^2\right) + \frac{\Delta P_2 - \Delta P_1}{\rho}, \tag{4.5}$$

To recover the common form of the Kutta condition typically applied in the classical theory of unsteady aerodynamics, we set $\Delta P_1 = \Delta P_2 = 0$ and $V_{1,2} = U \pm \frac{1}{2}\gamma_{\mathrm{TE}}$. In this case, Equation (4.5) results in

$$\dot{\Gamma}_{\mathrm{Kutta}}(t) = -U_\infty \gamma_{\mathrm{TE}}(t), \tag{4.6}$$

where γ_{TE} is the circulation distribution at the trailing-edge (instantaneous strength of the shed vortex sheet per unit length at the shedding time) calculated as

$$\gamma_{TE}(t) = V_2 - V_1, \tag{4.7}$$

Thus, the *exact* circulation dynamics governed by Equation (4.5) reduces to the classical Kutta's circulation governed by Equation (4.6) using two assumptions: linearization of the first term (velocity-term) and neglecting the second term due to pressure differences across the boundary layers. The former assumption is quite accurate for small deflections (small α). In this work, we show that the transition effects on the lift dynamics are related to (can be captured by) the pressure term in the circulation dynamics Equation (4.5).

Transition induces non-linearity in the lift dynamics. Since lift is ultimately dictated by the Kutta condition, one can legitimately deduce that the classical Kutta condition is violated, and special care is required to study the flow near the trailing-edge. It is worth noting that unlike the steady boundary layer where the flow reversal corresponds to zero shear stress at the wall (defining the separation phenomenon), in the unsteady case, zero shear stress (or flow reversal) is not an indication of boundary layer separation. In other words, the boundary layer assumptions may remain correct while flow reversal is observed inside it. In fact, separation might happen far downstream of the point of zero shear stress in unsteady flows. Finding a mathematical condition that define the boundary layer separation in unsteady flows has been a challenge over decades for scholars. However, it is known that upon separation, wake is commenced and the boundary layer breaks up and its definition is no longer valid (Sears & Telionis, 1975). Likewise, complicated boundary layer events can also be found in transversely oscillating cylinders. (Bao *et al.*, 2012; Peppa & Triantafyllou, 2016)

4.4.3 Persistence of the Boundary Layer in Transition

Figure 4.8 shows the vorticity contours and streamlines around the pitching NACA 0012 with 6 degrees pitching amplitude and motion reduced frequency of 0.1 ($A = 6^\circ$ and $k = 0.1$) at the highest geometric incident angle of the foil, $\alpha_u = 6$, and the maximum effective angle of

attack $\alpha_{eff} = \frac{\dot{\alpha} b}{U_\infty}$, which corresponds to the $\alpha_u = 3$. The LSB is initially formed close to the trailing-edge (Figure 4.8a) and is observed on the mid-upper surface at the highest geometric angle of attack (Figure 4.8b), which can be influenced by the leading edge separation and forms a significantly larger vortical region in cases that experience higher angles of attack (dynamic stall). In contrast to these cases of dynamic stall where a massive separation is observed on the airfoil (see figure 7 in Lee & Gerontakos (2004)), for the studied cases where transition occurs under pre-dynamic-stall conditions, the boundary layer behaves similar to that of attached flow in the sense that its edge is detectable all the way to the trailing-edge where the wake begins (Figure 4.8). This finding is in accordance with the pressure coefficient results (Figure 4.3); if significant separation had happened in the flow, the pressure distribution would have shown a flat trend in the separated region (similar to the pressure distributions at stall conditions) while figure 4.3 shows a monotonically decreasing pressure. Adding to the above discussion (for $A = 6°$), the results coming in the rest of this section will be at most for 3 degrees pitching amplitude, which helps even more to keep the flow attached. Consequently, using the vanishing vorticity criteria, the edge of the boundary layer can be determined at all the sections of the airfoil, specifically near the trailing-edge, which is of particular interest in this study to investigate the Kutta condition. Thus, by utilizing the CFD results, the edge of the boundary layer at the top and bottom of the airfoil have been found and the values of pressure and velocity at those locations have been extracted for further investigation provided in the coming sections.

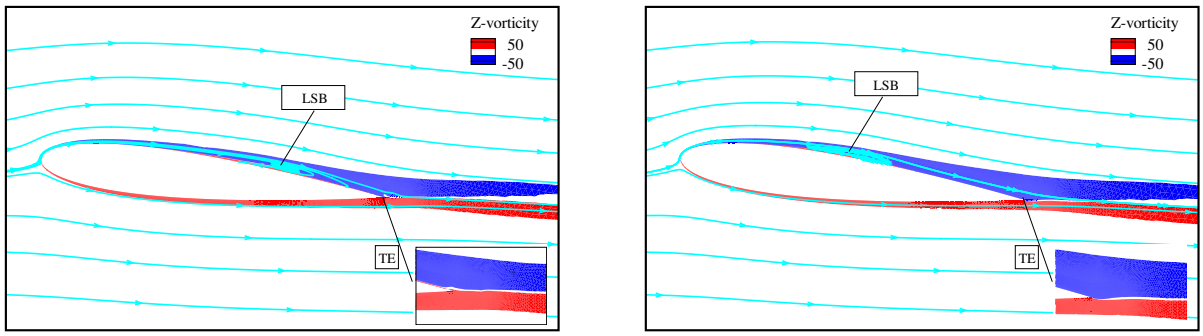

(a) (b)

Figure 4.8: Vorticity contours around a pitching NACA 0012 with $\alpha(t) = 6^\circ \sin(\omega t)$ and $k = 0.1$ and zoom-in near the trailing-edge at (a) $\alpha = \frac{A}{2}, \dot{\alpha}_{max} = Aw$ (maximum effective AOA) and (b) $\alpha_{max} = A, \dot{\alpha} = 0$ (maximum geometric AOA)

To better illustrate what is mentioned above, it is worth looking at a case where the airfoil experiences high angles of attack. Lee & Gerontakos (2004) experimentally studied the dynamic stall flow field around a pitching NACA 0012 prescribed to $\alpha(t) = 10^\circ + 15^\circ \sin(\omega t)$ at $Re = 135 \times 10^3$ and $k = 0.1$. As shown in figure 7 of their work, except for the cases that the airfoil is at relatively small angles of attack where the boundary layer persists, at higher angles, the vortical region on the airfoil grows and separation occurs at larger angles of attack quite far from the values considered in this study.

4.4.4 Effect of Transition on Circulation Dynamics

In the current study, the circulation dynamics is investigated at two different Reynolds numbers: $Re = 75 \times 10^3$ and $Re = 200 \times 10^3$; four different reduced frequencies: $k = 0.05, 0.1, 0.2, 0.3$; and three different pitching amplitudes: $A = 0.5, 1.5$ and 3 degrees. All the studied cases (9 in total) are shown in table 4.1.

Table 4.1: The pitching amplitudes, motion reduced frequencies and Reynolds numbers of all the studied cases.

	A \ k	0.05	0.1	0.2	0.3
$Re = 75 \times 10^3$	0.5°		*		
	1.5°		*		
	3°	*	*	*	*
$Re = 200 \times 10^3$	0.5°		*		
	3°	*	*		

Before discussing the effect of each parameter on the circulation dynamics, let us point out some noteworthy findings. For simplicity purposes, let, $\dot{\Gamma}_U = \frac{1}{2}(V_2^2 - V_1^2)$, $\dot{\Gamma}_P = (\Delta P_2 - \Delta P_1) / \rho$, $\dot{\Gamma}_{\text{total}} = \dot{\Gamma}_U + \dot{\Gamma}_P$ and $\dot{\Gamma}_{\text{Theodorsen}} \equiv \frac{\dot{L}_{Theodorsen}}{\rho U_\infty}$ (it is termed $\dot{\Gamma}_{\text{Theo}}$ in the coming figures). For a pitching airfoil hinged at the quarter-chord point, the total lift force reads $L_{Theodorsen} = \pi\rho b^2[U_\infty\dot{\alpha} + 0.5b\ddot{\alpha}] + 2\pi\rho U_\infty bC(k)[U_\infty\alpha + b\dot{\alpha}]$, where $C(k)$ is Theodorsen function (Theodorsen, 1935). As discussed above, in potential flow theory, $\dot{\Gamma}_P$ should be zero assuming zero pressure rise across the boundary layer at the trailing-edge station (zero loading). This assumption is accurate for high Reynolds number steady flows or unsteady flows at low reduced frequencies (quasi-steady conditions). Nevertheless, under unsteady conditions undergoing transition, this assumption might not be accurate and needs further investigation. Figures 4.9, 4.12 and 4.15 show the time-history of all the defined $\dot{\Gamma}$'s for all the studied cases. Note that all the results come from a pure sinusoidal pitching input, i.e. a simple harmonic motion, and have been normalized by the maximum value of the $\dot{\Gamma}_{\text{Kutta}}$. Interestingly, figures 4.9, 4.12 and 4.15 indicate that $\dot{\Gamma}_{\text{Kutta}}$ and $\dot{\Gamma}_U$ coincide in all the cases reflecting the fact that the linearization is fairly accurate, which is expected because of the considered small amplitudes. Therefore, any non-linearity in the flow dynamics should not be attributed to geometric non-linearities due to large angles. Moreover, since $\dot{\Gamma}_U \approx \dot{\Gamma}_{\text{Kutta}}$,

we have

$$\dot{\Gamma}_U = \dot{\Gamma}_{Kutta} \rightarrow \frac{1}{2}(V_2 + V_1)(V_2 - V_1) = U_\infty(V_2 - V_1) \tag{4.8}$$

resulting in $V_2 + V_1 = 2U_\infty$. So, the non-linear trend of the $\dot{\Gamma}_U$ must be attributed to the $V_2 - V_1$ term as $V_2 + V_1$ is shown to be equal to a constant (twice the free stream velocity).

In the upcoming sections, the results are provided in terms of rate of change of the circulation $\dot{\Gamma}$ coming from different sources and the Fast Fourier Transform (FFT) results of $\dot{\Gamma}_U$ and $\dot{\Gamma}_P$ to show both their linear-nonlinear behavior and their relative contribution to the total circulation. Moreover, in order to elaborate more on the flow events near the TE, the history of the boundary layer thickness on the top and bottom of the airfoil have been plotted. All the figures were normalized by the maximum thickness of the boundary layer.

Effect of pitching amplitude (A) on circulation dynamics

In this section, the effect of pitching amplitude (A) on the $\dot{\Gamma}$'s is investigated while the two other parameters are kept constant at $Re = 7.5 \times 10^4$ and $k = 0.1$. Since the objective of this article is to focus on transition-induced non-linearity on the lift dynamics in the pre-stall regime, the selected pitching amplitudes are fairly low. At lower amplitudes of pitching (Figure 4.9a), $\dot{\Gamma}_U$ behaves more linear compared to higher pitching amplitudes (Figures. 4.9b, 4.9c) where the non-linear trend is more apparent. This result can be confirmed by inspecting the FFT figures of $\dot{\Gamma}_U$ and $\dot{\Gamma}_P$ (Figure 4.10). Interestingly, both $\dot{\Gamma}_U$ and $\dot{\Gamma}_P$ possess cubic non-linearities in their response even at the considered small amplitudes and low frequency; the strength of this cubic non-linearity (i.e. third harmonic) relative to the linear response (first harmonic) increases as A increases. Of particular importance is the

remarkable contribution of the $\dot{\Gamma}_P$ to $\dot{\Gamma}_{\text{total}}$ in all the cases in this section (ranging between 15% to 35%).

Figure 4.9 shows that $\dot{\Gamma}_P$ is out of phase with respect to $\dot{\Gamma}_U$, which upon addition, would decrease the rate of circulation development (i.e. $\dot{\Gamma}_{\text{total}}$), causing a lag in circulation dynamics and consequently in lift dynamics too. The significant deviation of $\dot{\Gamma}_{\text{total}}$ from the classical linear theory of Theodorsen at a very small amplitude (0.5°) and low frequency ($k = 0.1$), shown in Figure 4.9a, is remarkable, and may be solely attributed to transition effects. However, increasing A, decreases the contribution of $\dot{\Gamma}_P$ and brings the $\dot{\Gamma}_{total}$ closer to $\dot{\Gamma}_U$ which is also reflected in the magnitude of the FFT results in figure 4.10 showing diminution of $|\dot{\Gamma}_P|$ when A increases. Nevertheless, we must point out that even in these cases of relatively larger amplitudes (Figure 4.9c), the effect of $\dot{\Gamma}_P$ is not negligible and the rate of circulation development is quite far from the linear theory of Theodorsen.

It must be noted that since the dynamics of $\dot{\Gamma}_P$ is non-linear, the superposition principle is not applicable and there must be coupling between the dynamics of the two-subsystems representing $\dot{\Gamma}_U$ and $\dot{\Gamma}_P$. For instance, assume the total circulation development is written as $\Gamma_{total} = a\,\Gamma + f(\gamma)$ where the first linear term represents the Kutta circulation ($\dot{\Gamma}_{\text{Kutta}} = \dot{\Gamma}_U$), and the second non-linear term represents the Γ_P. If this latter contribution is neglected, the circulation dynamics would be purely linear resulting in the classical theory of unsteady aerodynamics. However, when the second term does not vanish, the superposition principle cannot be applied; the total circulation cannot be decomposed into two contributions, one coming from each sub-system. Moreover, since $\dot{\Gamma}_P$ induces non-linearity in the total circulation, the non-linearity will also be inherited in the linear term ($a\,\Gamma$). That is, $\dot{\Gamma}_P$ is the main source of non-linearity in the response of $\dot{\Gamma}_U$ which explains why the CFD prediction of $\dot{\Gamma}_{\text{Kutta}}$ deviates from Theodorsen's.

In order to elaborate more on the flow events near the TE, the history of the boundary layer thickness on the top and bottom of the airfoil have been plotted in Figure 4.11. All the

figures were normalized by the maximum thickness of the boundary layer. Results reveal that the thickness of the boundary layer is not symmetric between the top and bottom surfaces of the airfoil otherwise, the Δy-plot would be flat zero. At lower A (Figure 4.11a), the y_{upper} and y_{lower} are more sinusoidal while increasing the pitching amplitude excites more non-linearity in the system. (Figure 4.11b,4.11c)

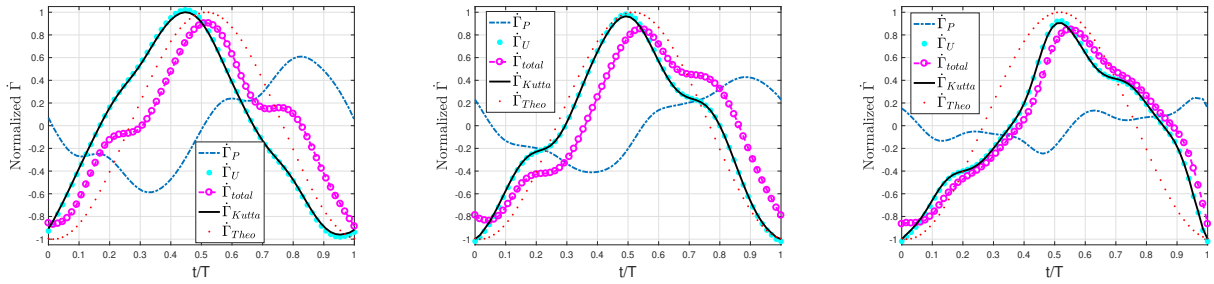

(a) (b) (c)

Figure 4.9: $\dot{\Gamma}$ history at $Re = 7.5 \times 10^4$, $k = 0.1$, and three different pitching amplitudes A: (a) $A = 0.5°$, (b) $A = 1.5°$, and (c) $A = 3°$

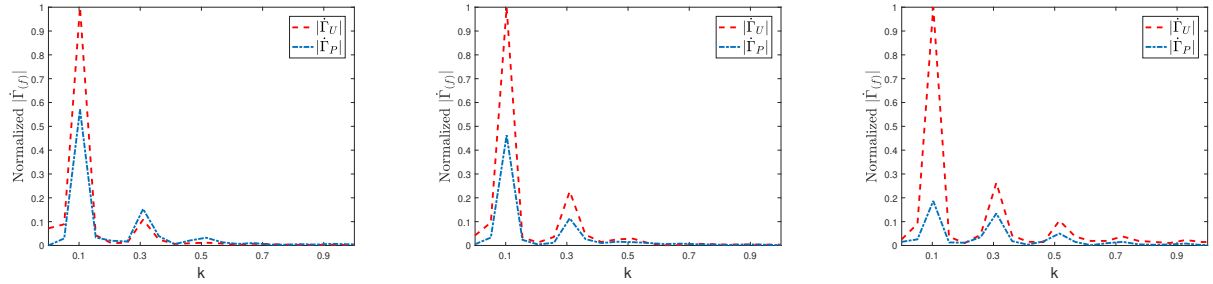

(a) (b) (c)

Figure 4.10: FFT of $\dot{\Gamma}_U$ and $\dot{\Gamma}_P$ at $Re = 7.5 \times 10^4$, $k = 0.1$, three different pitching amplitudes A: (a) $A = 0.5°$, (b) $A = 1.5°$, and (c) $A = 3°$

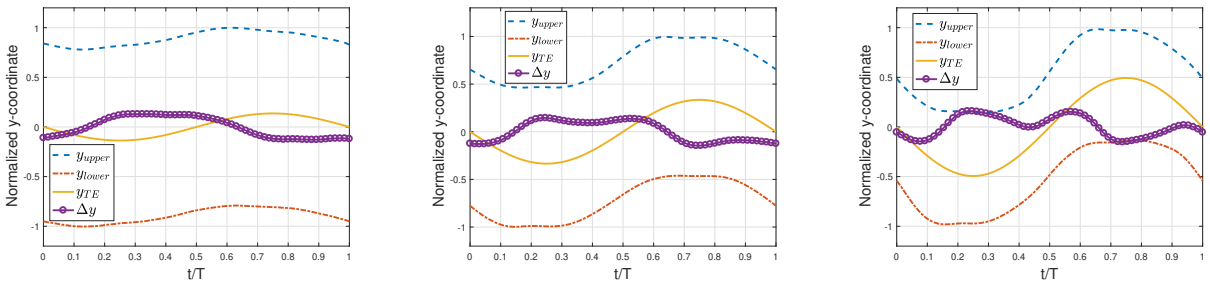

(a) (b) (c)

Figure 4.11: Variation of the y-coordinate of the boundary layer at the top and bottom of the trailing-edge and the difference between them (in purple) at $Re = 7.5 \times 10^4$, $k = 0.1$, and three different pitching amplitudes A: (a) $A = 0.5°$, (b) $A = 1.5°$, and (c) $A = 3°$

Effect of reduced frequency (k) on circulation dynamics

The reduced frequency effect is analyzed by varying the pitching frequency and retaining the pitching amplitude and Reynolds number fixed at $A = 3°$ and $Re = 7.5 \times 10^4$. Note that figures 4.9c, 4.10c, and 4.11c can also be considered in this section for comparison. Increasing k leads to an increase in the effective angle of attack causing the the adverse pressure gradient effects to dominate the transition effects. Hence, $\dot{\Gamma}_U$ becomes more linear (Figure 4.12), which can also be observed in the FFT results (Figure 4.13). Because of the relatively large A, the $\dot{\Gamma}_P$-contribution induces a small phase shift to $\dot{\Gamma}_{total}$ as discussed above. Even though there is a big difference between $\dot{\Gamma}_{\text{total}}$ coming from CFD and $\dot{\Gamma}_{\text{Theodorsen}}$; comparing the peaks imply that at low k values, Theodorsen phase matches with the numerical results, whereas at higher k values, a significant phase difference exists, which is similar to the viscous effects discussed in chapter 2. The boundary layer thickness (Figure 4.14) exhibits more sinusoidal trend as k increases which is in accordance with the circulation dynamics behavior.

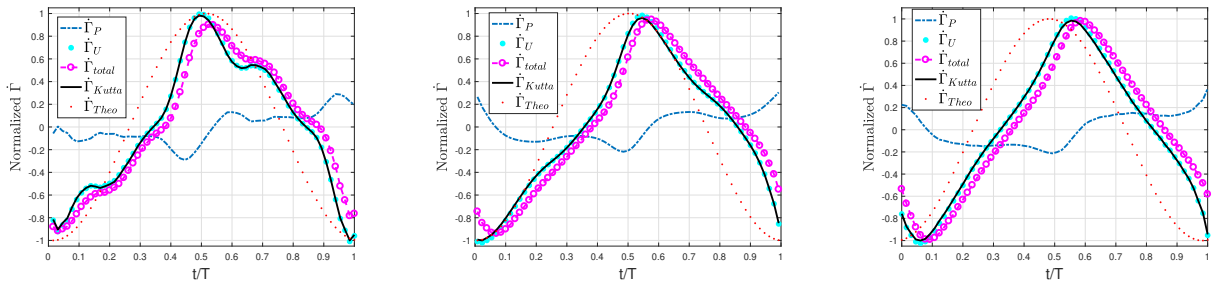

(a) (b) (c)

Figure 4.12: $\dot{\Gamma}$ history at $Re = 7.5 \times 10^4$, $A = 3°$ and three different motion reduced frequencies k: (a) $k = 0.05$, (b) $k = 0.2$, and (c) $k = 0.3$

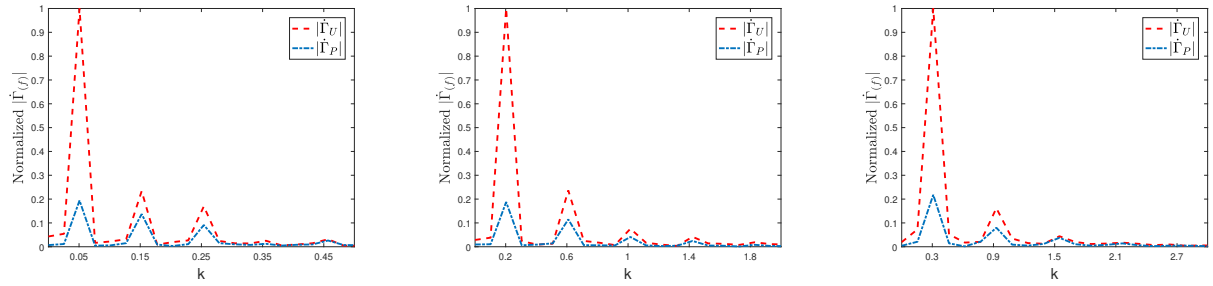

(a) (b) (c)

Figure 4.13: FFT of $\dot{\Gamma}_U$ and $\dot{\Gamma}_P$ at $Re = 7.5 \times 10^4$, $A = 3°$ and three different motion reduced frequencies k: (a) $k = 0.05$, (b) $k = 0.2$, and (c) $k = 0.3$

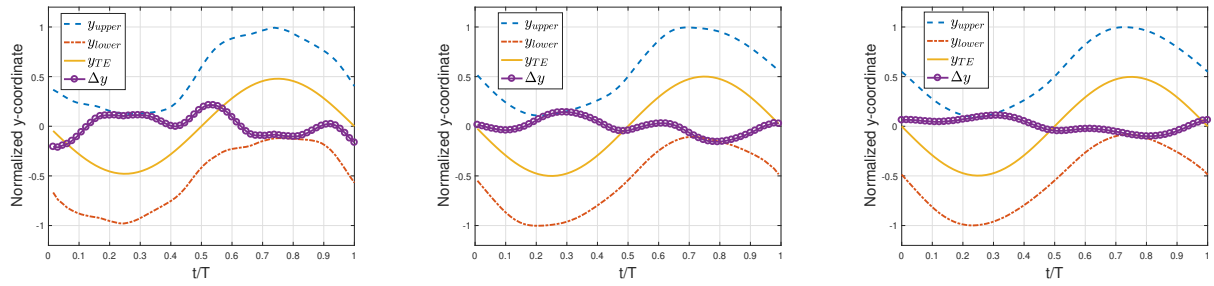

(a) (b) (c)

Figure 4.14: Variation of the y-coordinate of the boundary layer at the top and bottom of the trailing-edge and the difference between them (in purple) at $Re = 7.5 \times 10^4$, $A = 3°$ and three different motion reduced frequencies k: (a) $k = 0.05$, (b) $k = 0.2$, and (c) $k = 0.3$

Effect of Reynolds number (Re) on circulation dynamics

It is expected that increasing the Reynolds number will undermine the laminar-to-turbulent transition, therefore less non-linear behavior in the $\dot{\Gamma}$-response. For this part, the numerical simulations were carried out at two different reduced frequencies and pitching amplitudes (refer to table 4.1 for details). Considering figures 4.15a,4.15b for the $\dot{\Gamma}$-response when $A = 3°$ and comparing them with the ones for $Re = 7.5 \times 10^4$ (figures 4.9c, 4.12a), a more linear trend in $\dot{\Gamma}_U$ is observed (can also be confirmed with the FFT results). Unlike the lower Reynolds number case where $\dot{\Gamma}_P$ shifted the $\dot{\Gamma}_{\text{total}}$ to the right (i.e. induced a phase lag), at higher Reynolds number, this effect is not observed; $\dot{\Gamma}_{\text{total}}$ follows $\dot{\Gamma}_U$ in phase. However, at both Reynolds numbers, $\dot{\Gamma}_P$ leads to an attenuation of the amplitude of $\dot{\Gamma}_{\text{total}}$. The boundary layer thickness plots (figures 4.17a, 4.17b) also indicate smoother (akin to pure sinusoidal) trend of the flow.

Analogous to the influence of the pitching amplitude at the lower Reynolds number case (Figure 4.9), it can be seen that at lower pitching amplitudes (Figure 4.15c), $\dot{\Gamma}_P$ plays a considerable role in the dynamics of circulation. Nevertheless, it is interesting to point out that $\dot{\Gamma}_P$ possesses a linear behavior at small amplitude ($A = 0.5°$), low frequency ($k = 0.1$), and high Reynolds number ($Re = 20 \times 10^4$), as shown in Figure 4.15c which are the main assumptions underpinning the classical linear theory.

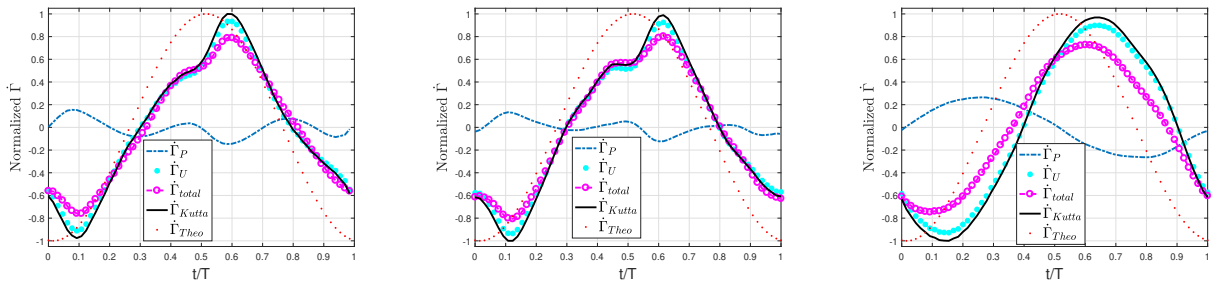

(a) (b) (c)

Figure 4.15: $\dot{\Gamma}$ history at $Re = 20 \times 10^4$ when (a) $k = 0.05$ and $A = 3°$, (b) $k = 0.1$ and $A = 3°$, and (c) $k = 0.1$ and $A = 0.5°$

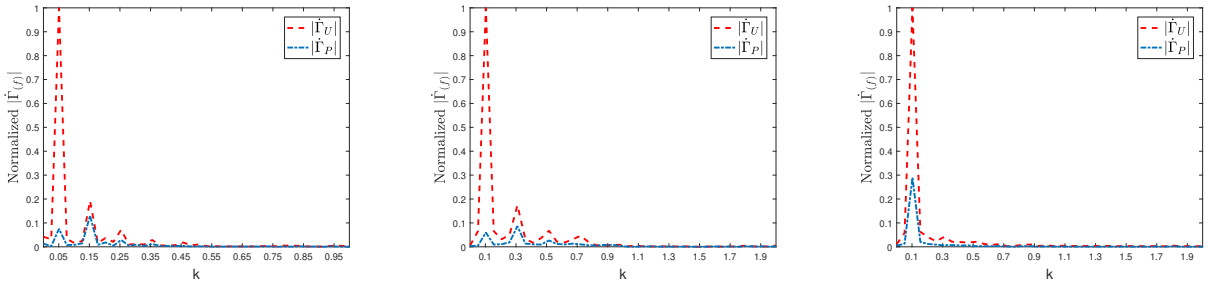

(a) (b) (c)

Figure 4.16: FFT of $\dot{\Gamma}_U$ and $\dot{\Gamma}_P$ at $Re = 20 \times 10^4$ when (a) $k = 0.05$ and $A = 3°$, (b) $k = 0.1$ and $A = 3°$, and (c) $k = 0.1$ and $A = 0.5°$

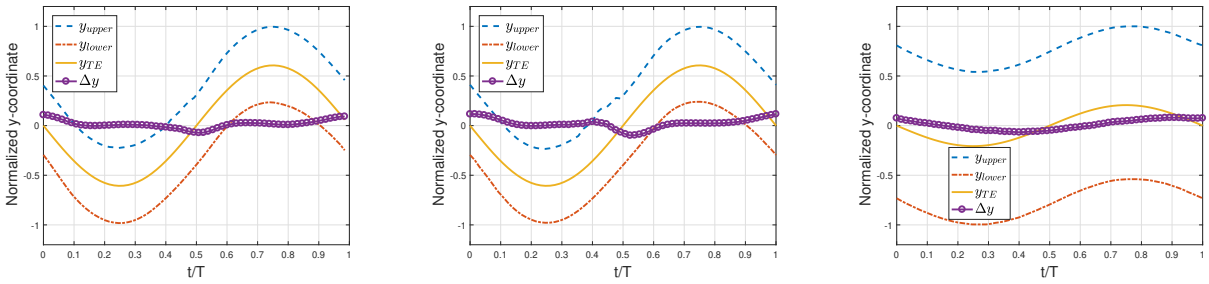

(a) (b) (c)

Figure 4.17: Variation of the y-coordinate of the boundary layer at the top and bottom of the trailing-edge and the difference between them (in purple) at $Re = 20 \times 10^4$ when (a) $k = 0.05$ and $A = 3°$, (b) $k = 0.1$ and $A = 3°$, and (c) $k = 0.1$ and $A = 0.5°$

4.5 Conclusion

CFD simulations (Reynolds-Averaged Navier-Stokes) are implemented to study the effects of the Laminar-to-Turbulent transition on the unsteady aerodynamic response of a pitching NACA 0012 airfoil. The $\gamma - Re_\theta$ transition model is coupled with $k - \omega$ SST turbulence model to account for transition effects. The numerical model (flow solver, closure model, dynamic mesh, etc) is validated against an experimental study at a moderate Reynolds number of $Re = 48 \times 10^3$, which shows the satisfactory accuracy of the numerical model. It

has been shown that under the studied conditions (the airfoil, free-stream turbulent intensity and reduced frequency), bellow $Re \approx 200 \times 10^3$, transition has a significant effect on the lift response. It induces non-linearities in the lift and circulation dynamics, which diminish as Reynolds number increases toward the fully turbulent flow.

Dissecting the flow field near the trailing-edge, we show that the Kutta condition is violated when transition occurs even at small pitching amplitudes ($A = 0.5°$) and low reduced frequencies ($k = 0.1$); the rate of vorticity pumped into the wake from the boundary layer is quite different from the linear potential flow theory (e.g., Theodorsen). Consequently, the development of the bound circulation over the airfoil is quite different from the linear theory, and in fact possesses a non-linear behavior even at very small angles of attack and oscillation frequencies. We show that this deviation is due to a pressure jump across the boundary layer, which is caused by transition effects. Such a pressure jump is typically ignored in potential flow analysis. It leads to an additional contribution to the rate of change of bound circulation, which is found to be out of phase with respect to the main linear component. Hence, upon addition, it decreases the rate of change of bound circulation, causing a lag in circulation development and consequently in lift dynamics.

The effect of three parameters (pitching amplitude, frequency and Reynolds number) on the circulation dynamics is investigated. As pitching amplitude or frequency increases, the effects due to adverse pressure gradient dominate over the transition effects, diminishing the contribution of the pressure jump, leading to a more linear response. Also, increasing the Reynolds number, the flow becomes closer to a fully turbulent one where the linear response is dominant.

Chapter 5

Conclusion and Future Considerations

5.1 Concluding remarks

Potential flow framework is the basis of almost all the analytical models in unsteady aerodynamics. This framework is not complete and requires an auxiliary condition. The most common condition that is employed is the Kutta condition. By removing the trailing-edge singularity, Kutta condition dictates the amount of circulation or lift on the airfoil. It was shown that the application of Kutta condition in unsteady flows, specially at high reduced frequencies and low Reynolds number flows, is controversial. In this work, the Kutta condition was relaxed, and unsteady triple deck theory; a boundary layer theory that accounts for the transition from a Blasius boundary layer to Goldstein wake layer at the trailing edge, was utilized to obtain the required condition in potential flow. As a result, a theoretical viscous unsteady aerodynamics model for an oscillating thin airfoil with arbitrary time-varying camber was developed. This model is essentially a viscous correction to Theodorsen's potential-flow frequency response function, which accounts for viscous actions near the trailing edge region. Using the developed model, it was shown that viscosity leads to a significant phase

lag at high frequencies and low Reynolds numbers, which is not predicted by Theodorsen's potential flow model. To validate our theoretical model, computational fluid dynamic (CFD) simulations were utilized to solve the fluid flow around a pitching NACA 0012. The incompressible unsteady Reynolds-averaged Navier-Stokes equations were solved for the cases of high Reynolds number and unsteady laminar ones for the cases of low Reynolds number. The total lift history was obtained from CFD at different motion frequencies and the frequency response was constructed, which showed very good agreement with the theoretical results. The differences between the classical model of Theodorsen and the developed viscous model were explained in terms of viscous induced lag and lag in circulation development. Moreover, the dissatisfaction with Kutta condition was discussed.

The natural extension of the theoretical model was to develop a numerical method that can handle any type of airfoil shape subjected to any arbitrary motion, which accounts for wake deformation. The best candidate was the efficient and sufficiently accurate unsteady vortex lattice model. It was shown through Hilbert matrices algebra how the Kutta condition was implicitly applied in UVLM by dictating the location of the collocation and control point (panel layout). Then, the Kutta condition was relaxed and the triple-deck theory was utilized to include the viscous effects in UVLM. Based on this approach, the location of the collocation and control points are no longer fixed and varies with time based on the strength of the singularity coming from the triple-deck theory, which is a function of angle of attack. Next, three different inputs, namely step, single-frequency and multi-frequency harmonic motions were prescribed to the airfoil and the results were compared against analytical and CFD results, which showed an excellent agreement.

Lastly, URANS simulations have been implemented to study the effects of the Laminar-to-Turbulent transition on the circulation dynamics of a pitching NACA 0012 airfoil laboring transition SST model. In the first step, the numerical method was validated against an experimental study and the flow field near the trailing edge was analyzed. It has been shown

that bellow $Re = 200 \times 10^3$ the transition effects are significant, and are not negligible from the lift force history point of view. By utilizing the exact derivation of the Kutta condition, it was shown that transition induces non-linearities in the circulation dynamics. Results showed the remarkable contribution of the pressure rise/fall across the boundary layer near the TE in the dynamics of the circulation, which is nonlinear in all the cases, and therefore, it is not expected to be captured by the linear potential flow theory. This work casts light on how the potential flow framework can be extended to account for the non-linear lift dynamics when transition occurs.

5.2 Recommendations for Future Research

One of the main contributions of this dissertation is providing a framework on how to replace the Kutta condition in the potential flow framework and, instead, utilizing the triple-deck boundary layer theory to obtain a viscous condition. As a result, all the classical theories that have used Kutta condition can be revisited to develop the viscous extension of them. Obviously, this process is involved and requires special techniques and tools. For example, Küssner (1929)'s model for sharp-edged gust problem (among many other examples in unsteady aerodynamics) can be a good candidate for this purpose.

In this work, we adopted UVLM to develop a numerical approach for the developed theoretical model. This work can be extended in two ways. First, another numerical model like discrete vortex method (DVM) can be utilized as the Kutta condition is explicitly satisfied in that framework, which facilitates replacing it with the viscous condition. Second, in the derivation of panel layout in UVLM based on Hilbert matrices algebra, it is assumed that the panel length is constant. This assumption can be relaxed, which may result in removing the dependence of the collocation and control point on the number of panel in the extended UVLM.

The main message of chapter 3 in this dissertation was to direct the attentions to a neglected term in classical theories, which plays a vital role in the non-linear circulation dynamics under transition conditions. The ultimate goal is to find the map between the neglected term, which comes from the pressure rise/fall across the boundary layer near the TE, and the effective parameters such as Reynolds number, motion frequency, type of maneuver, turbulent intensity, airfoil type etc. Therefore, a large numerical and/or experimental data set is needed to achieve this goal.

Bibliography

Abramson, H. N. & Chu, H.-H. 1959 A discussion of the flutter of submerged hydrofoils. *Journal of Ship Research* **3** (2).

Abramson, H. N., Chu, W.-H & Irick, J. T. 1967 Hydroelasticity with special reference to hydrofoil craft. *Tech. Rep.* 2557. NSRDC Hydromechanics Lab.

Abramson, H. N. & Ransleben, G. E. 1965 An experimental investigation of flutter of a fully submerged subcavitating hydrofoil. *Journal of Aircraft* **2** (5), 439–442.

Abu-Ghannam, BJ & Shaw, R 1980 Natural transition of boundary layersthe effects of turbulence, pressure gradient, and flow history. *Journal of Mechanical Engineering Science* **22** (5), 213–228.

Alben, S. 2008 The flapping-flag instability as a nonlinear eigenvalue problem. *Physics of Fluids* **20** (10), 104106.

Ansari, S. A., Żbikowski, R. & Knowles, K. 2006*a* Aerodynamic modelling of insect-like flapping flight for micro air vehicles. *Progress in Aerospace Sciences* **42** (2), 129–172.

Ansari, S. A., Żbikowski, R. & Knowles, K. 2006*b* Non-linear unsteady aerodynamic model for insect-like flapping wings in the hover. part 1: methodology and analysis. *Proceedings of the Institution of Mechanical Engineers, Part G: Journal of Aerospace Engineering* **220** (2), 61–83.

Ansari, S. A., Zbikowski, R. & Knowles, K. 2006*c* Non-linear unsteady aerodynamic model for insect-like flapping wings in the hover. part2: Implementation and validation. *Journal of Aerospace Engineering* **220**, 169–186.

Archibald, F. S. 1975 Unsteady kutta condition at high values of the reduced frequency parameter. *Journal of Aircraft* **12** (6), 545–550.

Arena, AV & Mueller, TJ 1980 Laminar separation, transition, and turbulent reattachment near the leading edge of airfoils. *AIAA Journal* **18** (7), 747–753.

Bao, Sheng, Chen, Sheng, Liu, Zhaohui, Li, Jing, Wang, Hanfeng & Zheng, Chuguang 2012 Simulation of the flow around an upstream transversely oscillating cylinder and a stationary cylinder in tandem. *Physics of Fluids* **24** (2), 023603.

Bass, R. L., Johnson, J. E. & Unruh, J. F. 1982 Correlation of lift and boundary-layer activity on an oscillating lifting surface. *AIAA Journal* **20** (8), 1051–1056.

Basu, B. C. & Hancock, G. J. 1978 The unsteady motion of a two-dimensional aerofoil in incompressible inviscid flow. *Journal of Fluid Mechanics* **87** (01), 159–178.

Batchelor, G. K. 2000 *An introduction to fluid dynamics*. Cambridge university press.

Belotserkovskii, S. M. 1977 Study of the unsteady aerodynamics of lifting surfaces using the computer. *Annual Review of Fluid Mechanics* **9** (1), 469–494.

Benton, SI & Visbal, MR 2019 The onset of dynamic stall at a high, transitional reynolds number. *Journal of Fluid Mechanics* **861**, 860–885.

Birkhoff, G. 1962 Helmholtz and taylor instability. *Proceedings of Symp. Applied Mathematics* **13**, 55–76.

Birnbaum, W. 1924 Der schlagflugelpropeller und die kleinen schwingungen elastisch befestigter tragfluegel. *Z Flugtech Motorluftschiffahrt* **15**, 128–134.

Birnbaum, W. & Ackermann, W. 1923 Die tragende wirbelfläche als hilfsmittel zur behandlung des ebenen problems der tragflügeltheorie. *ZAMM-Journal of Applied Mathematics and Mechanics/Zeitschrift für Angewandte Mathematik und Mechanik* **3** (4), 290–297.

Bisplinghoff, R. L., Ashley, H. & Halfman, R. L. 1996 *Aeroelasticity*. Dover Publications, New York.

Blasius, H. 1908 *Grenzschichten in Flüssigkeiten mit kleiner Reibung*. Druck von BG Teubner.

Boutilier, Michael SH & Yarusevych, Serhiy 2012 Separated shear layer transition over an airfoil at a low reynolds number. *Physics of Fluids* **24** (8), 084105.

Brown, S. N. & Cheng, H. K. 1981 Correlated unsteady and steady laminar trailing-edge flows. *Journal of Fluid Mechanics* **108**, 171–183.

Brown, S. N. & Daniels, P. G. 1975 On the viscous flow about the trailing edge of a rapidly oscillating plate. *Journal of Fluid Mechanics* **67** (04), 743–761.

Brown, S. N. & Stewartson, K. 1970 Trailing-edge stall. *Journal of Fluid Mechanics* **42** (03), 561–584.

Chow, R. & Melnik, R. E. 1976 Numerical solutions of the triple-deck equations for laminar trailing-edge stall. In *Proceedings of the Fifth International Conference on Numerical Methods in Fluid Dynamics June 28–July 2, 1976 Twente University, Enschede*, pp. 135–144. Springer.

Chu, W.-H. 1961 An aerodynamic analysis for flutter in Oseen-type viscous flow. *Journal of the Aerospace Sciences* **29**, 781–789.

Chu, W.-H. & Abramson, H. N. 1959 An alternative formulation of the problem of flutter in real fluids. *Journal of the Aerospace Sciences* **26** (10).

Collar, A. R. 1951 On the reciprocal of a segment of a generalized hilbert matrix. In *Mathematical Proceedings of the Cambridge Philosophical Society*, , vol. 47, pp. 11–17. Cambridge University Press.

Crighton, D. G. 1985 The Kutta condition in unsteady flow. *Annual Review of Fluid Mechanics* **17** (1), 411–445.

Daniels, P. G. 1978 On the unsteady Kutta condition. *The Quarterly Journal of Mechanics and Applied Mathematics* **31** (1), 49–75.

Darakananda, Darwin & Eldredge, Jeff D 2019 A versatile taxonomy of low-dimensional vortex models for unsteady aerodynamics. *Journal of Fluid Mechanics* **858**, 917–948.

Deparday, Julien & Mulleners, Karen 2019 Modeling the interplay between the shear layer and leading edge suction during dynamic stall. *Physics of Fluids* **31** (10), 107104.

Dickinson, M. H., Lehmann, F.-O. & Sane, S. P. 1999 Wing rotation and the aerodynamic basis of insect flight. *Science* **284** (5422), 1954–1960.

Ding, Q.n & Wang, D.-L. 2006 The flutter of an airfoil with cubic structural and aerodynamic non-linearities. *Aerospace science and technology* **10** (5), 427–434.

Dovgal, AV, Kozlov, VV & Michalke, A 1994 Laminar boundary layer separation: instability and associated phenomena. *Progress in Aerospace Sciences* **30** (1), 61–94.

Dowell, Earl H, Williams, MH & Bland, SR 1983 Linear/nonlinear behavior in unsteady transonic aerodynamics. *AIAA Journal* **21** (1), 38–46.

Dugas, René 2012 *A history of mechanics*. Courier Corporation.

Epps, Brenden P, Roesler, Bernard T, Medvitz, Richard B, Choo, Yeunun & McEntee, Jarlath 2019 A viscous vortex lattice method for analysis of cross-flow propellers and turbines. *Renewable Energy* **143**, 1035–1052.

Falkner, V. M. 1943 The calculation of aerodynamic loading on surfaces of any shape. *Tech. Rep.*. AERONAUTICAL RESEARCH COUNCIL LONDON (UNITED KINGDOM).

Fluent, Ansys 2009 12.0 users guide. *Ansys Inc* .

Ford, CW Pitt & Babinsky, Holger 2013 Lift and the leading-edge vortex. *Journal of Fluid Mechanics* **720**, 280–313.

Garmann, Daniel J & Visbal, Miguel R 2011 Numerical investigation of transitional flow over a rapidly pitching plate. *Physics of Fluids* **23** (9), 094106.

Garrick, I. E. 1937 Propulsion of a flapping and oscillating airfoil. *Tech. Rep.* NACA-TR-567.

Garrick, I. E. 1938 On some reciprocal relations in the theory of nonstationary flows. *Tech. Rep.* 629. NACA.

Gharali, Kobra & Johnson, David A 2013 Dynamic stall simulation of a pitching airfoil under unsteady freestream velocity. *Journal of Fluids and Structures* **42**, 228–244.

Glauert, H. 1926 *The elements of aerofoil and airscrew theory*. Cambridge University Press.

Goldstein, S. 1930 Concerning some solutions of the boundary layer equations in hydrodynamics. *Mathematical Proceedings of the Cambridge Philosophical Society* **26** (1), 1–30.

Goldstein, S. 1938 *Modern developments in fluid dynamics: an account of theory and experiment relating to boundary layers, turbulent motion and wakes*. Clarendon Press.

Graftieaux, L., Michard, M. & Grosjean, N. 2001 Combining piv, pod and vortex identification algorithms for the study of unsteady turbulent swirling flows. *Measurement Science and Technology* **12** (9), 1422.

Greer, Donald, Hamory, Phil, Edwards, Center, Krake, Keith & Drela, Mark 2000 Design and predictions for high-altitude (low reynolds number) aerodynamic flight experiment. *Journal of aircraft* **37** (4), 684–689.

Gupta, Rohit & Ansell, Phillip J 2018 Unsteady flow physics of airfoil dynamic stall. *AIAA Journal* **57** (1), 165–175.

Hedman, Sven G 1966 Vortex lattice method for calculation of quasi steady state loadings on thin elastic wings in subsonic flow. *Tech. Rep.*. AERONAUTICAL RESEARCH INST OF SWEDEN STOCKHOLM.

Helmholtz, Hermann 1858 About integrals of hydrodynamic equations related with vortical motions. *J. für die reine Angewandte Mathematik* **55**, 25.

Hemati, M. S., Eldredge, J. D. & Speyer, J. L. 2014 Improving vortex models via optimal control theory. *Journal of Fluids and Structures* **49**, 91–111.

Henry, C. J. 1961 Hydrofoil flutter phenomenon and airfoil flutter theory. *Tech. Rep.* 856. Davidson Laboratory.

Ho, C. & Chen, S. 1981 Unsteady kutta condition of a plunging airfoil. In *Unsteady turbulent shear flows*, pp. 197–206. Springer.

Hosseini, Seyed Mohammad, Vinuesa, Ricardo, Schlatter, Philipp, Hanifi, Ardeshir & Henningson, Dan S 2016 Direct numerical simulation of the flow around a wing section at moderate reynolds number. *International Journal of Heat and Fluid Flow* **61**, 117–128.

Howarth, L. 1935 The theoretical determination of the lift coefficient for a thin elliptic cylinder. *Proceedings of the Royal Society of London. Series A, Mathematical and Physical Sciences* **149** (868), 558–586.

Hussein, Ahmed A & Canfield, Robert A 2017 Unsteady aerodynamic stabilization of the dynamics of hingeless rotor blades in hover. *AIAA Journal* **56** (3), 1298–1303.

Hussein, A. A., Taha, H., Ragab, S. & Hajj, M. R. 2018 A variational approach for the dynamics of unsteady point vortices. *Aerospace Science and Technology* **78**, 559–568.

James, R. M. 1972 On the remarkable accuracy of the vortex lattice method. *Computer Methods in Applied Mechanics and Engineering* **1** (1), 59–79.

Jobe, C. E. & Burggraf, O. R. 1974 The numerical solution of the asymptotic equations of trailing edge flow. *Proceedings of the Royal Society of London A: Mathematical, Physical and Engineering Sciences* **340** (1620), 91–111.

Jones, M. A. 2003 The separated flow of an inviscid fluid around a moving flat plate. *Journal of Fluid Mechanics* **496**, 405–441.

Joukowsky, N. 1910 Über die konturen der tragflächen der drachenflieger. *Zeit. für Flugtechnik und Motorluftschiffahrt* **1**, 281–284.

Kadlec, R. A. & Davis, S. S. 1979 Visualization of quasiperiodic flows. *AIAA Journal* **17** (11), 1164–1169.

Katz, Joseph & Maskew, RIAN 1988 Unsteady low-speed aerodynamic model for complete aircraft configurations. *Journal of Aircraft* **25** (4), 302–310.

Katz, J. & Plotkin, A. 2001 *Low-speed aerodynamics*. Cambridge University Press.

Kim, Dong-Ha & Chang, Jo-Won 2010 Unsteady boundary layer for a pitching airfoil at low reynolds numbers. *Journal of mechanical science and technology* **24** (1), 429–440.

Kim, Dong-Ha & Chang, Jo-Won 2014 Low-reynolds-number effect on the aerodynamic characteristics of a pitching naca0012 airfoil. *Aerospace Science and Technology* **32** (1), 162–168.

Krylov, N. M. & Bogoliubov, N. N. 1943 *Introduction to Non-Linear Mechanics.(AM-11)*. Princeton University Press.

Kurtulus, D Funda 2018 Aerodynamic loads of small-amplitude pitching naca 0012 airfoil at reynolds number of 1000. *AIAA Journal* **56** (8), 3328–3331.

Küssner, H. G. 1929 Schwingungen von flugzeugflügeln. *Jahrbuch der deutscher Versuchsanstalt für Luftfahrt especially Section E3 Einfluss der Baustoff-Dämpfung* pp. 319–320.

Kutta, W. M. 1902 Auftriebskräfte in strömenden flüssigkeiten. *Illustrierte Aeronautische Mitteilungen* **6** (133), 133–135.

La Mantia, M. & Dabnichki, P. 2009 Unsteady panel method for flapping foil. *Engineering Analysis with Boundary Elements* **33** (4), 572–580.

Lamb, H. 1932 *Hydrodynamics*. Cambridge university press.

Langlois, W. E. & Deville, M. O. 2014 *Slow viscous flow*. Springer.

Langtry, Robin B & Menter, Florian R 2009 Correlation-based transition modeling for unstructured parallelized computational fluid dynamics codes. *AIAA Journal* **47** (12), 2894–2906.

Lee, T & Basu, S 1998 Measurement of unsteady boundary layer developed on an oscillating airfoil using multiple hot-film sensors. *Experiments in Fluids* **25** (2), 108–117.

Lee, T & Gerontakos, P 2004 Investigation of flow over an oscillating airfoil. *Journal of Fluid Mechanics* **512**, 313–341.

Li, J. & Wu, Z.-N. 2015 Unsteady lift for the wagner problem in the presence of additional leading/trailing edge vortices. *Journal of Fluid Mechanics* **769**, 182–217.

Lian, Yongsheng & Shyy, Wei 2007 Laminar-turbulent transition of a low reynolds number rigid or flexible airfoil. *AIAA Journal* **45** (7), 1501–1513.

Librescu, L., Chiocchia, G. & Marzocca, P. 2003 Implications of cubic physical/aerodynamic non-linearities on the character of the flutter instability boundary. *International Journal of Non-Linear Mechanics* **38** (2), 173–199.

Lighthill, M. J. 1953 On boundary layers and upstream influence. ii. supersonic flows without separation. *Proceedings of the Royal Society of London A: Mathematical, Physical and Engineering Sciences* **217** (1131), 478–507.

Liu, Jian, Xiao, Zhixiang & Fu, Song 2018 Unsteady transition studies over a pitching airfoil using ak-ω-γ transition model. *AIAA Journal* pp. 1–6.

Loewy, R. G. 1957 A two-dimensional approximation to unsteady aerodynamics in rotary wings. *Journal of Aeronautical Sciences* **24**, 81–92.

Lorber, Peter F & Carta, Franklin O 1994 Incipient torsional stall flutter aerodynamic experiments on three-dimensional wings. *Journal of Propulsion and Power* **10** (2), 217–224.

Mandre, S. & Mahadevan, L. 2010 A generalized theory of viscous and inviscid flutter. *Proceedings of the Royal Society of London A: Mathematical, Physical and Engineering Sciences* **466** (2113), 141–156.

McAuliffe, Brian R & Yaras, Metin I 2010 Transition mechanisms in separation bubbles under low-and elevated-freestream turbulence. *Journal of Turbomachinery* **132** (1), 011004.

McCroskey, WJ & Puccif, SL 1982 Viscous-inviscid interaction on oscillating airfoils in subsonic flow. *AIAA Journal* **20** (2), 167–174.

McMasters, John & Henderson, M 1980 Low-speed single-element airfoil synthesis. *Technical Soaring* **6** (2), 1–21.

Menter, F. R. 1994 Two-equation eddy-viscosity turbulence models for engineering applications. *AIAA Journal* **32** (8), 1598–1605.

Menter, Florian R, Langtry, Robin Blair, Likki, SR, Suzen, YB, Huang, PG & Völker, S 2006 A correlation-based transition model using local variablespart i: model formulation. *Journal of turbomachinery* **128** (3), 413–422.

Mesalles Ripoll, Pol, Rezaei, Amir S & Taha, Haitham E 2019 Extension of the unsteady vortex lattice method: viscous oseen vortices and thickness effects. In *AIAA Scitech 2019 Forum*, p. 1852.

Messiter, A. F. 1970 Boundary-layer flow near the trailing edge of a flat plate. *SIAM Journal on Applied Mathematics* **18** (1), 241–257.

Messiter, A. F. 1983 Boundary-layer interaction theory. *Journal of applied mechanics* **50** (4b), 1104–1113.

Michelin, S. & Smith, S. G. L. 2009 An unsteady point vortex method for coupled fluid–solid problems. *Theoretical and Computational Fluid Dynamics* **23** (2), 127–153.

Mueller, Thomas J & DeLaurier, James D 2003 Aerodynamics of small vehicles. *Annual review of fluid mechanics* **35** (1), 89–111.

Multhopp, H. 1950 *Methods for calculating the lift distribution of wings (subsonic lifting-surface theory)*. Aeronautical Research Council London.

Narasimha, R 1985 The laminar-turbulent transition zone in the boundary layer. *Progress in Aerospace Sciences* **22** (1), 29–80.

Negi, Prabal Singh, Vinuesa, Ricardo, Hanifi, Ardeshir, Schlatter, Philipp & Henningson, Dan S 2018 Unsteady aerodynamic effects in small-amplitude pitch oscillations of an airfoil. *International Journal of Heat and Fluid Flow* **71**, 378–391.

Nguyen, Anh Tuan, Kim, Joong-Kwan, Han, Jong-Seob & Han, Jae-Hung 2016 Extended unsteady vortex-lattice method for insect flapping wings. *Journal of Aircraft* **53** (6), 1709–1718.

Ogata, Katsuhiko & Yang, Yanjuan 1970 Modern control engineering .

Orszag, S. A. & Crow, S. C. 1970 Instability of a vortex sheet leaving a semi-infinite plate. *Studies in Applied Mathematics* **49** (2), 167–181.

Pelletier, Alain & Mueller, Thomas J 2000 Low reynolds number aerodynamics of low-aspect-ratio, thin/flat/cambered-plate wings. *Journal of Aircraft* **37** (5), 825–832.

Peppa, Sofia & Triantafyllou, George S 2016 Sensitivity of two-dimensional flow past transversely oscillating cylinder to streamwise cylinder oscillations. *Physics of Fluids* **28** (3), 037102.

Peters, D. A. 2008 Two-dimensional incompressible unsteady airfoil theoryan overview. *Journal of Fluids and Structures* **24**, 295312.

Poels, Allison, Rudmin, Daniel, Benaissa, Azemi & Poirel, Dominique 2015 Localization of flow separation and transition over a pitching naca0012 airfoil at transitional reynolds numbers using hot-films. *Journal of Fluids Engineering* **137** (12), 124501.

Poirel, D & Mendes, F 2014 Experimental small-amplitude self-sustained pitch–heave oscillations at transitional reynolds numbers. *AIAA Journal* **52** (8), 1581–1590.

Poling, D. R. & Telionis, D. P. 1986 The response of airfoils to periodic disturbances-the unsteady kutta condition. *AIAA Journal* **24** (2), 193–199.

Prandtl, Ludwig 1904 Über flussigkeitsbewegung bei sehr kleiner reibung. *Verhandl. III, Internat. Math.-Kong., Heidelberg, Teubner, Leipzig, 1904* pp. 484–491.

Prandtl, L. 1918 *Gesammelte Abhandlungen zur angewandten Mechanik, Hydro-und Aerodynamik*. Springer.

Prandtl, L. 1924 Über die entstehung von wirbeln in der idealen flüssigkeit, mit anwendung auf die tragflügeltheorie und andere aufgaben. In *Vorträge aus dem Gebiete der Hydro-und Aerodynamik (Innsbruck 1922)*, pp. 18–33. Springer.

Preston, J. H. 1943 *The Approximate Calculation of the Lift of Symmetrical Aerofoils taking Account of the Boundary Layer, with Application to Control Problems*. HM Stationery Office.

Pullin, D. I. & Wang, Z. 2004 Unsteady forces on an accelerating plate and application to hovering insect flight. *Journal of Fluid Mechanics* **509**, 1–21.

Raffel, Markus, Merz, Christoph B, Schwermer, Till & Richter, Kai 2015 Differential infrared thermography for boundary layer transition detection on pitching rotor blade models. *Experiments in Fluids* **56** (2), 30.

Ramamurti, R. & Sandberg, W. 2002 A three-dimensional computational study of the aerodynamic mechanisms of insect flight. *Journal of Experimental Biology* **205** (10), 15071518.

Ramesh, K., Gopalarathnam, A., Edwards, J. R., Ol, M. V. & Granlund, K. 2013 An unsteady airfoil theory applied to pitching motions validated against experiment and computation. *Theoretical and Computational Fluid Dynamics* pp. 1–22.

Ramesh, K., Gopalarathnam, A., Granlund, K., Ol, M. V. & Edwards, J. R. 2014 Discrete-vortex method with novel shedding criterion for unsteady aerofoil flows with intermittent leading-edge vortex shedding. *Journal of Fluid Mechanics* **751**, 500–538.

Rezaei, A. S. & Taha, H. 2017 Computational study of lift frequency responses of pitching airfoils at low reynolds numbers. AIAA-Paper 2017-0716.

Rezaei, Amir S & Taha, Haitham E 2019 Transition regime and its effects on the unsteady aerodynamic characteristics of a pitching airfoil. In *AIAA Scitech 2019 Forum*, p. 0302.

Richter, K, Koch, S, Gardner, AD, Mai, H, Klein, A & Rohardt, CH 2014 Experimental investigation of unsteady transition on a pitching rotor blade airfoil. *Journal of the American Helicopter Society* **59** (1), 1–12.

Robinson, A. & Laurmann, J. A. 1956 *Wing theory*. Cambridge University Press.

Rott, N. 1956 Diffraction of a weak shock with vortex generation. *Journal of Fluid Mechanics* **1** (01), 111–128.

Rott, N. & George, M. B. T. 1955 An approach to the flutter problem in real fluids. *Tech. Rep.* 509.

Saffman, Philip G 1992 *Vortex dynamics*. Cambridge university press.

Santos, Carlos R & Marques, Flavio D 2018 Energy harvesting from stall-induced oscillations of pitching airfoils at high-subsonic regime. In *2018 AIAA/ASCE/AHS/ASC Structures, Structural Dynamics, and Materials Conference*, p. 0463.

Satyanarayana, B. & Davis, S. 1978 Experimental studies of unsteady trailing-edge conditions. *AIAA Journal* **16** (2), 125–129.

Savage, S. B., Newman, B. G. & Wong, D. T.-M. 1979 The role of vortices and unsteady effects during the hovering flight of dragonflies. *The Journal of Experimental Biology* **83** (1), 59–77.

Schlichting, H. & Truckenbrodt, E. 1979 *Aerodynamics of the Airplane*. McGraw-Hill.

Sears, WR 1976*a* Unsteady motion of airfoils with boundary-layer separation. *AIAA Journal* **14** (2), 216–220.

Sears, WR & Telionis, DP 1975 Boundary-layer separation in unsteady flow. *SIAM Journal on Applied Mathematics* **28** (1), 215–235.

Sears, W. R. 1956 Some recent developments in airfoil theory. *Journal of the Aeronautical Sciences* .

Sears, W. R. 1976*b* Unsteady motion of airfoils with boundary-layer separation. *AIAA Journal* **14** (2), 216–220.

Shen, S. F. & Crimi, P. 1965 The theory for an oscillating thin airfoil as derived from the Oseen equations. *Journal of Fluid Mechanics* **23** (03), 585–609.

Slotine, Jean-Jacques E, Li, Weiping & others 1991 *Applied nonlinear control*, , vol. 199. Prentice hall Englewood Cliffs, NJ.

Smith, FT 1986 Steady and unsteady boundary-layer separation. *Annual review of fluid mechanics* **18** (1), 197–220.

Smith, F. T. 1983 Interacting flow theory and trailing edge separation–no stall. *Journal of fluid Mechanics* **131**, 219–249.

Smith, Michael JC 1996 Simulating moth wing aerodynamics-towards the development of flapping-wing technology. *AIAA Journal* **34** (7), 1348–1355.

Spence, D. A. 1954 Prediction of the characteristics of two-dimensional airfoils. *Journal of the Aeronautical Sciences* .

Stanford, Bret K & Beran, Philip S 2010 Analytical sensitivity analysis of an unsteady vortex-lattice method for flapping-wing optimization. *Journal of Aircraft* **47** (2), 647–662.

Stewartson, K. 1968 On the flow near the trailing edge of a flat plate. *Proceedings of the Royal Society of London A: Mathematical, Physical and Engineering Sciences* **306** (1486), 275–290.

Stewartson, K. 1974 Multistructured boundary layers on flat plates and related bodies. *Adv. Appl. Mech* **14** (145-239), 136.

Stewartson, K. 1981 D' alembert's paradox. *SIAM review* **23** (3), 308–343.

SureshBabu, ArunVishnu, Ramesh, Kiran & Gopalarathnam, Ashok 2019 Model reduction in discrete-vortex methods for unsteady airfoil flows. *AIAA Journal* pp. 1–14.

Taha, H., Hajj, M. R. & Beran, P. S. 2014 State space representation of the unsteady aerodynamics of flapping flight. *Aerospace Science and Technology* **34**, 1–11.

Taha, Haithem & Rezaei, Amir S 2019*a* Viscous extension of potential-flow unsteady aerodynamics: the lift frequency response problem. *Journal of Fluid Mechanics* **868**, 141–175.

Taha, Haithem E, Hajj, Muhammad R & Nayfeh, Ali H 2012 Flight dynamics and control of flapping-wing mavs: a review. *Nonlinear Dynamics* **70** (2), 907–939.

Taha, Haitham E & Rezaei, Amir S 2018 Unsteady viscous lift frequency response using the triple deck theory. In *2018 AIAA Aerospace Sciences Meeting*, p. 0038.

Taha, Haitham E & Rezaei, Amir S 2019*b* On the dynamics of unsteady lift and circulation and the circulatory-non-circulatory classification. In *AIAA Scitech 2019 Forum*, p. 1853.

Tchieu, A. A. & Leonard, A. 2011 A discrete-vortex model for the arbitrary motion of a thin airfoil with fluidic control. *Journal of Fluids and Structures* **27** (5), 680–693.

Theodorsen, T. 1935 General theory of aerodynamic instability and the mechanism of flutter. *Tech. Rep.* 496. NACA.

Tietjens, O. K. G. & Prandtl, L. 1934 *Applied hydro-and aeromechanics: based on lectures of L. Prandtl*. Courier Corporation.

Truckenbrodt, E. 1953 Tragflächentheorie bei inkompressibler strömung. *Jahrbuch* pp. 40–65.

Veldmann, A. E. P. & Van de Vooren, A. I. 1975 Drag of a finite plate. In *Proceedings of the Fourth International Conference on Numerical Methods in Fluid Dynamics*, pp. 423–430. Springer.

Von Baumhauer, AG & Koning, C 1923 On the stability of oscillations of an airplane wing .

Von Karman, T. & Sears, W. R. 1938 Airfoil theory for non-uniform motion. *J. Aeronautical Sciences* **5** (10), 379–390.

Wagner, H. 1925 Uber die entstehung des dynamischen auftriebs von tragflugeln. *ZAMM* **5**.

Wang, C. & Eldredge, J. D. 2013 Low-order phenomenological modeling of leading-edge vortex formation. *Theoretical and Computational Fluid Dynamics* **27** (5), 577–598.

Wang, Shengyi, Ingham, Derek B, Ma, Lin, Pourkashanian, Mohamed & Tao, Zhi 2010 Numerical investigations on dynamic stall of low reynolds number flow around oscillating airfoils. *Computers & Fluids* **39** (9), 1529–1541.

Wang, Z. 2000 Vortex shedding and frequency selection in flapping flight. *Journal of Fluid Mechanics* **410**, 323–341.

Weissinger, J. 1949 Über eine erweiterung der prandtlschen theorie der tragenden linie. *Mathematische Nachrichten* **2** (1-2), 45–106.

Wilcox, D. C. 1998 *Turbulence modeling for CFD*. DCW industries La Canada, CA.

Woolston, D. S. & Castile, G. E. 1951 Some effects of variations in several parameters including fluid density on tbe flutter speed of light uniform cantilever wings .

Xia, X. & Mohseni, K. 2013 Lift evaluation of a two-dimensional pitching flat plate. *Physics of Fluids* **25** (9), 091901.

Xia, X. & Mohseni, K. 2017 Unsteady aerodynamics and vortex-sheet formation of a two-dimensional airfoil. *Journal of Fluid Mechanics* **830**, 439–478.

Yan, Z., Taha, H. & Hajj, M. R. 2014 Geometrically-exact unsteady model for airfoils undergoing large amplitude maneuvers. *Aerospace Science and Technology* **39**, 293–306.

Yarusevych, Serhiy, Sullivan, Pierre E & Kawall, John G 2009 On vortex shedding from an airfoil in low-reynolds-number flows. *Journal of Fluid Mechanics* **632**, 245–271.

Yongliang, Y., Binggang, T. & Huiyang, M. 2003 An analytic approach to theoretical modeling of highly unsteady viscous flow excited by wing flapping in small insects. *Acta Mechanica Sinica* **19** (6), 508–516.

Zakaria, Mohamed Y, Al-Haik, Mohammad Y & Hajj, Muhammad R 2015 Experimental analysis of energy harvesting from self-induced flutter of a composite beam. *Applied Physics Letters* **107** (2), 023901.

Zakaria, M. Y., Taha, H. & Hajj, M. R. 2017 Measurement and modeling of lift enhancement on plunging airfoils: A frequency response approach. *Journal of Fluids and Structures* **69**, 187–208.